Title
Probing the heme structure and environment of bacterial Heme-Nitric oxide/OXygen binding domains with resonance Raman spectroscopy

Author
Tran, Rosalie

Publication Date
2010

Peer reviewed|Thesis/dissertation

Probing the heme structure and environment of bacterial *H*eme-*N*itric oxide/*OX*ygen binding domains with resonance Raman spectroscopy

by

Rosalie Tran

A dissertation submitted in partial satisfaction of the

requirements for the degree of

Doctor of Philosophy

in

Chemistry

in the

Graduate Division

of the

University of California, Berkeley

Committee in charge:

Professor Richard A. Mathies, Co-chair
Professor Michael A. Marletta, Co-chair
Professor Judith P. Klinman
Professor James M. Berger

Spring 2010

Probing the heme structure and environment of bacterial *H*eme-*N*itric oxide/*OX*ygen binding domains with resonance Raman spectroscopy

by Rosalie Tran

Abstract

Probing the heme structure and environment of bacterial *H*eme-*N*itric oxide/*OX*ygen binding domains with resonance Raman spectroscopy

by

Rosalie Tran

Doctor of Philosophy in Chemistry

University of California, Berkeley

Professor Richard A. Mathies, Co-chair

Professor Michael A. Marletta, Co-chair

The *H*eme-*N*itric oxide/*OX*ygen binding (H-NOX) domain encompasses a family of proteins closely related (≤ 40% sequence identity) to the heme domain of soluble guanylate cyclase (sGC), the eukaryotic enzyme receptor for NO [1, 2]. sGC discriminates between NO and O_2, and exclusively binds NO even in the presence of excess O_2. Although some H-NOX domains have ligand binding properties that are identical to sGC, others additionally bind O_2, including the atypical sGCs from *Drosophila melanogaster* and *Caenorhabditis elegans* [1, 3, 4]. The molecular basis of this ligand selectivity is not fully understood. In order to better understand the H-NOX domain, resonance Raman (RR) spectroscopy was employed in combination with isotopic substitution and site-directed mutagenesis to probe the heme pocket in *Thermoanaerobacter tengcongensis* (*Tt* H-NOX) as a model system for this family of heme proteins. Thus, the expression, purification, and RR characterization of *Tt* H-NOX and selected mutants were performed to elucidate the heme environmental properties that influence ligand binding.

A striking feature of the O_2-bound WT *Tt* H-NOX crystal structure is the presence of a distorted heme molecule [5]. RR investigation of *Tt* H-NOX proteins containing mutations at key conserved residues, Ile-5 and Pro-115, determined that the most dramatic heme conformational changes occurred in the O_2-bound forms, and that the single P115A mutation generated a significantly relaxed chromophore. Decreased RR intensities were observed for several out-of-plane modes in the 400-750 cm^{-1} region known to be sensitive to ruffling and saddling deformations, as well as increased vibrational frequencies for the core heme skeletal modes. These changes demonstrated that the P115A heme conformation was considerably more relaxed than WT, with increased flexibility within the protein pocket that allowed for rapid sampling of alternate conformations.

Another remarkable feature of this family is the spectroscopic observation of an unusually high ν(C-O) frequency. To elucidate the interactions responsible for this property, mutations were made in *Tt* H-NOX to probe the distal pocket, the conserved Tyr-Ser-Arg (YxSxR) motif, and the heme-linkage site (His-102). RR spectra of these mutants indicated that H-bonding interactions between these residues and the heme significantly affected the CO bond by increasing the back-donation of the Fe^{II} d_π electrons into the CO π^* orbitals. The most significant change occurred upon disruption of the H-bonds between the YxSxR motif and the heme propionate groups, producing two dominant CO-bound heme conformations; one was structurally similar to WT, and the other conformer displayed ν(C-O) downshifts of up to ~70 cm^{-1}. Based on these shifts, the most important factor contributing to the C-O stretching mode may be the neutralization of the negative charges on the propionate groups via the strictly conserved YxSxR motif.

Finally, the role of the *Tt* H-NOX binding pocket in stabilizing the O_2 complex was investigated. Evidence of H-bonds to the bound O_2 was demonstrated in the RR spectra of Trp-9 and Tyr-140 mutants; the disruption of the H-bond network in these mutations increased ν(Fe-O_2) upon returning electron density to the Fe-O_2 bond. In contrast, the addition of steric bulk to the H-NOX pocket decreased the ν(Fe-O_2) frequency relative to the WT protein. These shifts suggested that the bulky distal residues forced the H-NOX binding pocket into a more open position that increased the distance between Tyr-140 and the O_2, thereby weakening this crucial H-bond. Thus, two distinct factors influence the ν(Fe-O_2) in *Tt* H-NOX: (i) electrostatic effects from H-bonding with Tyr-140, which *increased* the ν(Fe-O_2) frequency upon its removal; and (ii) steric effects which *decreased* ν(Fe-O_2) due to bond lengthening from a more loosely held O_2 ligand.

In summary, this work presents a comparative analysis of the heme environmental effects in *Tt* H-NOX. By directly probing the interactions between the heme chromophore and the protein pocket through a combination of RR spectroscopy and site-directed mutagenesis, this study may elucidate the biochemical properties of these H-NOX domains, and bring insight into the relationship between heme structure and protein function in this family.

Dedication

In loving memory of my grandmother, Muoi Thi Ho,

and

To my wonderfully supportive family and friends, for their love and encouragement.

Table of Contents

List of Figures

List of Tables

Acknowledgement

This dissertation represents the culmination of my journey through graduate school, which has been both exciting and difficult at times. I am quite certain that I would not have survived it as well without the generous support, guidance, and encouragement from my mentors, labmates, friends, and family.

First and foremost, I am grateful to my advisors, Prof. Richard A. Mathies and Prof. Michael A. Marletta, for giving me the freedom to pursue this project. To Rich, I am indebted for his steadfast support and guidance throughout the years in my research endeavors. His ceaseless enthusiasm for science and learning has been inspirational, in addition to his high standard for thoroughness and quality in research. To Michael, I am appreciative for always reminding me to step back and look at the big picture when I got too caught up or stuck on the details. Their complementary advising styles have greatly enriched my graduate experiences. I would also like to thank my undergraduate advisors at Occidental College, Prof. Phoebe K. Dea and Prof. Tetsuo Otsuki, who were influential in encouraging me to pursue a Ph.D. in Chemistry.

I would also like to thank the members of my qualifying exam committee: Professors Judith P. Klinman, Graham R. Fleming, Haw Yang, and James M. Berger. I could not have asked for a friendlier committee to ease my nervousness and anxiety during the exam. Special thanks also go to Prof. Klinman and Prof. Berger for their acceptance to be on my dissertation committee and read about my resonance Raman studies on the H-NOX domains.

Of course, much of my research endeavors would not have been possible without the amazing efforts of Mary R. Hammond and F. Jeffrey Sturm, the administrative assistants to the Mathies and Marletta laboratories, respectively. Both always managed to find time in their hectic days to help me out or provide support, reminding me to keep perspective on the important things in life. Words cannot fully express my gratitude to them for their incredible ability to keep the labs running so smoothly for everyone.

My fellow colleagues over the years in both the Mathies and Marletta groups also deserve heartfelt thanks. I am delighted to have been a part of these two groups, with their evolving mix of cultures, personalities, and opinions. I am indebted to many of them for their help with technical difficulties, ranging from electronic problems with the Kr^+ laser to molecular biology problems with cloning or purification. As a biophysical chemist in these two groups, I have often felt like a "jack of all trades, [but] master of none." Thus, I would like to thank the Mathies lab for teaching this "biologist" some physical chemistry, and the Marletta lab for teaching this "p-chemist" some molecular biology and protein biochemistry.

Although I decided not to specifically name people in the two groups for fear of accidentally forgetting someone (as is apparent by the paragraph above), there are two individuals who stand out for their constant encouragement throughout the years and greatly contributed to my well being during the difficult times in graduate school: Lily Y. Chao and Hans K. Carlson. They were my constant reminders to keep a positive outlook even when prospects appeared bleak. Thank you so much for keeping my life balanced both in and out of the lab.

In closing, I would like to thank my wonderful (and ridiculously huge) family for helping me maintain my perspective and sanity throughout the years. I am very lucky to have such a supportive, loving, and close network to cheer me on in all of my endeavors. My eight nieces and nephews provided me with a constant source of fun distractions, while my five older siblings and their spouses always assured me that they would be proud of me regardless of my accomplishments. Finally, I thank my parents for their love, unwavering support, and faith in me. Although they won't be able to read a word of this dissertation due to language barriers, I can at least attempt to translate my gratitude to them into Vietnamese (with the help of the internet):

Cảm ơn, Mẹ và Cha.

I hope that I got that right.

Chapter 1

Introduction

This thesis investigates, via resonance Raman (RR) spectroscopy and site-directed mutagenesis, how the protein environment of the *H*eme-*N*itric oxide/*OX*ygen binding (H-NOX) domain plays a role in regulating ligand binding and heme conformation. Using the H-NOX domain from *Thermoanaerobacter tengcongensis* (*Tt* H-NOX) as a model system, the aim of this work is to elucidate the interactions occurring between the binding pocket and the heme prosthetic group, and to understand the divergent ligand binding properties within this family of heme proteins. RR analyses of the *Tt* H-NOX domain are presented and discussed in Chapters 2-4. In addition, Chapter 5 summarizes the conclusions of the work presented in this dissertation, and outlines some prospective future studies for the H-NOX family. Chapter 1, is divided into three subcategories: the first section discusses the role and importance of soluble guanylate cyclase (sGC) in the nitric oxide (NO) signaling pathway; the second section highlights the sGC studies that led to the identification of the H-NOX domain, and outlines our current understanding of this family; and the third section provides an overview of RR spectroscopy in application to heme proteins. Finally, the main focus and structural organization of this thesis will be presented at the end of Chapter 1.

1.1 Nitric oxide in biology

It is well established that the diatomic radical, NO, functions as a cytotoxin and environmental pollutant; however, NO is also an important signaling molecule in eukaryotic organisms with an array of widely studied pharmacological and physiological effects [6-14]. At high concentrations, NO is utilized by the immune system as a potent antimicrobial toxin that is generated by immunostimulated-activated macrophages to kill infectious organisms and tumor cells upon the triggering of an anti-pathogen and anti-tumor response [15-19]. In addition, NO may also contribute to tissue damage during infection and inflammation since the long-term production of NO can lead to the development of cancer due to its ability to damage DNA and cause cellular injury [20, 21].

In contrast to its cytotoxic properties, NO is also responsible for regulating many downstream physiological processes at low nanomolar concentrations in eukaryotes, most notably in the cardiovascular and nervous systems. In the cardiovascular system, these processes include vascular tone, in addition to platelet function and aggregation; whereas neurotransmission is controlled in the nervous system [22, 23]. Together, these cellular responses are mediated via the well-known heme-based enzyme receptor for NO, soluble guanylate cyclase (sGC) [24-27].

1.1.1 sGC and the NO/cGMP signaling pathway

In addition to denitrification pathways, nitric oxide is produced in biology by the enzyme, nitric oxide synthase (NOS), from the oxidation of L-arginine into L-citrulline and NO. This process is regulated *in vivo* by the binding of Ca^{2+} ions to calmodulin (Cam), which then binds to and activates NOS to produce NO [28]. Three known isoforms of NOS exist and display high sequence identity (~50%): inducible NOS (iNOS), endothelial NOS (eNOS), and neuronal NOS (nNOS) [28, 29]. Since eNOS and nNOS are both constitutive enzymes that transiently produce low levels of NO, they are mainly involved in homeostatic processes such as neurotransmission, peristalsis, and vasodilation [6, 24, 25, 28]. In contrast, the inducible enzyme iNOS is the main source of NO during antimicrobial, anti-tumor, and inflammation responses, producing large quantities of NO on the order of 10^6 molecules per cell for extended periods of time [15, 16, 18, 19, 28, 30, 31].

It is well known that NO can be a potent toxin and highly reactive with different cellular components, including O_2, thiols, and metal ions; thus, the use of NO as a signaling molecule requires a highly selective receptor. This specificity is satisfied via sGC, which selectively binds NO even in the presence of excess O_2, despite having the same heme prosthetic group as the globins. The uncharged NO radical generated by NOS is able to rapidly diffuse across cell membrane walls and bind to sGC at a diffusion-limited rate, activating the enzyme by several hundred-fold [26, 27]. This

activation initiates the rapid conversion of guanosine triphosphate (GTP) to cyclic guanosine monophosphate (cGMP), which then binds to phosphodiesterases, cGMP-dependent protein kinases, and cGMP-gated ion channels, leading to the downstream regulation of several physiological functions (Figure 1.1).

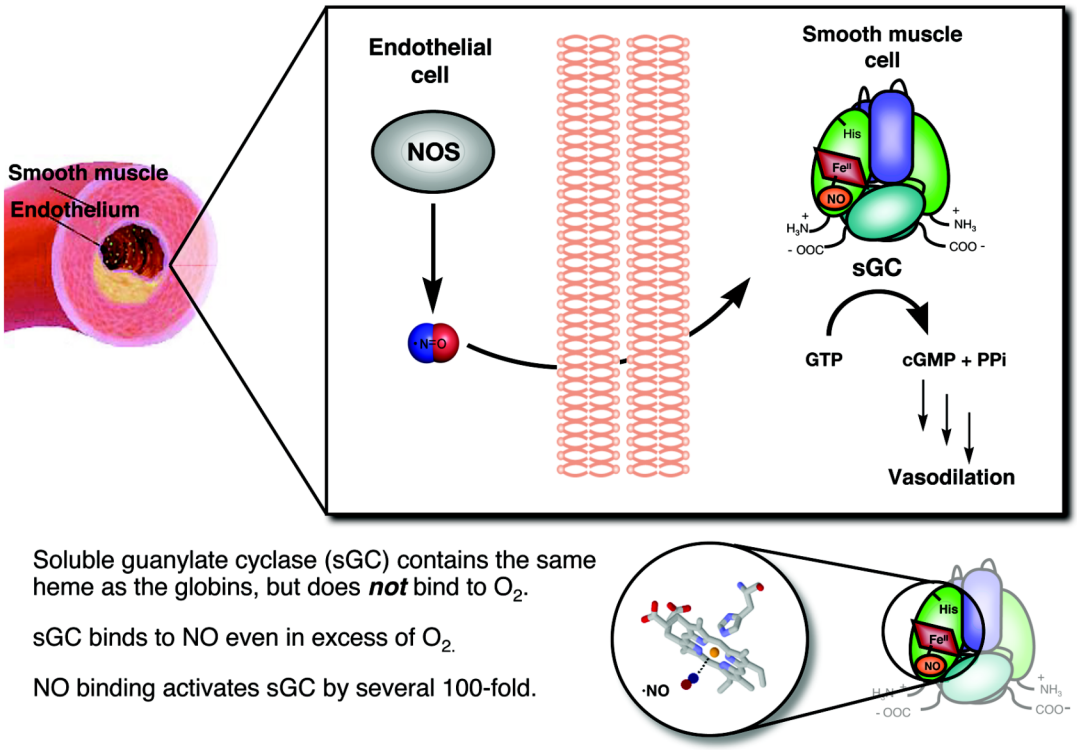

Figure 1.1 Nitric oxide (NO) signaling pathway in eukaryotic organisms. NO is produced by nitric oxide synthase (NOS) and diffuses across cell membrane layers to a target cell. Although the NO receptor sGC contains the same histidyl-ligated heme chromophore as the globins, it does not bind O_2, exclusively binding NO even in excess concentrations of O_2. Upon binding to soluble guanylate cyclase (sGC), NO activates the enzyme by several hundred-fold and catalyzes the synthesis of cGMP from GTP. The signaling pathway scheme is adapted from Denninger *et al*. [26].

1.1.2 Structural components of sGC

sGC is a 72 kDa heterodimeric enzyme composed of α and β subunits, and binds one heme molecule at the N-terminal β-chain region per heterodimer [26, 27, 32]. Although four sGC polypeptides are known to exist, the most well studied sGC isoform to date is the α1β1 heterodimer. Each subunit of sGC is divided into four distinct domains. The β subunit binds heme and consists of the following domains: an N-terminal heme-binding domain, a Per/Arnt/Sim (PAS) domain, a coiled-coil region, and a C-terminal

catalytic domain (Figure 1.2) [27]. Despite being composed of similar domains, the α subunit does not bind heme. The central regions of the sGC subunits are thought to assist in the formation of a functionally active heterodimer. Whereas the heme-binding domain is located in the N-terminal region of the β subunit, the catalytic domain encompasses C-terminal portions of both α1 and β1 subunits. Winger *et al*. localized the catalytic domains of sGC to residues 467-690 and 414-619 of the α1 and β1 subunits, respectively [33]. Efficient catalysis of cGMP synthesis requires both catalytic domains from the α1 and β1 subunits, and is dependent on the heme ligation state of the β1 H-NOX domain, as well as the ability of the catalytic domains to form a heterodimer.

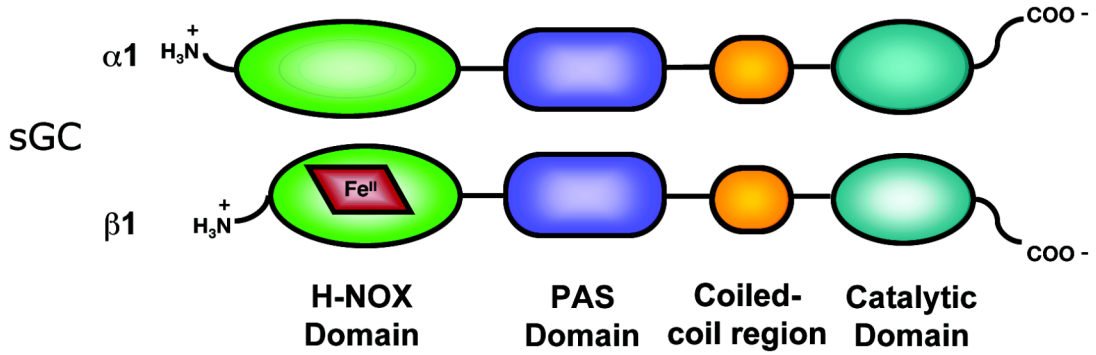

Figure 1.2 Schematic representation of sGC domain architecture. sGC forms a heterodimer consisting of two homologous subunits (α1 and β1). Although each subunit contains an H-NOX domain, a PAS domain, a coiled-coil region, and a catalytic domain, only the β1 subunit binds heme via a His-105 residue. Adapted from Derbyshire *et al*. [27].

Previous studies identified the first 194 amino acids of the β1 subunit as the minimal residues necessary to encode the heme-binding region of sGC [34]. Furthermore, the heme is bound to this region via a proximal histidine linkage (H105, rat β1 numbering). The activation of sGC is thought to involve the breaking of this Fe-His linkage upon binding NO to form a 5-coordinate, low spin complex [26, 32, 35]. This induced Fe-His bond rupture would then reorient the histidine ligand, initiating an overall protein conformational change that could translate to the catalytic domain of sGC. CO also activates sGC through the formation of a 6-coordinate, low spin complex [35]. However, the rate of cGMP production is only 2-4 times faster than basal level compared to activation by NO, which increases the production rate by several hundred-fold. Addition of the benzylindazole derivative, YC-1, to the sGC CO complex leads to its full activation; thus, it is postulated that this molecule interacts with the proximal side of the protein to induce a conformation that weakens the Fe-His bond and mimics the 5-coordinate NO conformer [36, 37].

1.2 The H-NOX family of heme proteins

The *H*eme *N*itric oxide/*OX*ygen (H-NOX) binding domain emerged in 2003 as a new family of heme proteins, encompassing domains from both eukaryotic and prokaryotic organisms [1, 2]. Its name derives from the fact that this family has evolved to contain proteins with divergent properties: those that bind NO, O_2, and CO, and others that discriminate against O_2 binding. Prior to the discovery of these prokaryotic heme domains and the reclassification of the sGC heme domain as part of the H-NOX family of proteins, sGC was exclusively associated with other mammalian nucleotide cyclases, such as adenylate cyclase and particulate guanylate cyclase [26, 27].

As previously mentioned, sGC has evolved in nature to selectively bind NO in the presence of much higher levels of O_2 even though it contains the same protoporphyrin IX chromophore as the globins. The ability of sGC to discriminate against O_2 is critical toward its role as a sensitive NO sensor, and the question of how this discrimination occurs at a molecular level has been pursued over the last three decades. Many proposals have emerged over the years to explain the selectivity of sGC, including the presence of a negative polarity in the distal pocket, steric bulk, and a weak Fe-His bond [26, 27, 32, 34, 38-41]. Upon discovery and examination of the prokaryotic H-NOX domains with their divergent ligand binding properties, more structural and biochemical studies revealed other qualities that were plausibly responsible for excluding O_2-binding in sGC [1, 5, 34, 38, 42-45].

1.2.1 Homologs to the β1 domain of sGC

A PSI-BLAST search into the genomic database produced a number of homologous prokaryotic heme proteins sharing up to 40% sequence identity with the β1(1-194) region of sGC [1, 2, 5] (Figure 1.3). In addition to homodimeric cyclases from the eukaryotes, *C. elegans* and *D. melanogaster*, this family of homologous proteins also

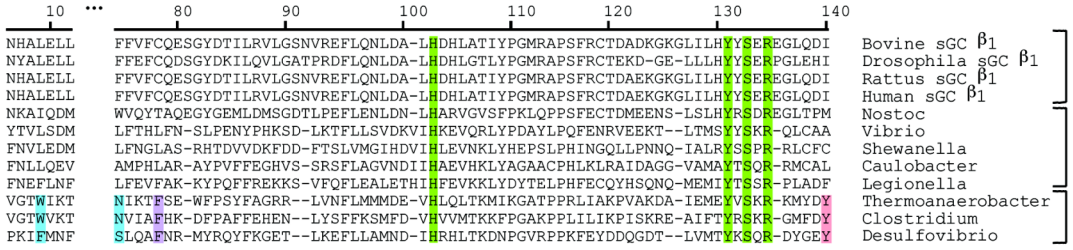

Figure 1.3 Partial sequence alignment of the H-NOX family showing the conserved heme-binding proximal histidine and Tyr-Ser-Arg (YxSxR) motif. Sequences from both eukaryotic and prokaryotic organisms (*i.e.* facultative aerobes and obligate anaerobes) are included. H-bonding distal pocket residues are highlighted in the H-NOX sequences from the obligate anaerobes. Adapted from Boon *et al*. [38].

included predicted open reading frames (ORFs) from both prokaryotic facultative aerobes and obligate anaerobes. These predicted ORFs were typically linked with histidine kinases and methyl-accepting chemotaxis (MCP) domains, respectively. Based on the diversity of these adjacent domains, it is thought that an early progenitor H-NOX domain existed from which the present ones evolved in order to accommodate the varied signaling functions involved with the sensing of O_2 or NO (Figure 1.4).

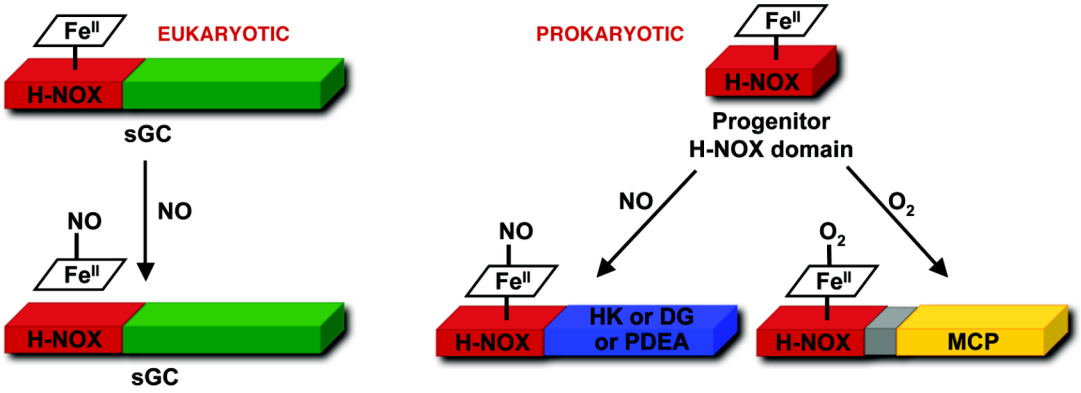

Figure 1.4 Divergence of ligand binding and H-NOX function in eukaryotic and prokaryotic organisms. Similar to sGC, the H-NOX domains in facultative aerobes do not bind O_2, and are often found adjacent to histidine kinases or diguanylate cyclases; whereas those from obligate anaerobes, such as *Thermoanaerobacter tengcongensis*, bind O_2 and may be part of a methyl-accepting chemotaxis protein (MCP).

Composed of ~190 residues, these prokaryotic proteins share several other conserved amino acids with β1(1-194) in addition to the proximal histidine linkage. Of particular importance is the Tyr-Ser-Arg (YxSxR) motif, which is known to assist heme binding and orientation via hydrogen bonds to the heme propionate groups, and a conserved proximal proline residue that influences heme conformation. Based on early bioinformatics and sequence analyses of these predicted ORFs, Iyer *et al.* initially classified this family of proteins as the *H*eme *N*itric *O*xide *B*inding (HNOB) domain based on their similarity to the NO-sensing sGC [2]. However, later work by Karow *et al*. conclusively showed that whereas some proteins bind NO and CO like sGC, others can additionally bind O_2; thus, the family was renamed the *H*eme *N*itric oxide/*OX*ygen (H-NOX) binding domain to reflect these different ligand binding properties within the group of heme proteins [1].

1.2.2 Structural and biochemical characterization

The N-terminal 188 amino acids of the predicted MCP, Tar4, comprise the H-NOX domain from the thermophilic obligate anaerobe, *Thermoanaerobacter tengcongensis*

(*Tt* H-NOX), and is fused to the MCP through two membrane-spanning regions [5, 44]. Unlike sGC, this H-NOX domain binds O_2 with very high affinity (K_d = 90 nM), in addition to NO and CO [1]. The O_2-bound *Tt* H-NOX domain was the first protein of its family to be structurally determined via x-ray crystallography [5, 46]. Solved to 1.77 Å by Pellicena *et al*., this crystal structure revealed a unique fold consisting of 7 alpha helices and 4 beta strands (Figure 1.5). Furthermore, it was shown that a distal tyrosine residue at position 140 (*Tt* numbering) interacted with the bound O_2 via a hydrogen-bonding network that included Trp-9 and Asn-74. Sequence homology models with the non-O_2-binding H-NOX domains indicated that they lacked this distal tyrosine residue, typically having a nonpolar residue in its place [38] (Figure 1.3). This discovery led to the hypothesis that the lack of a tyrosine residue in the distal pocket of sGC was responsible for its ability to discriminate between NO and O_2 [1, 38, 39, 47].

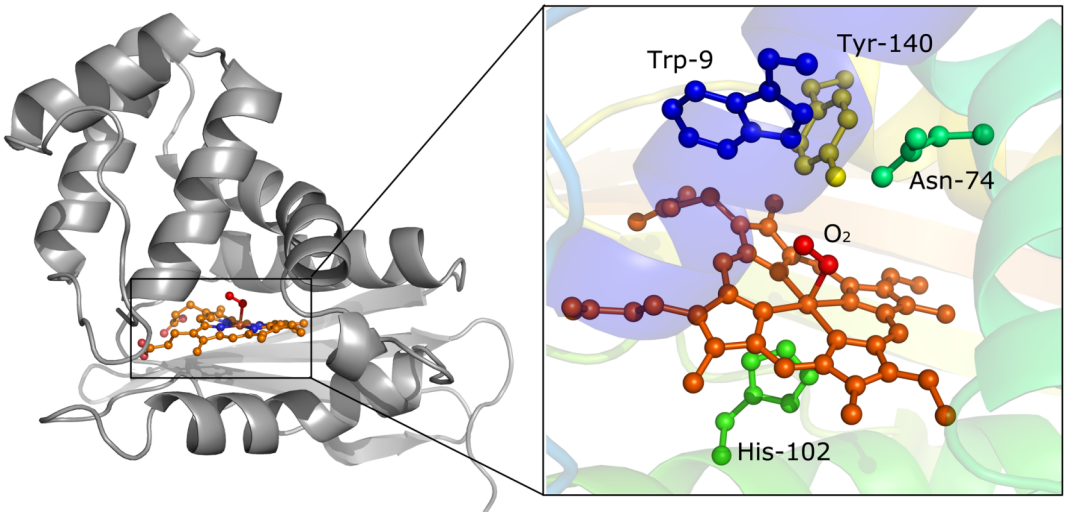

Figure 1.5 Structural features of the H-NOX domain from *T. tengcongensis*. O_2-bound *Tt* H-NOX protein fold and zoomed-in detail of heme-binding pocket with hydrogen-bonding distal residues (Trp-9, Asn-74, and Tyr-140) and proximal His-102 displayed (PDB 1U55).

One of the most striking features in the *Tt* H-NOX crystal structure was the severe heme distortion from planarity. Normal mode structural decomposition (NSD) [48-50], on the heme coordinates indicated that the extent of heme distortion observed in *Tt* H-NOX had not previously been measured [5]. It has been postulated that this deformation may be coupled to changes on the molecular surfaces of the H-NOX domain, and subsequently lead to differences in intermolecular interactions that to signal transduction in the protein [5, 44, 51]. Through energy minimization calculations, Pellicena *et al.* found that the Ile-5, Pro-115, and Leu-144 residues were responsible for the observed heme deformation in *Tt* H-NOX, with the Ile-5 predicted to be most important for maintaining this distorted conformer [5]. Subsequent crystallographic and spectroscopic studies on *Tt* H-NOX mutants at these residue

positions indicated that a single P115A mutation was sufficient to significantly relax the heme prosthetic group [44, 51].

X-ray crystallographic and NMR solution structures of other H-NOX domains from *Nostoc sp* (*Ns* H-NOX) and *Shewanella oneidensis* (*So* H-NOX) that do not bind O_2 have also been determined [42, 43]. These additional structures have provided insight into the ligand-induced conformational changes in the protein that may be involved in signal transduction. To investigate the differential enzyme activation responses to NO and CO by sGC, Ma *et al*. solved the crystal structures of the ligand-free, NO-bound, and CO-bound complexes of *Ns* H-NOX as a model system [43]. Comparing the different structures, they conjectured that the heme played a role in the activation mechanism by functioning as a flexing wedge that would initiate the H-NOX N-terminal subdomain to undergo a ~20° rotational shift upon transition between the 6- and 5-coordinate NO states. Erbil *et al*. proposed a similar mechanism with their "heme strain model" after determining the solution structures of the CO-bound WT *So* H-NOX domain and a H103G(imidazole) mutant [42]. These two forms were selected for the NMR study to mimic the ligand-free and kinase-inhibitory 5-coordinate NO-bound *So* H-NOX, which both contain paramagnetic hemes. Comparison of the NMR structures also demonstrated a rotational shift of the H-NOX distal subdomain upon loss of the axial histidine bond, and further supported the potential role of this subdomain movement in signal transduction.

1.2.3 Ligand discrimination in the H-NOX family

Previous studies on the H-NOX proteins indicate that those which originate from obligate anaerobes contain a distal hydrogen-bonding residue, and are able bind O_2 in addition to NO and CO. Interestingly, H-NOX proteins from the facultative aerobes resemble sGC in their ligand binding properties, and discriminate against O_2, binding only to NO and CO [1, 34, 38, 52]. From sequence alignments (Figure 1.3), it became apparent that the O_2-binding H-NOX domains contained distal hydrogen-bonding residues, whereas the non-O_2-binding residues lacked this property. The x-ray crystal structure of the O_2-bound WT *Tt* H-NOX domain demonstrated the importance of the distal Tyr-140 when it was found to be within hydrogen-bonding distance to the O_2 ligand, and presumably stabilized the O_2-bound heme complex in a manner similar the globins [5, 53].

Spectral and kinetic characterization of a series of *Tt* H-NOX distal pocket mutants targeting these hydrogen bonding residues (Figure 1.5) indicated a clear effect on the O_2 affinity [38]. To test the importance of a distal pocket tyrosine in O_2 stabilization, Boon *et al*. generated an F142Y mutation in the H-NOX distal pocket of *Legionella pneumophila* (*Lp* H-NOX2) and an I145Y mutation in the heme domain of sGC, β1(1-385) in order to introduce O_2-binding in these proteins [38]. Based on the similarity of electronic absorption spectra with the O_2-bound *Tt* H-NOX domain and a measured K_d of ~70 mM for the β1(1-385) I145Y mutant, Boon *et al*. concluded that the primary

molecular factor for ligand discrimination against O_2 in sGC was the absence of a distal tyrosine residue [38].

However, Rothkegel *et al*. showed that replacing Ile-145 with tyrosine in full length sGC did not confer the ability to bind O_2 [54]. Interestingly, Martin *et al*. additionally found that this substitution destabilized the sGC-NO complex and impeded the NO association [41]. Thus, the full mechanism of O_2 exclusion in sGC remains unclear, but it must include other contributing factors in addition to the absence of a hydrogen-bonding distal residue. To elucidate these properties, more structural information on the full-length enzyme will be necessary.

1.3 Probing heme structure with resonance Raman spectroscopy

Metalloporphyrins are one of the most widely studied classes of molecules via Raman spectroscopy. The two low-lying π-π^* electronic transitions from the aromatic porphyrin ring can be conveniently excited by wavelengths in the visible region (Figure 1.6), making modes that are coupled to the electronic transition readily accessible via resonance enhancement. In addition, a wealth of information can be obtained from the vibrational frequencies due to their sensitivity to porphyrin geometry and electronic structure. Thus, resonance Raman spectroscopy has emerged over the years as a powerful tool for probing the metalloporphyrin structure and geometry *in situ* within proteins.

Combining vibrational analysis with isotopic substitution is also an invaluable asset to better understanding heme RR spectra; the ability to specifically label regions of the porphyrin allows for accurate assignments and a detailed description of the vibrational modes. In particular, the use of $^{18}O_2$, ^{13}CO, and ^{15}NO has enabled the unambiguous assignment of modes involving these ligands; this is especially useful for probing interactions between the heme complex and protein environment. When used in conjunction with site-directed mutagenesis, one can directly observe the influence of specific residues within the protein pocket on the metal-ligand bond strength and conformation.

1.3.1 Resonance effect in Raman spectroscopy

In traditional non-resonance Raman spectroscopy, a molecule is irradiated with a laser wavelength in a spectral region that is far removed from the electronic absorption features of the molecule. Under these conditions, the scattered radiation is generally weak and so a high solute concentration is typically necessary to acquire adequate data.

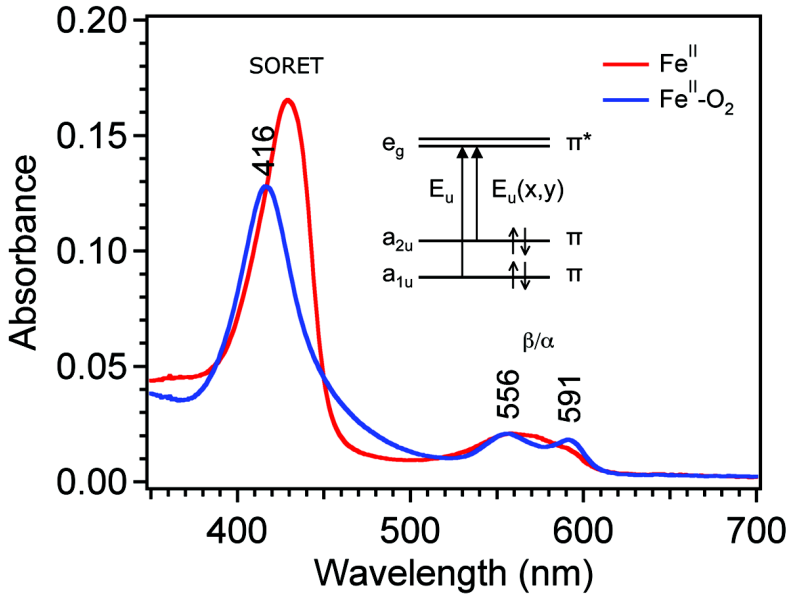

Figure 1.6 Electronic absorption spectra of Fe^{II} and Fe^{II}-O_2 *Tt* H-NOX. The Soret and α/β region are clearly labeled. A schematic representation of the simplified Gouterman four-orbital model for porphine is included for reference [55]. Due to configuration interaction, the transition dipoles of the two indicated π-π* transitions either combine constructively to produce a higher energy transition (Soret band) or destructively to produce a lower energy transition (α/β bands). Adapted from Spiro *et al*. [56].

In contrast, the Raman scattering from a specific chromophore can be significantly increased by a factor of 10^3 up to 10^6 once the excitation wavelength falls within or near the electronic absorption band of the chromophore, selectively amplifying the vibrational features of the absorbing molecule via resonance enhancement [57, 58]. In this process, only the skeletal vibrations of the absorbing chromophore are magnified, leaving the vibrational features from the non-absorbing species weak. As described by Albrecht *et al*., there are two main Raman scattering mechanisms: A-term and B-term scattering [57, 59, 60]. The Albrecht A-term is the dominant resonance scattering mechanism for allowed electronic transitions, and relative enhancements for different totally symmetric vibrational modes depend on the Franck-Condon overlap from the transition [56]. In contrast, the B-term scattering Raman intensities are not Condon derived for the non-totally symmetric modes, and typically gain intensity via vibronic mixing with strongly allowed transitions [58-60].

Figure 1.7 primarily describes the Franck-Condon activated A-term resonance Raman scattering process [57, 59, 61]. In this process, a molecule starts out in the initial vibrational eigenstate, $|i\rangle$, of the ground electronic state and is projected onto the

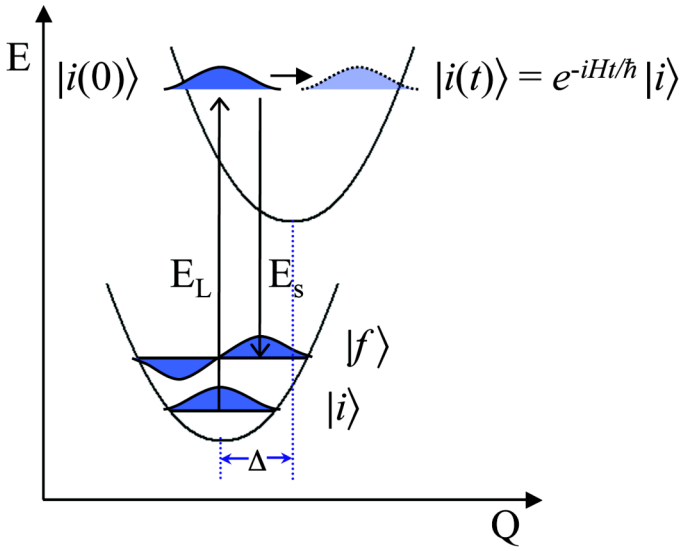

Figure 1.7 Time-dependent picture of resonance Raman enhancement. The resonance Raman intensity amplitude is directly proportional to the integrated overlap between the propagating wavepacket, $|i(t)\rangle$, and the final vibrational state in the Raman transition, $|f\rangle$. Significant overlap is achieved for vibrations with large displacements (Δ) along their nuclear coordinates upon electronic excitation. Adapted from Myers *et al*. [57].

excited state surface upon interaction of its electronic transition moment (*eM*) with incident radiation of energy, E_L. On this excited state surface, $|i\rangle$ evolves with time under the influence of the excited state Hamiltonian operator. As $|i(t)\rangle$ moves along the excited state surface over time, the overlap between $|f\rangle$ and $|i(t)\rangle$ changes. The Raman intensity for a specific mode depends on the integrated Franck-Condon overlap between the propagating wavepacket ($|i(t)\rangle$) and the final vibrational eigenstate, $|f\rangle$. This dependence is evident in the expression for the Raman cross-section [$\sigma_{i\to f}(E_L)$], which is defined as:

$$(1) \qquad \sigma_{i\to f}(E_L) = \frac{8\pi E_s^{\,3} E_L e^4 M^4}{9\hbar^6 c^4}\left|\int_0^\infty \langle f|i(t)\rangle \exp\left[\frac{i(E_L+\varepsilon_i)t}{\hbar}\right] e^{-\Gamma t/\hbar} dt\right|^2$$

where E_s and E_L indicate the scattered and incident photon energies, *M* is the electronic transition length, $|i\rangle$ and $|f\rangle$ are the initial and final vibrational states involved in the Raman transition, ε_i corresponds to the energy of the initial vibrational state, Γ is the homogeneous linewidth of the excited state, and $|i(t)\rangle$represents the propagating wavepacket on the excited state surface [57]. In order for $|i(t)\rangle$ to gain good overlap with $|f\rangle$, the ground and excited state surfaces must be significantly displaced; hence, only the vibrations along which a large distortion occurs upon electronic excitation are

resonantly enhanced. Too little displacement between the two surfaces results in a poor overlap between $|i(t)\rangle$ and $|f\rangle$, so the Raman intensity is hardly enhanced for these vibrations [57].

For application to heme proteins, a stable source of high intensity, monochromatic radiation from a continuous wave (CW) krypton ion (Kr^+) laser provides the majority of the necessary excitation wavelengths (*e.g.* 406.7 nm, 413.1 nm, 568.2 nm, 647 nm) to obtain resonance with either the Soret or α/β bands of a heme prosthetic group (Figure 1.6). The main instrumental components of the Raman spectrometer generally include an excitation source, sample holder, focusing lens, collection optics, polarizer, polarization scrambler, monochromator (*e.g.* double), and a charge-coupled device (CCD) for digital detection (Figure 1.8). The use of a double monochromator over a single one can significantly cut back on incident (Rayleigh) light scattering.

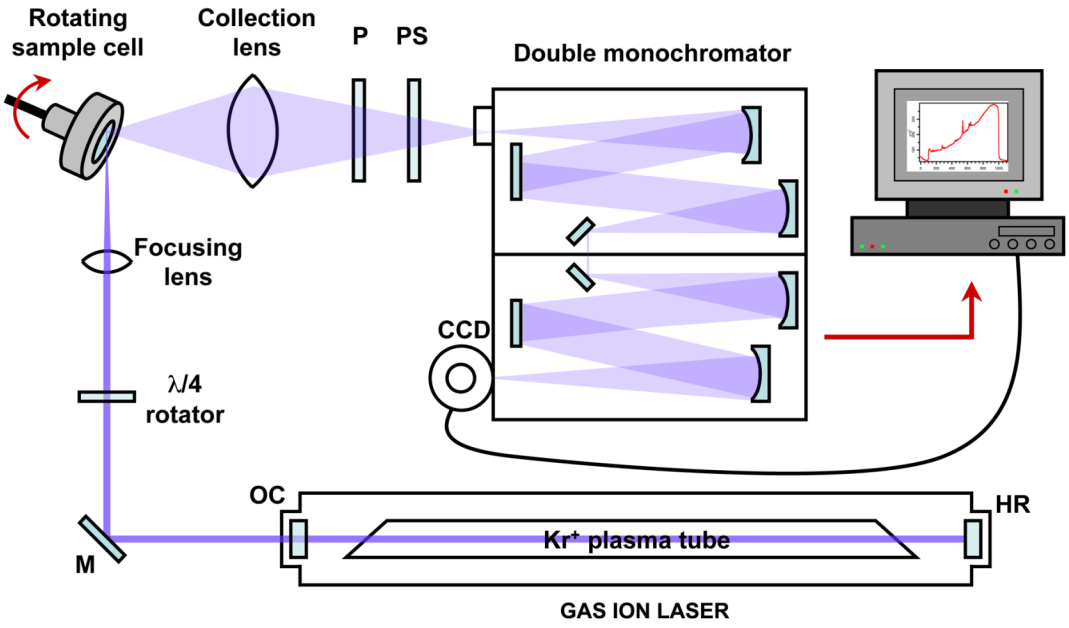

Figure 1.8 Schematic diagram of data collection in Raman spectrometer. A focused CW laser beam from a Kr^+ source irradiates the sample held in the rotating cell, which is oriented in a backscattering geometry. The scattered light is collected and focused by the collection optics, passing through a polarizer (P) and polarization scrambler (PS) to the entrance slit of the double monochromator, where it is dispersed by two diffraction gratings. The Raman lines are then detected by the charge-coupled-device (CCD) for digital conversion on a computer. (OC = output coupler, HR = high reflector).

To prevent photodegradation of the absorbing species, microspinning sample cells (with holding volumes of 50-500 μL) are usually utilized. In typical Raman experiments, the

polarizer is oriented so that the electric vector of the scattered radiation lies parallel to the electric vector of the linearly-polarized incident light [58]. The depolarization ratio, defined as $\rho = I_{\perp}/I_{\parallel}$, can be obtained by collecting Raman spectra with the polarizer oriented either perpendicularly or parallel to the incident light, and is a characteristic property that is specific to the molecular and vibrational symmetry [58].

1.3.2 Heme skeletal modes and structural implications in proteins

Upon selection of an excitation wavelength that overlaps with the Soret band of the heme chromophore, the main features that are observed in the resonance Raman spectrum involve totally symmetric in-plane breathing modes from the porphyrin ring (Figures 1.9 and 1.10). Fluorescence is usually not a problem due to quenching by the the heme iron. The most structure sensitive bands occur in the 1350-1650 cm^{-1} region, and are highly influenced by the oxidation state, spin state, and coordination state [62]. In the high frequency region, the most intense resonance Raman feature is typically found between 1350-1380 cm^{-1} and corresponds to the C_{α}-N pyrrole-breathing mode (ν_4). Due to its sensitivity to the oxidation state of the iron, as well as the occupancy of the porphyrin π^* orbitals upon ligand binding, ν_4 is typically referred to as the π-electron density marker [56]. Other significant heme skeletal markers involve C_{α}-C_m (ν_3 and ν_{10}) and C_{β}-C_{β} (ν_2) stretching vibrations; the frequency of these modes are highly influenced by the spin and coordination states of the heme group, and can also reflect changes in the heme conformation or core size. In addition, both the frequency and intensity of these heme skeletal modes may be further modulated by the surrounding protein environment, providing a very sensitive probe of the binding site.

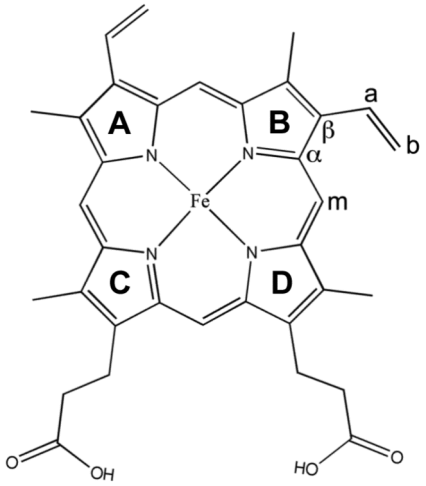

Figure 1.9 Chemical structure of heme. Selected carbon atoms are labeled using the C_{α}, C_{β}, and C_m nomenclature for resonance Raman skeletal modes. Pyrrole groups are labeled as defined by Pellicena *et al*. [5].

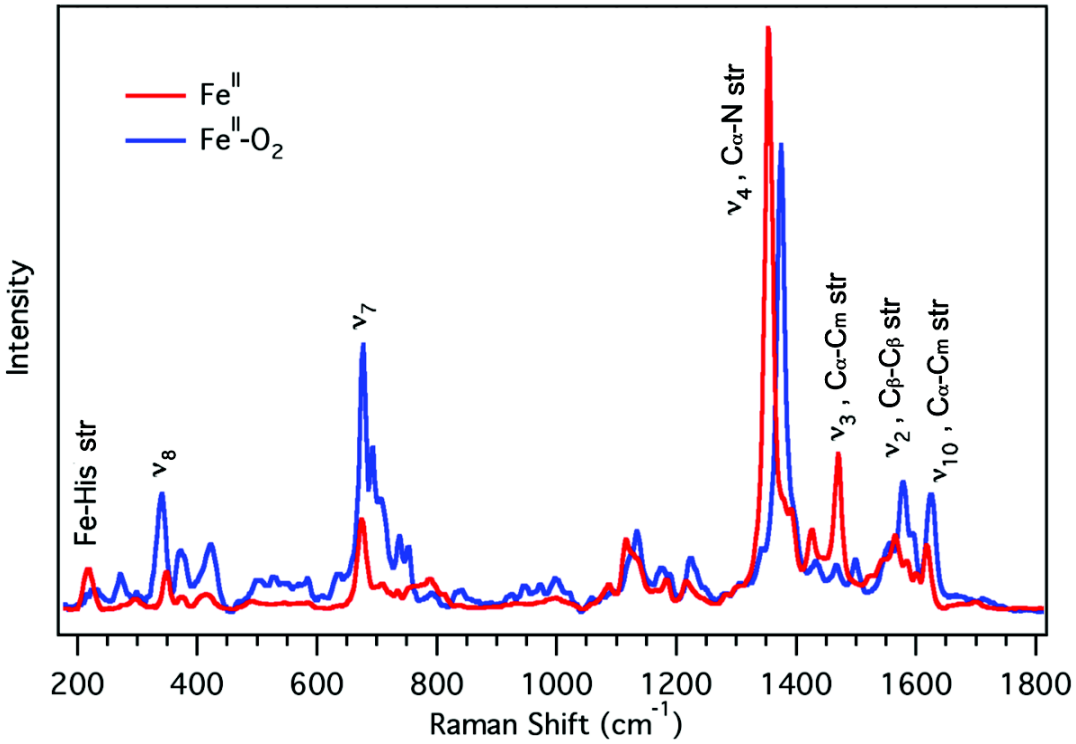

Figure 1.10 Resonance Raman spectra of *Tt* H-NOX with labeled skeletal modes. An example of resonance Raman spectra of *Tt* H-NOX in the 5-coordinate ferrous unligated form (red), and 6-coordinate O_2 complex (blue), indicating the locations and relative intensities of different porphyrin vibrational modes.

Due to direct coupling with the porphyrin π-π^* transitions, one can also observe Fe^{II}-ligand modes such as ν(Fe-His) or ν(Fe-O_2). These modes typically occur in the low frequency region, and provide a direct measurement of the bond strength. In particular, the Fe-His stretching mode provides insight into interactions between the proximal histidine ligand and the surrounding protein matrix [63]. Other useful information can be obtained from examining this 150-1050 cm^{-1} region of the resonance Raman spectrum. The intensity of certain heme out-of-plane (oop) modes (*e.g.* pyrrole folding or swiveling deformations) can reveal information about the conformation of the chromophore. In addition, vibrational shifts in the low frequency region (*e.g.* ~378 cm^{-1}, ~420 cm^{-1}) may indicate differences in how the heme substituent groups interact with nearby residues. These bands from the substituents are resonantly enhanced due to coupling with the porphyrin core [56].

Both steady-state and time-resolved resonance Raman spectroscopy have been extensively utilized over the last three decades to understand the mechanisms by which ligand binding to a heme sensor domain transfers signal to the functional domain [36, 37, 56, 58, 62-83]. Several examples of these ligand-binding heme sensor proteins studied via resonance Raman spectroscopy include the NO-sensing enzyme sGC, the

O_2-sensing FixL and direct oxygen sensor (DOS), and the CO-sensing CooA. Specifically, these studies have shown that three main pathways exist by which the heme can convey signal to the functional domain upon ligand binding: (i) the distal pocket, (ii) the proximal pocket, and (iii) along the heme periphery. The determination of the particular pathway may be detected through the changes in vibrational frequency and/or Raman intensity of the heme-associated modes. Thus, in combination with site-directed mutagenesis, RR spectroscopy is a direct method to probe the active site of the solution protein for ligand bond strength modulation, heme conformational changes, or cleavage of hydrogen bonds with surrounding amino acids.

1.4 Thesis

Resonance Raman spectroscopy has been well established as an effective tool for investigating protein-ligand interactions in heme proteins [56, 58, 63, 82, 84]. In this thesis, a biophysical approach was taken using resonance Raman spectroscopy to elucidate the binding interactions between the H-NOX domain and different exogenous ligands, as well as the electrostatic and steric interactions that occur in solution using *Tt* H-NOX as a model system. The role of several conserved residues, including Pro-115, in maintaining the heme conformation in *Tt* H-NOX has been investigated via resonance Raman spectroscopy and is discussed in Chapter 2. In addition, the structural determinants that modulate the back-donation of electrons from Fe^{II} d_π to CO π^* in the H-NOX family were examined through a combination of site-directed mutagenesis, resonance Raman spectroscopy, and isotopic substitution. This spectroscopic characterization of the CO complex in *Tt* H-NOX and different mutants is discussed in Chapter 3. Furthermore, previous work by Boon *et al*. established a link between O_2 affinity and the presence of a hydrogen-bonding tyrosine in the H-NOX distal pocket [38]. Kinetic studies by Weinert *et al*. also showed changes in the O_2 affinity upon the addition of steric bulk to the protein pocket [45]. In Chapter 4, the O_2 binding properties of *Tt* H-NOX upon disrupting different heme pocket features is examined spectroscopically with isotope substitution. Finally, Chapter 5 summarizes the contributions of these resonance Raman studies and presents recommendations for future experiments to further elucidate the properties of the H-NOX family, providing insight into its protein-ligand interactions and mechanism of ligand discrimination.

Chapter 2

Resonance Raman Spectra of an O_2-Binding H-NOX Domain Reveal Heme Relaxation upon Mutation

2.1 Abstract

Resonance Raman spectra are measured for *Tt* H-NOX WT and three other *Tt* H-NOX proteins containing mutations at key conserved residues to determine the heme conformation in solution. The most dramatic changes in heme conformation occurred in the O_2-bound forms, and the single *Tt* H-NOX P115A mutation was sufficient to generate a significant relaxation of the chromophore. Clear evidence of heme relaxation in the *Tt* H-NOX I5L, P115A, and I5L/P115A mutants in solution is demonstrated by the observation of reduced resonance Raman intensities for several out-of-plane low frequency modes (*e.g.* γ_{11}, γ_{12}, γ_{13}, and γ_{15}) in the 400-750 cm^{-1} region known to be sensitive to ruffling and saddling deformations, as well as increased vibrational frequencies for the core heme skeletal stretching modes, ν_3, ν_2, and ν_{10}. In addition, all three mutants exhibited some degree of heme conformational heterogeneity based on several broad skeletal markers (*e.g.* ν_{10}) in the high frequency region. These results are comparable to those observed by Olea *et al.* for *Tt* H-NOX P115A in crystal form, where four different heme structures were determined from a single unit cell. Based on the resonance Raman spectra, it is clear that the actual heme conformation for *Tt* H-NOX P115A in solution is considerably more relaxed than WT, with increased flexibility within the protein pocket, allowing for rapid sampling of alternate conformations.

2.2 Introduction

Nonplanar porphyrin conformations are of great interest and widely investigated due to their potential role in regulating biochemical properties and activity in proteins containing either heme or chlorophyll cofactors [48, 50, 85-89]. Over the last three decades, several methods have been utilized to study these heme deformations in proteins. These include theoretical approaches using DFT and QM/MM methodologies [86, 89-91], vibrational spectroscopy of model compounds isolating specific distortions [65, 87, 88, 92, 93], and the normal coordinate structural decomposition (NSD) method developed by Shelnutt *et al.* [48-50] to quantify specific heme deformations observed in x-ray crystal structures. In nature, some of the largest heme deformations typically occur in the c-type cytochromes and peroxidases with out-of-plane displacements greater than 1 Å [50]. However, recent crystallographic work by Pellicena *et al.* shows that the *H*eme-*N*itric oxide/*OX*ygen binding (H-NOX) domain from *Thermoanaerobacter tengcongensis* also contains a highly distorted heme structure [5]. Subsequent H-NOX crystal structures indicate that the heme chromophore can sample a range of nonplanar conformations [43, 46].

The H-NOX family of heme proteins has the unique property that some proteins bind only NO and CO, whereas others additionally bind O_2 [47, 94]. The first crystal structure obtained within this family was the O_2-bound H-NOX domain from the bacterial obligate anaerobe, *Thermoanaerobacter tengcongensis* (*Tt* H-NOX) [5]. One of the most distinctive features about this O_2-bound structure is the significant heme deformation (Figure 2.1a). Energy minimization calculations by Pellicena *et al.* predicted that Ile-5, Pro-115, and Leu-144 maintained nonbonded contacts with the heme, inducing this observed deformation in *Tt* H-NOX [1, 5]. Of those three residues, Pro-115 is of particular interest since it is conserved within this family. Thus, a key focus in investigating these H-NOX domains is to better understand how these conserved residues may contribute towards regulating heme distortion, and thereby possibly controlling ligand specificity.

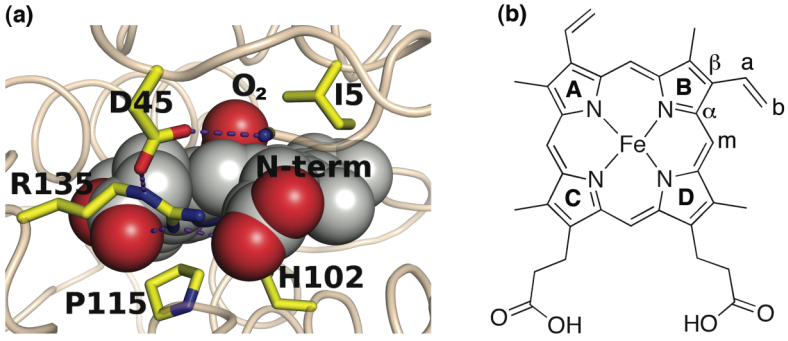

Figure 2.1 (a) Structure of the heme pocket of the *Tt* H-NOX WT Fe^{II}-O_2 complex, indicating the distal Ile-5 and proximal Pro-115 thought to be responsible for the distorted heme structure (PDB 1U55). (b) Heme molecular structure and labeling scheme.

Recently, Olea *et al*. have shown via x-ray crystallography that mutating Pro-115 to alanine in *Tt* H-NOX alters the protein pocket such that the heme relaxes and samples several conformations, including more planar structures than that observed in the WT protein [44]. However, the presence of four different heme structures in the unit cell complicated the determination of which conformation is actually dominant in solution. To address this question, a different technique that can probe the heme structure in solution is required.

Because of its selectivity and sensitivity to molecular structure, resonance Raman spectroscopy is an invaluable tool for specifically probing protein-bound heme conformations in solution (Figure 2.1b). Detailed information on the ground state geometry and electronic structure can be obtained from the vibrational frequencies; furthermore, the RR intensities provide insight into the symmetry and equilibrium geometry, and may be used to probe excited state dynamics [56, 57]. In addition, RR spectroscopy is useful for investigating heme deformations because the distortions within the chromophore cause frequency shifts in the skeletal stretching modes (denoted as "ν") and activate the intensity of low frequency out-of-plane (oop) modes (denoted as "γ") [50, 56, 79, 88].

In this study, we use resonance Raman spectroscopy to investigate the effects of mutating the distal Ile-5 and proximal Pro-115 residues in *Tt* H-NOX on the heme structure. The spectra show that these residues are important in *Tt* H-NOX for maintaining a specific protein environment, and that mutating Ile-5 and Pro-115 relaxes the solution chromophore conformation for the O_2 complexes. Specifically, our RR spectra suggest that the single P115A mutation leads to the largest change in the heme structure, whereas the *Tt* H-NOX I5L and I5L/P115A double mutants maintain conformations that are more similar to *Tt* H-NOX WT. These conformational changes likely occur as a consequence of heme pocket rearrangements to accommodate the substituted residues. We compare these relaxations to the quantified changes observed in crystal form using the normal coordinate structural decomposition (NSD) analysis developed by Shelnutt *et al.* [48-50, 92].

2.3 Experimental Procedures

2.3.1 Protein expression and purification

Expression and purification of the Tt H-NOX domain were performed as previously described [1] with the following modifications. Thawed cell pellets resuspended in buffer A [50 mM TEA, 20 mM NaCl, 5% glycerol, 1 mM Pefabloc (Pentapharm), pH 7.5] were lysed at 4 °C with an Emulsiflex-C5 high-pressure homogenizer at 15000 psi (Avestin, Inc.) upon addition of DNAse I and lysozyme (Sigma). Lysed cells were centrifuged for 1 h at 42000 rpm at 4 °C, and the supernatant was heat-denatured at 75 °C for 45 min. The denatured protein was centrifuged again for 1 h at 42000 rpm, and the supernatant was concentrated to < 10 mL using 10 K MWCO spin concentrators

(Vivaspin). Concentrated protein was then loaded onto a prepacked Superdex S75 Hiload 26/60 gel filtration column (Pharmacia) equilibrated with buffer A, and fractions containing Tt H-NOX were pooled and applied to a POROS HQ 7.9 mL (1 × 10 cm, 10 mm) anion-exchange column (Applied Biosystems) at 5-10 mL/min. Flow-through containing the Tt H-NOX domain was collected and stored at -80 °C. Site-directed mutagenesis was carried out using the QuikChange® protocol (Stratagene), and verified by sequencing (UC Berkeley sequencing core).

2.3.2 Sample preparation

The purified Tt H-NOX protein was brought into an anaerobic glovebag, and oxidized using ~5-10 mM potassium ferricyanide to remove the bound O_2. The ferricyanide was removed using a PD10 desalting column (Amersham Biosciences) equilibrated with buffer B (50 mM TEA, 50 mM NaCl, pH 7.5). Following oxidation and desalting, the protein was reduced with ~5-20 mM sodium dithionite that was removed using a PD10 desalting column upon complete reduction of the heme. The $^{16}O_2$ complexes were generated by opening the reduced protein to air. To make the $^{18}O_2$ (95% $^{18}O_2$; Cambridge Isotopes) complexes, gas was added to a sealed Reacti-Vial (Pierce) containing Fe^{II}-unligated protein. Commercially available horse heart myoglobin and horse muscle hemoglobin (Sigma) samples were prepared similarly. Final sample concentrations for the Raman experiments were typically 15 to 50 mM. All UV/Vis absorption samples were prepared and measured as previously described [1, 52].

2.3.3 Resonance Raman spectroscopy

All spectra were collected using the 413.1 nm line from a Kr^+ laser (Spectra-Physics model 2025) focused to a beam diameter of ~60 μm with a 50 mm focal-length excitation lens. Raman scattering was detected with a cooled, back-illuminated CCD (LN/CCD-1100/PB; Roper Scientific) controlled by an ST-133 controller coupled to a subtractive dispersion double spectrograph [95]. The laser power at the sample was ~2 mW, and a microspinning sample cell was used to minimize photoinduced degradation. Typical data acquisition times were 30 to 60 min. Electronic absorption spectra were obtained before and after the Raman experiments to verify that no photoinduced degradation occurred. Raman spectra were corrected for wavelength dependence of the spectrometer efficiency with a white lamp, and the instrument was calibrated using the Raman frequencies from cyclohexane, CCl_4, and toluene. The reported frequencies are accurate to ±1 cm^{-1}, and the spectral bandpass was set to 8 cm^{-1}. For each Raman spectrum, the raw data were baseline-corrected, and the buffer background signal was subtracted. Spectral analysis and decomposition were performed using Igor Pro (WaveMetrics). Isotopic shifts were approximated on the basis of a simple harmonic oscillator (HO) model.

2.3.4 Structural deformation analysis

To deconvolute the distortions from *Tt* H-NOX and other heme proteins, we used the web-based version of the normal-coordinate structural decomposition method (NSD) developed by Jentzen *et al.* to input our heme coordinates and quantify the deformations for the porphyrin macrocycle [48-50, 92]. This program uses a porphyrin reference of D_{4h}-symmetry to describe the heme distortions in terms of displacements along the lowest frequency out-of-plane normal coordinates within the molecule. The generated output quantifies the amount of each deformation type necessary to model the overall observed distortions within a given heme structure. Coordinates from previous crystal structures were obtained from the RCSB Protein Data Bank [5, 44, 53, 96-98]. For all proteins used in our NSD calculations, the heme is oriented such that the vinyl groups remain in quadrants I and II as defined by Jentzen *et al.* [48] in order to maintain the directionality in the absolute signs of the deformation types. In our analysis, the minimal basis set was used to quantify the different types of heme distortion. This basis set only includes the lowest frequency mode from each of the 6 in-plane and 6 out-of-plane normal deformations, and has been shown to adequately describe heme distortions in proteins [49]. The overall magnitude of out-of-plane distortions (Δ_{oop}) for the heme is defined as the square root of the squared sum of observed *z* axis displacements for the 24-atom porphyrin macrocycle ($C_{20}N_4$). This total out-of-plane distortion was determined from the complete basis set, which gives the total deformation of each symmetry type [49].

2.4 Results

2.4.1 Electronic absorption characterization

As an initial step toward characterizing the effects of mutating Ile-5 and Pro-115 in *Tt* H-NOX, we obtained electronic absorption spectra of the proteins with different ligands. Table 2.1 summarizes the Soret and α/β bands measured for *Tt* H-NOX in the unligated, CO, NO, and O_2-bound forms, and includes the globins for comparison [99]. Both the unligated and CO complexes show small changes in absorption upon mutating Ile-5 and Pro-115. The unligated *Tt* H-NOX WT spectrum displays a characteristic Soret at ~430 nm and a broad α/β band at ~563 nm, indicative of a 5-coordinate, high-spin species. Compared to *Tt* H-NOX WT, the P115A, I5L, and I5L/P115A mutants produce minor red shifts between 1-6 nm in the Soret and α/β bands. Addition of CO to the reduced, unligated *Tt* H-NOX WT protein shifts the electronic absorption features to display the Soret at ~423 nm and discernible α/β bands at ~567 nm and ~541 nm, confirming the presence of a 6-coordinate, low-spin CO complex. All three *Tt* H-NOX mutants display similar Soret values at 424 nm, but deviate by 1-3 nm in the split α/β band region compared to *Tt* H-NOX WT.

Table 2.1 Electronic absorption properties for *Tt* H-NOX, Hb, and Mb in the reduced and CO, NO, and O_2-bound forms.

Protein	Ligand	Soret	α/β	Ref.
Tt WT	reduced	430	563	[1]
Tt P115A		432	563	this work
Tt I5L		431	569	this work
Tt P115A/I5L		431	566	this work
Hb		430	555	[99]
Mb		434	556	[99]
Tt WT	CO	423	567/541	[1]
Tt P115A		424	568/538	this work
Tt I5L		424	565/541	this work
Tt P115A/I5L		424	570/542	this work
Hb		419	569/540	[99]
Mb		423	579/542	[99]
Tt WT	NO	420	575/547	[1]
Tt P115A		418	573/543	this work
Tt I5L		421	572/539	this work
Tt P115A/I5L		421	568/535	this work
Hb		418	575/545	[99]
Mb		421	575/543	[99]
Tt WT	O_2	416	591/556	[1]
Tt P115A		416	584/548	this work
Tt I5L		418	587/550	this work
Tt P115A/I5L		417	588/552	this work
Hb		415	576/541	[99]
Mb		418	580/542	[99]

[a] All peak positions are reported in nm.

Addition of NO to the reduced, unligated *Tt* H-NOX WT protein results in a 6-coordinate, low-spin NO complex (Soret: 420 nm, α/β bands: 575 nm and 547 nm). A slight blue shift of 2-4 nm is observed in the Soret and α/β bands for the *Tt* H-NOX P115A NO complex. Although the Soret only shifts to 421 nm for the *Tt* H-NOX I5L mutant, its α/β bands decrease by 3 and 8 nm to 572 and 539 nm, respectively. The largest blue shift is observed in the α/β region for the *Tt* H-NOX I5L/P115A mutant (7 and 12 nm, respectively).

As previously shown, *Tt* H-NOX produces a stable 6-coordinate, low-spin O_2 complex upon exposure of a reduced sample to air [1]. The mutants shift by 6-7 nm to shorter wavelengths in the α/β region compared to *Tt* H-NOX WT (Soret: 416 nm, α/β bands: 591 nm and 556 nm). The largest shift is observed for the *Tt* H-NOX P115A mutant with α/β bands at ~584 and ~548 nm.

In summary, the NO and O_2 complexes show consistent shifts in the α/β bands toward shorter wavelengths upon mutating Ile-5 and Pro-115 in *Tt* H-NOX, whereas the unligated and CO complexes exhibit both shorter and longer wavelength changes for the mutants. The overall changes observed in the electronic absorption spectra are relatively minor, but consistently reproducible. These observed shifts are plausibly introduced from structural rearrangements within the heme pocket, which then change the internal electric field. However, interpreting the changes in the α/β region is more complicated due to the different factors that influence its shape and splitting pattern, including contributions from electronic and vibronic perturbations, heme-protein interactions, and vibronic coupling strength redistributions [100].

2.4.2 Resonance Raman spectroscopy

To better characterize the effects of mutating Ile-5 and Pro-115 on the *Tt* H-NOX heme solution structure, we performed resonance Raman measurements on the unligated and oxygenated forms (Figures 2.2 and 2.3). The main heme skeletal marker bands, ν_4, ν_3, ν_2, and ν_{10}, are summarized in Table 2.2 and compared to other proteins [81]. The π-electron density marker (ν_4), assigned as the pyrrole breathing mode, varies between 1350-1380 cm^{-1} depending on the oxidation state of the heme. The spin and coordination state markers, ν_3, ν_2, and ν_{10}, correspond to C_α-C_m and C_β-C_β stretching vibrations in the macrocycle [56, 79]. Together, these skeletal markers in the 1350-1650 cm^{-1} region can be used to detect different conformations as a result of their sensitivity to the porphyrin core size and π-conjugation. In addition, the Fe-His stretching vibration at ~220 cm^{-1} is a sensitive probe of the bound histidine, providing unique structural details about the heme environment in the proximal pocket [63].

Table 2.2 Heme skeletal modes for the Fe^{II}-unligated and Fe^{II}-O_2 complexes of *Tt* H-NOX, hemoglobin, myoglobin, and FixL.[a]

Protein	Ligand	ν_{10}	ν_2	ν_3	ν_4	ν(Fe-X)	Ref.
Tt WT	unligated	1600	1565	1469	1353	217	[1]
Tt P115A		1602	1567	1469	1353	223	this work
Tt I5L		1599	1564	1469	1352	217	this work
Tt P115A/I5L		1601	1566	1471	1354	220	this work
Hb		nr[b]	1564	1470	1356	217	[101]
Mb		nr	1563	1471	1357	220	[101]
Bj FixLH[c]		1602	1555	1469	1353	218	[81]
Tt WT	O_2	1624	1579	1499	1375	567	[1]
Tt P115A		1631	1581	1503	1377	565	this work
Tt I5L		1627	1580	1499	1372	564	this work
Tt P115A/I5L		1630	1582	1502	1375	562	this work
Hb		nr	1581	1503	1376	570	this work
Mb		nr	1584	1506	1377	570	this work
Bj FixLH		1638	1579	1504	1377	569	[81]

[a] All vibrational frequencies are reported in cm^{-1}.
[b] nr = not reported.
[c] *B. japonicum* FixL heme-PAS.

The resonance Raman spectra of the fully reduced, 5-coordinate *Tt* H-NOX WT and P115A mutant were obtained to investigate the effect of the proximal Pro-115 mutation on the Fe-His bond strength. The vibrational frequencies and intensities are similar, with the exception of the 6 cm^{-1} increase for the Fe-His stretch to 223 cm^{-1} for P115A and a ~5 cm^{-1} increase in bandwidth. In the high frequency region, the skeletal markers at 1353, 1469, 1565, and 1600 cm^{-1} correspond to typical ν_4, ν_3, ν_2, and ν_{10} values for 5-coordinate, histidyl-ligated, high-spin heme proteins [64, 81, 102]. The striking spectral similarity between the *Tt* H-NOX WT spectrum and that of P115A in Figure 2.2 suggests that the heme conformation is minimally perturbed by this mutation, although the Fe-His bond length may have decreased slightly.

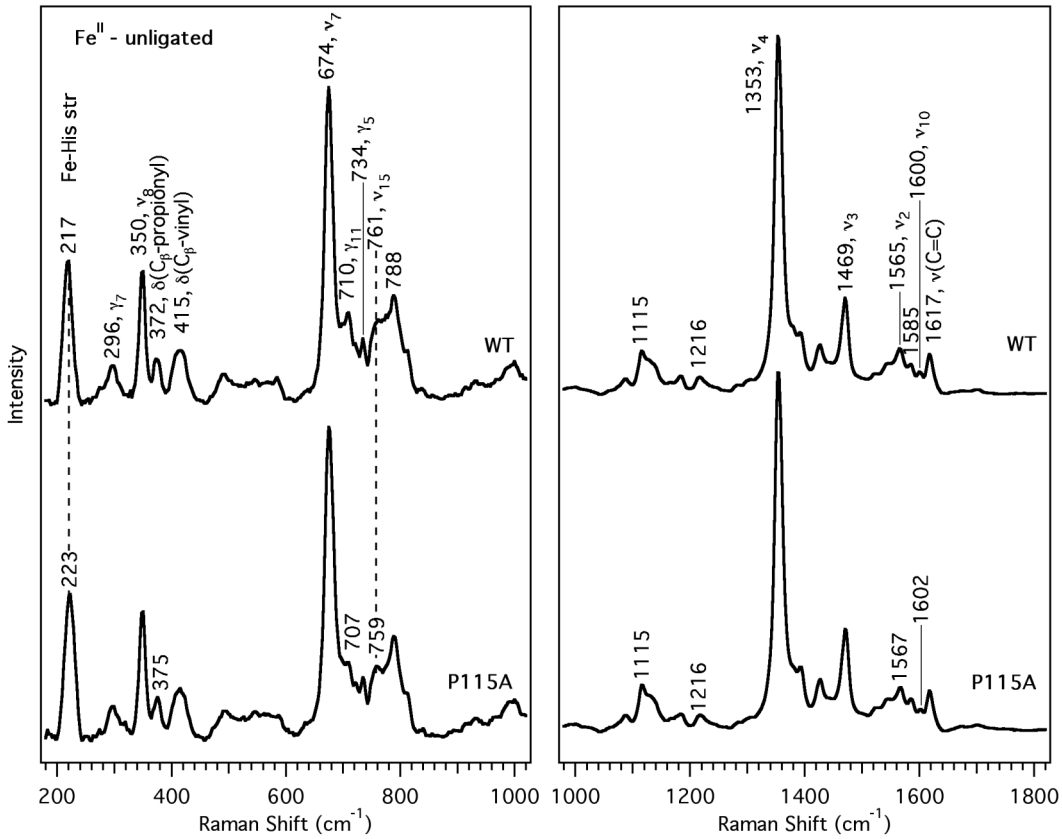

Figure 2.2 Resonance Raman spectra of the Fe^{II}-unligated form of *Tt* H-NOX WT (upper trace) and P115A (lower trace). Spectral intensities in the low and high frequency regions were normalized to ν_7 and ν_4, respectively.

The resonance Raman spectra of the O_2 complexes are compared in Figure 2.3 and the vibrational frequencies are also summarized in Table 2.2. The $^{18}O_2$-isotopically substituted RR spectra are indicated with dotted lines and overlaid upon the natural abundance O_2 complex spectra in the lower frequency region to assign the Fe-O_2 stretch (Figure 2.3, traces a-f). Based on the simple harmonic oscillator model, a downshift of 21 cm^{-1} is predicted for ν(Fe-O_2) upon $^{16}O_2 \rightarrow {}^{18}O_2$ substitution. As previously shown [1], *Tt* H-NOX WT displays a ν(Fe-O_2) band at 567 cm^{-1} which shifts to 540 cm^{-1} for the $^{18}O_2$ complex. Mutating Pro-115 and Ile-5 causes small downshifts of 2 to 5 cm^{-1} relative to *Tt* H-NOX WT. The *Tt* H-NOX P115A mutant exhibits an isotope-sensitive band at 565 cm^{-1} which decreases by 20 cm^{-1} for the $^{18}O_2$ complex, corresponding very well with the expected downshift. Similarly, ν(Fe-O_2) for the *Tt* H-NOX I5L/P115A double mutant is observed at 562 cm^{-1} and it decreases by 25 cm^{-1} upon $^{18}O_2$ substitution. A cumulative downshift is observed for ν(Fe-O_2) upon addition of the second mutation. This further decrease in frequency for the double mutant can plausibly be explained by a greater disruption of critical nonbonded contacts within the heme pocket that work to stabilize the O_2 complex.

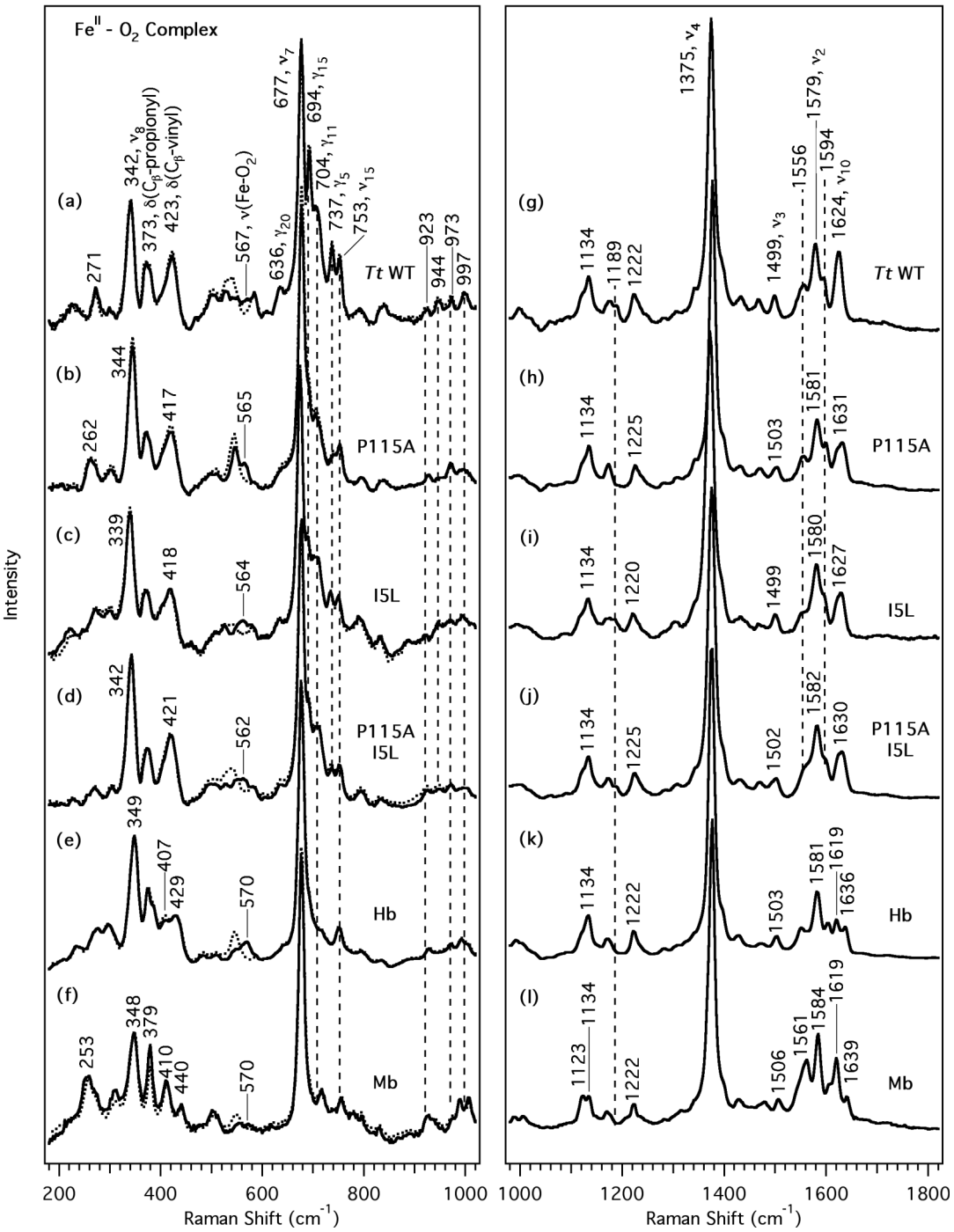

Figure 2.3 Resonance Raman spectra of the O_2 complexes of the *Tt* H-NOX domains and globins. The left panel shows the lower frequency region for *Tt* H-NOX WT (a), P115A (b), I5L (c), P115A/I5L (d), Hb (e), and Mb (f). $^{18}O_2$ spectra (dotted line) are overlapped over the $^{16}O_2$ spectra to indicate the frequency shifts upon isotopic substitution. The right panel shows the high frequency region (traces g-l).

In the high frequency region of the O_2 complexes (Figure 2.3, traces g-l), the skeletal markers at 1375, 1499, 1579, and 1624 cm^{-1} for *Tt* H-NOX WT are indicative of a 6-coordinate, histidyl-ligated, low-spin O_2 complex [101, 102]. Compared to *Tt* H-NOX WT, the three mutants show upshifts of 1-7 cm^{-1} for the skeletal markers (Table 2.2). Similar to the native globins, the *Tt* H-NOX P115A mutant completely lacks a shoulder band at 1189 cm^{-1}, whereas WT and the other mutants exhibit two overlapping bands at 1176 cm^{-1} and 1189 cm^{-1}. In *Tt* H-NOX, ν_3 remains constant at 1499 cm^{-1} for WT and the I5L mutant, but shifts to 1503 and 1502 cm^{-1} for the P115A and I5L/P115A mutants, respectively. The 1556 cm^{-1} peak is most pronounced in *Tt* H-NOX WT and P115A, but appears more as a broad shoulder in the I5L and I5L/P115A mutants. Furthermore, ν_2 (1579 cm^{-1}) and ν_{19} (1594 cm^{-1}) in *Tt* H-NOX WT upshift by 2-3 cm^{-1} and 5 cm^{-1}, respectively, upon mutating Ile-5 and Pro-115; these two bands correspond to C_β-C_β and C_α-C_m stretching vibrations. The breadth and slight asymmetry of ν_{10} (C_α-C_m stretch) in *Tt* H-NOX WT is likely due to overlap with the C=C stretching mode at 1619 cm^{-1} (assignment based on polarization and Q-band RR). Compared to *Tt* H-NOX WT (1624 cm^{-1}), ν_{10} upshifts to 1631, 1627, and 1630 cm^{-1} for the *Tt* H-NOX P115A, I5L, and I5L/P115A mutants. These observed vibrational shifts in the high frequency region is reflective of the approximate shift pattern expected for changes in heme ruffling ($\nu_{10} > \nu_2 > \nu_3 > \nu_4$). However, closer inspection of the high frequency region reveals shoulders for ν_{10} in *Tt* H-NOX P115A and I5L/P115A that correspond to the ν_{10} vibrational frequency for WT at 1624 cm^{-1}. This band broadens and exhibits decreased intensity in the three mutants; the change is most striking in *Tt* H-NOX P115A, which has been shown by crystallography to sample a range of heme conformations [44]. This observed crystallographic heterogeneity in the heme conformation for *Tt* H-NOX P115A is comparable to the broadened ν_{10} in the complementary RR spectra.

Below 1000 cm^{-1}, several vibrational modes in the *Tt* H-NOX O_2 complex spectra display reduced RR intensity upon mutation of Ile-5 and Pro-115. Heme out-of-plane modes (defined as γ to distinguish them from stretching modes, ν) involving bending, tilting, folding, and wagging motions occur in these lower frequency regions [56]. The reduced RR intensities mainly occur in the 675-850 cm^{-1} and 900-1050 cm^{-1} regions as indicated by the vertical dashed lines in Figure 2.3 (traces a-d). Specifically, *Tt* H-NOX WT (trace a) exhibits peaks at 694 (γ_{15}, sym. pyr fold), 704 (γ_{11}, asym. pyr fold), 737 (γ_5, sym. pyr fold), 944 [$\delta(C_m\text{-H})$], and 997 cm^{-1} [$\delta(C_m\text{-H})$] which decrease in relative RR intensity after mutating Ile-5 and Pro-115; the most striking change occurs at 694 cm^{-1}. This band may be attributed to an in-plane pyrrole ring folding deformation mode [65]. Subtle changes are also observed in the overlapping *Tt* H-NOX WT bands in the 500-640 cm^{-1} region, which are likely due to pyrrole swivels and folding vibrations [56, 85, 88]. Of particular note are the weak bands at 526 (ν_{49}), 589 (ν_{48}), 605 (sym. pyr fold) and 636 cm^{-1} (γ_{20}, asym. pyr fold) in *Tt* H-NOX WT that vanish in the *Tt* H-NOX P115A mutant. These peaks are still present in the *Tt* H-NOX I5L and I5L/P115A mutants, albeit slightly broader and lower in intensity than WT. The 271 cm^{-1} band in *Tt* H-NOX WT also broadens and downshifts by 9 cm^{-1} in the P115A mutant to 262 cm^{-1}; this peak may correspond to either ν_{52} (porph-substituent bending) or a pyrrole tilting motion (γ_{16}) within the heme [86, 103].

2.4.3 Spectral decomposition

The RR intensity decreased for several low frequency modes in the O_2 complexes for the *Tt* H-NOX mutants (Figure 2.3), but remained constant in the unligated (Figure 2.2, supporting information, Figure 2.1S) and CO complexes (supporting information, Figure 2.3S). These bands may show changes in intensity due to the inactivation of Raman modes upon heme relaxation. To quantify these spectral changes, the RR spectra were normalized and fit to Lorentzian peaks with fixed widths. The integrated peak areas are shown in Figure 2.4 to compare the RR intensity changes across *Tt* H-NOX WT and mutants. Intensity decreases of ~30-70% are observed in the RR spectra of the O_2 complexes upon mutating Ile-5 and Pro-115. In addition, the 704 cm^{-1} peak (γ_{11}, asym. pyrrole folding) in *Tt* H-NOX WT broadens and develops a small shoulder at 709-712 cm^{-1}, shifting toward the higher frequency band and decreasing in RR intensity in the mutants.

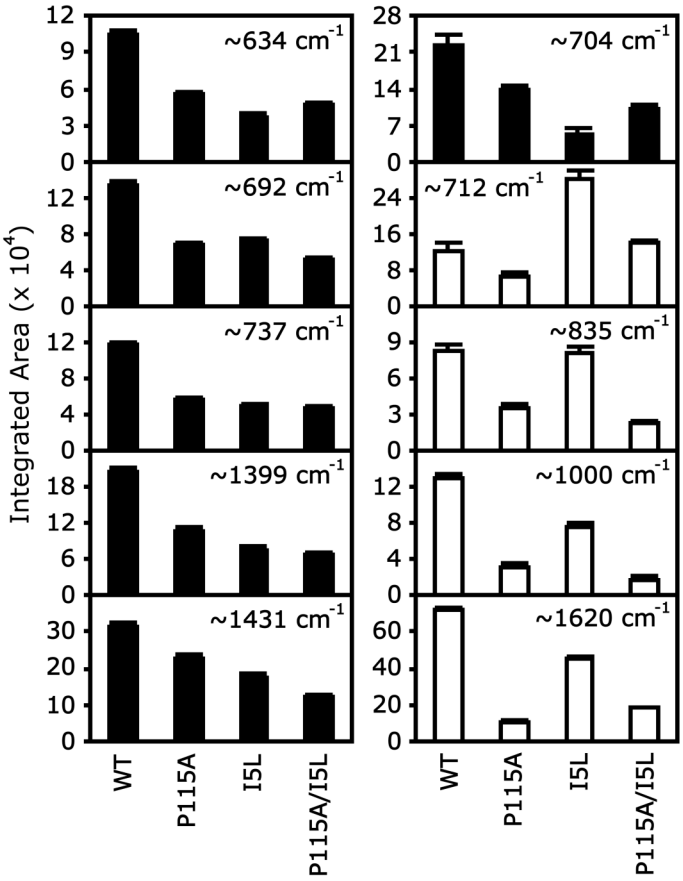

Figure 2.4 Integrated RR peak areas show intensity changes in *Tt* H-NOX O_2 complexes upon mutation of Ile-5 and Pro-115. The black and white bars denote the two different trends in RR intensity changes.

Two different trends in the RR intensities were noted (the bars in Figure 2.4 are shaded differently to denote the two trends): one shows the intensity steadily decreasing across all mutants, whereas the other trend displays a zigzag pattern due to the minimal to moderate intensity change observed in *Tt* H-NOX I5L compared to the other two mutants.

2.4.4 Normal coordinate structural decomposition

Table 2.3 quantifies the calculated heme out-of-plane (oop) distortions for the O_2 complexes of *Tt* H-NOX and other proteins from our NSD analysis [50]. The generated output gives the amount of displacement along the normal coordinates for the six deformation types (*e.g.* ruffling, saddling) that properly simulate the observed distortions in the *Tt* H-NOX heme coordinates. NSD results obtained from other heme proteins are included for comparison. The total out-of-plane displacement (Δ_{oop}) and the amount of specific deformation types are reported according to the complete and minimal basis sets, respectively. The complete basis set includes all normal modes of the 24 atom D_{4h}-symmetric porphyrin macrocycle ($C_{20}N_4$) to fully describe the observed heme nonplanarity. The minimal basis set only includes the lowest frequency normal coordinates of each symmetry type (6 in-plane and 6 out-of-plane) since these are expected to have the lowest distortion energies and should be predominant in the heme deformations [48, 49].

As shown in Table 2.3, the largest displacements observed in the *Tt* H-NOX WT monoclinic (PDB 1U55) and orthorhombic (PDB 1U4H) crystal structures are from the B_{2u} (saddling) and B_{1u} (ruffling) deformations. The total rms out-of-plane displacement (Δ_{oop}) is ~1.6 Å for three different *Tt* H-NOX WT structures, but is reduced to ~1.1 Å in the monoclinic heme B structure. Pellicena *et al*. associate this heme relaxation with a ~11° rotation of the protein's distal portion with respect to the proximal side and a reorientation of the distal Ile-5 residue [5]. With the exception of the monoclinic heme B structure, the other three *Tt* H-NOX WT hemes maintain ~1.0-1.2 Å displacements in B_{1u} and B_{2u} deformations.

Compared to *Tt* H-NOX WT (Δ_{oop} ~1.6 Å), the *Tt* H-NOX I5L mutant showed a decrease of ~0.2-0.3 Å in overall out-of-plane displacement. The B_{1u} deformation is more relaxed than B_{2u} in *Tt* H-NOX I5L, but a small increase occurs in the $E_{g(x,y)}$ (waving) displacement. In addition, the B_{1u} directionality changes sign between the two *Tt* H-NOX I5L heme molecules. This also occurs for several deformations in the truncated and human hemoglobins (PDB 1IDR and 2DN1, respectively), and may result from differences in the crystal packing interactions and orientation of residues close to the heme.

The crystal structure of *Tt* H-NOX P115A contained four different hemes, producing a broader range of NSD displacements compared to the other proteins (PDB 3EEE). The most relaxed structure (heme C) exhibited out-of-plane distortion values (B_{2u}, -0.04

Å; B_{1u}, -0.49 Å; Δ_{oop}, 0.54 Å) comparable to those obtained for the crystal structures of *Bj* FixL [96] and the globins [53, 97, 98]. The Δ_{oop} for these proteins ranged from 0.36 to 0.60 Å in contrast to *Tt* H-NOX WT (~1.6 Å). The total out-of-plane displacement for the least relaxed *Tt* H-NOX P115A structure (heme A) is 0.90 Å, which is close to the 1.11 Å Δ_{oop} observed for the monoclinic *Tt* H-NOX WT heme B structure.

Table 2.3 Calculated heme out-of-plane distortions from normal coordinate structural decomposition (NSD) analysis for O_2-bound *Tt* H-NOX and other heme proteins.

PDB	Protein	Δ_{oop} [a]	B_{2u} [b]	B_{1u}	A_{2u}	$E_{g(x)}$	$E_{g(y)}$	A_{1u}	Ref.
1U55	*Tt* WT A	1.59	-1.07	-1.11	-0.1	-0.10	0.24	-0.03	[5]
1U55	*Tt* WT B	1.11	-0.65	-0.79	0.32	-0.24	0.02	-0.03	[5]
1U4H	*Tt* WT A	1.59	-1.09	-1.09	-0.02	-0.30	0.11	-0.06	[5]
1U4H	*Tt* WT B	1.60	-1.00	-1.20	0.10	-0.15	0.14	-0.06	[5]
Heme A	*Tt* I5L	1.28	-0.93	0.73	-0.11	-0.18	0.40	-0.02	[c]
Heme B	*Tt* I5L	1.23	-0.81	-0.81	0.13	-0.31	0.14	-0.02	[c]
3EEE	*Tt* P115A A	0.90	-0.40	-0.77	0.04	-0.17	0.02	0.00	[44]
3EEE	*Tt* P115A B	0.82	-0.50	-0.61	0.03	-0.11	0.03	0.01	[44]
3EEE	*Tt* P115A C	0.54	-0.04	-0.49	-0.09	-0.16	-0.08	0.01	[44]
3EEE	*Tt* P115A D	0.62	0.07	-0.52	-0.03	-0.25	-0.18	0.01	[44]
Heme A	*Tt* I5L/P115A	0.85	-0.53	0.05	-0.16	-0.05	0.52	-0.04	[c]
Heme B	*Tt* I5L/P115A	0.74	-0.63	0.17	-0.02	0.01	0.32	-0.08	[c]
1DP6	*Bj* FixL [d]	0.60	0.44	-0.32	0.18	0.01	0.11	-0.03	[96]
1A6M	*Sw* Mb [e]	0.36	0.19	0.01	0.22	-0.05	0.19	0.07	[98]
1ASH	As Hb [f]	0.47	-0.11	0.41	0.08	-0.11	0.07	-0.01	[53]
1IDR	tHb A [g]	0.58	-0.13	0.33	0.28	-0.25	-0.19	0.04	[97]
1IDR	tHb B [g]	0.55	0.15	0.45	0.01	0.05	-0.21	-0.04	[97]

[a] Total out-of-plane displacement (Å) from the complete basis set
[b] Reported displacements for each symmetry type are from the minimal basis set
[c] unpublished experiments, Olea *et al.*
[d] O_2-sensing FixL domain of *Bradyrhizobium japonicum*
[e] Sperm whale myoglobin
[f] *Ascaris suum* hemoglobin domain I
[g] Truncated hemoglobin N from *Mycobacterium tuberculosis*

The *Tt* H-NOX double mutant significantly relaxed the ruffling distortion with a B_{1u} displacement of ~0.05-0.2 Å. Comparable to *Sw* Mb, these magnitudes are the lowest

of the three *Tt* H-NOX mutants. In contrast, the B_{2u} displacement (heme A, -0.53 Å; heme B, -0.63 Å) is greater than the < 0.1 Å observed in hemes C and D of the P115A mutant. Another unique feature exhibited by the double mutant is the ~0.3-0.5 Å $E_{g(y)}$ contribution, which is similar to *Tt* H-NOX I5L heme A (0.4 Å). Interestingly, the Δ_{oop} for *Tt* H-NOX I5L/P115A (heme A, 0.85 Å; heme B, 0.74 Å) falls within the ~0.5 - 0.9 Å range obtained for the four *Tt* H-NOX P115A heme molecules, suggesting that the Ile-5 mutation contributes minimally to heme relaxation.

2.5 Discussion

We now provide a detailed interpretation of the spectral changes exhibited by RR leading to the current model for heme distortion in *Tt* H-NOX. Specifically, the reduction in relative RR intensity for the low frequency modes, and the observed frequency shifts and peak broadening in the heme skeletal markers of *Tt* H-NOX P115A and I5L mutants provide evidence for a more relaxed chromophore within the solution form of the mutated protein. These changes are related to the heme structure and how its altered conformation, in comparison to *Tt* H-NOX WT, may result from heme cavity rearrangements. By comparing the spectroscopic data with the available crystallographic results, detailed information on the heme structure and insight into the possible role of these conserved residues are revealed.

2.5.1 RR intensity changes in *Tt* H-NOX O_2 complex spectra

Choi and Spiro identified several out-of-plane motions of iron-porphyrin complexes, including pyrrole tilts (~260 cm^{-1}), methine bridge deformations [$\gamma(C_\alpha\text{-}C_m)$, ~320 cm^{-1}], pyrrole folding modes (~425-510 cm^{-1}), and methine-hydrogen deformations [$\gamma(C_m\text{-}H)$, ~840 cm^{-1}] [65]. Modes that occur below 400 cm^{-1} involve methine bridge wagging and other pyrrole deformations, and are expected to be heavily mixed [56]. These out-of-plane modes are generally expected to be Franck-Condon and Jahn-Teller inactive for planar porphines of D_{4h} symmetry, but may be activated upon nonplanar heme distortion and symmetry reduction [65, 88]. The RR intensities of these modes are induced when their components are projected onto the in-plane electronic excitations [65, 86]. Hence, only the modes that occur along specific heme distortion coordinates and have the same symmetry will be activated.

Our RR spectra of *Tt* H-NOX WT exhibit several bands corresponding to out-of-plane modes associated with heme deformations in the O_2 complex. Specifically, the 450-600 cm^{-1} region displays many overlapped Raman features that are plausibly out-of-plane pyrrole tilts, swivels, and folding modes activated by the symmetry lowering effects of the protein environment on the chromophore. Other notable features include the moderately intense 692 cm^{-1} shoulder (γ_{15}, sym. pyrrole folding), the 704 peak with

a small shoulder at 712 cm^{-1} (γ_{11}, sym. pyrrole folding), and the 737 cm^{-1} band (γ_5/ν_{16}, asym. pyrrole folding and deformation). These peaks are known to be sensitive to saddling (B_{2u}) and ruffling (B_{1u}) deformations, and are tentatively assigned by association with previous work by Spiro, Shelnutt, Schweitzer-Stenner, and others [56, 65, 70, 85, 86, 88, 92, 104]. Between 900-1000 cm^{-1}, four distinct peaks observed in the *Tt* H-NOX WT spectrum are tentatively assigned as hydrogen wagging motions [103]. These RR features confirm that the striking heme deformations observed in the *Tt* H-NOX WT structure also exist in solution and are not an outcome of crystallization. Interestingly, these characteristic low frequency bands in the *Tt* H-NOX spectra are unique to the O_2 complex, and are not prominently featured in the other *Tt* H-NOX complexes or bacterial H-NOXs (*e.g. V. cholerae*, *L. pneumophila*, *N. punctiforme*) [1, 52]. In agreement with these observations, NSD analysis of the *N. sp* H-NOX domain crystal structures by Ma *et al.* indicate $\Delta_{oop} \sim 0.7$-0.9 Å for the unligated, CO, and NO complexes; these values are lower than those observed for the *Tt* H-NOX O_2 structures by Pellicena *et al*. ($\Delta_{oop} \sim 1.1$-1.6 Å) [5, 43].

Mutation of the Ile-5 and Pro-115 residues in *Tt* H-NOX caused decreases in the relative RR intensities for several out-of-plane modes in the O_2 complex, but did not appreciably alter any mode intensities in the unligated spectra. These observations indicate a distinct difference in how the mutations affect the heme conformation for the O_2 and unligated species; although significant structural changes occur in the O_2 complex, the great similarity in RR intensity for the unligated spectra strongly suggests minimal changes in the heme structure. The most important point about the loss of RR intensity is that it clearly demonstrates a relaxation of the heme upon mutating these residues. The replacement of Pro-115 in *Tt* H-NOX with an alanine relieves the original proximal strain on pyrrole group D by freeing up space around the random coil linking α-helix F and β-strand 1. This structural reorganization is consistent with the loss of RR intensity at 508 (γ_{12}), 526 (ν_{49}), 588 (ν_{48}), and the 692-737 cm^{-1} region (γ_{15}, γ_{11}, γ_5), where pyrrole swivels and folding modes that correspond to the B_{1u}, B_{2u}, and E_g symmetry are expected to occur [70, 85, 86, 88, 104]. A similar effect, albeit to a lesser degree, can explain the changes in the *Tt* H-NOX I5L spectra via its distal strain over pyrrole A and influence on reorienting nearby residue contacts with the propionate groups (*e.g.* Asp-45).

Although the three *Tt* H-NOX mutants showed comparable decreases in relative RR intensity for some of the low frequency bands, the P115A mutant displayed several distinct features. These included the following observations: (i) the apparent absence of the 1189 cm^{-1} peak corresponding to the C_β-substituent and C_α-N antisymmetric stretching modes, which is also exhibited in the globins spectra, (ii) the retention of the hydrogen wagging modes (850-1050 cm^{-1}) in *Tt* H-NOX I5L compared to the P115A mutant, and (iii) the greater similarity in peakwidth and frequency between the *Tt* H-NOX I5L and WT spectra in comparison to P115A. In addition, the locations where RR intensity is lost after mutating the heme pocket residues correspond well to the less congested regions in the globin spectra, supporting our tentative assignment of these peaks to heme out-of-plane modes. These characteristics together support a more dominant effect of Pro-115 on the *Tt* H-NOX heme structure than Ile-5.

Our spectral observations also fit well with the structural data via the NSD analysis, which indicates that the lowest Δ_{oop} occurs in *Tt* H-NOX P115A (heme C; Δ_{oop} ~ 0.5 Å) rather than the double mutant. The Δ_{oop} range of ~0.5-0.9 Å for all four molecules in the unit cell and the differing effects on the B_{2u} and B_{1u} deformations further support the heme flexibility that we observed by RR in the *Tt* H-NOX P115A mutant. According to the NSD analysis, the *Tt* H-NOX I5L mutation affected the B_{2u} displacement less than B_{1u}; this effect may explain the two trends shown in the spectral decomposition in that some modes may be more sensitive and specific to certain heme deformations. In addition, the normal mode displacements for *Tt* H-NOX I5L displayed modest decreases compared to *Tt* H-NOX P115A, which agrees well with our conclusions from the RR spectra. Finally, the cumulative decrease in relative RR intensity exhibited by the double mutant was close to those observed for the single *Tt* H-NOX P115A mutant, further suggesting that the dominant perturbation of the pocket originates from the Pro-115 mutation. This reduction of the B_{2u} and B_{1u} deformations can be rationalized based on the nonbonded contacts between Pro-115 and pyrrole group C of the heme (Figures 2.1 and 2.5).

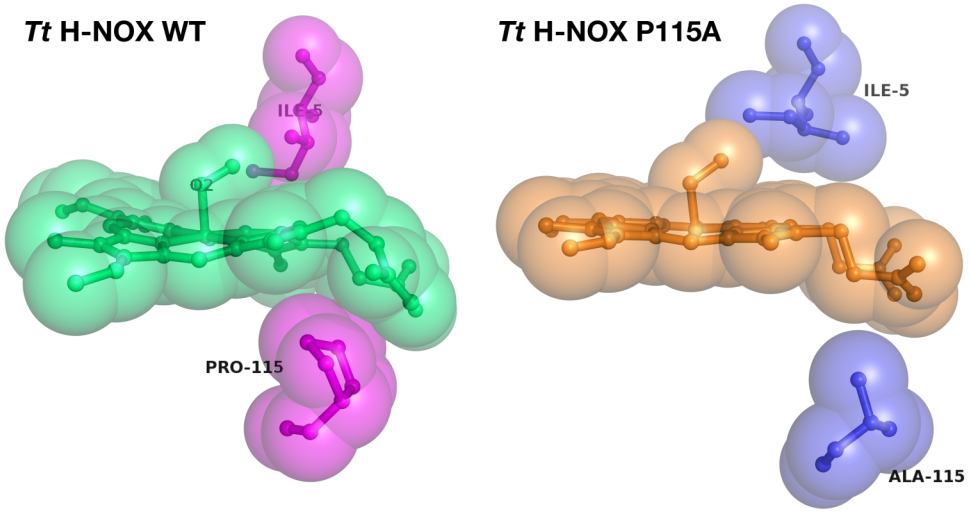

Figure 2.5 Comparison of *Tt* H-NOX WT (PDB 1U55) with P115A (PDB 3EEE) showing reduction of steric nonbonded contacts between proximal Pro-115 and heme upon mutation to Ala-115.

The proline ring clearly pushes up into the heme and forces the chromophore into a nonplanar conformation. Upon substitution with alanine, the ring is substituted by a more freely rotating methyl group, which allows the heme conformation to relax (Figure 2.5). In contrast to Pro-115, Ile-5 makes a less intrusive distal contact with the heme pyrrole group B in *Tt* H-NOX; thus, mutating this residue has a smaller effect on the heme conformation.

2.5.2 Frequency shifts and peak broadening

In contrast to the pronounced changes observed in the O_2 complex spectra, the great similarity in vibrational frequency and intensity between the RR spectra for the *Tt* H-NOX WT and P115A unligated species demonstrates the minimal impact of this mutation on the heme. The increased Fe-His stretching frequency for *Tt* H-NOX P115A suggests a strengthening of the Fe-His bond. In contrast, crystallographic results indicate that the bond lengths for the two proteins are within error. This discrepancy is not surprising since in resonance Raman spectroscopy, a vibrational frequency shift of 5-6 cm^{-1} in the most sensitive bands corresponds to bond length changes of as small as 0.01 Å [56, 63]. Such a change would be below the range detectable by crystallography. Olea *et al*. do note, however, that the Fe-His bond tilting angle shifts from 78° in *Tt* H-NOX WT (heme A, monoclinic) to 87° in P115A (heme C, monoclinic), resulting in a more perpendicular orientation of His-102 with respect to the heme, and plausibly enables a better bond overlap between Fe and His-102 [44]. Furthermore, the slight broadening of the peak by ~5 cm^{-1} suggests some heterogeneity in the proximal pocket, and supports our assertion that the *Tt* H-NOX P115A mutation introduces structural disorder and flexibility to the protein pocket. This heterogeneity in the RR spectra fits well with the 80-87º Fe-His tilt angle range reported for the four *Tt* H-NOX P115A heme molecules [44].

Kinetic studies by Olea *et al*. on *Tt* H-NOX have shown that the O_2 dissociation rates decrease by an order of magnitude between WT ($1.22 \pm 0.09\ s^{-1}$) and the P115A mutant ($0.22 \pm 0.01\ s^{-1}$), but that the O_2 association rates are similar ($13.6 \pm 1.0\ \mu M^{-1}s^{-1}$ and $10.4 \pm 1.1\ \mu M^{-1}s^{-1}$, respectively) [44]. Our RR results exhibit a small cumulative downshift in the $\nu(Fe\text{-}O_2)$ frequency with the three *Tt* H-NOX mutants from 567-570 cm^{-1} (WT) to 562 cm^{-1} (I5L/P115A mutant). In addition, the P115A mutant exhibits a 6 cm^{-1} downshift to 265 cm^{-1} from WT (271 cm^{-1}); this band may be a combination of in-plane $Fe\text{-}N_{pyr}$ stretching, pyrrole tilting, and pyrrole-substituent bending motions (ν_{52}). Irwin *et al*. previously proposed that a stronger ligand field could arise from a constrained heme along the equatorial porphyrin plane [71]. Since heme ruffling is thought to result in a shortening of the equatorial $Fe\text{-}N_{pyr}$ bonds, this may partly explain the different frequencies observed between *Tt* H-NOX WT and the mutants for $\nu(Fe\text{-}O_2)$ and $\nu(Fe\text{-}N_{pyr})$, although other factors within the protein pocket (*e.g.* hydrogen-bonding residues, tension on the trans-Fe-imidazole bond, and steric bulk) also clearly influence the stability of the O_2 complex. In particular, the ruffling deformation/$Fe\text{-}N_{pyr}$ bond distance dependence is consistent with our observed $\nu(Fe\text{-}N_{pyr})$ downshift for the *Tt* H-NOX P115A mutant, which also exhibits a relaxation of the ruffling deformation. In contrast, the crystal structures indicate that the $Fe\text{-}N_{pyr}$ distances are ~2.0 Å for both *Tt* H-NOX WT and P115A with only a negligible decrease for the WT $Fe\text{-}N_{pyr}$ distance. However, based on Badger's Rule [105, 106], the inverse force constant/bond length relationship shows that the vibrational frequency is more sensitive to small changes (~0.01 Å) in internuclear distance. Thus, the discrepancy between the RR spectra and crystal structure can be readily explained.

Structural heterogeneity in a sample can be revealed by the broadness and asymmetry of structure sensitive lines, such as ν_2 (C_β-C_β stretch) and ν_{10} (C_α-C_m stretch) [92]. Our RR results exhibit several regions in which the peaks broaden upon mutating Ile-5 and Pro-115 in *Tt* H-NOX. The clearest example of this is ν_{10} in the P115A mutant; in comparison to the WT spectra, this band decreases in intensity and broadens to display a prominent shoulder band at 1631 cm^{-1}. Broad features are also observed for the *Tt* H-NOX Ile-5 and double mutants in the 1550-1600 cm^{-1} range; the modes in this region correspond to the C_α-C_m, C_β-C_β, and peripheral vinyl modes. The broadening of these distinct peaks into merged bands suggests conformational flexibility in these regions, and may result from the ability of the Leu-5 side chain to rapidly flip directions within the pocket. These fluctuations likely disrupt the contacts between the protein's YxSxR motif and the nearby propionate groups. Furthermore, the fact that ν_2 and ν_{10} upshift in frequency for all three *Tt* H-NOX mutants supports the possibility of a better π-π overlap in the C=C, C_β-C_β, and C_α-C_m bonds within the porphyrin macrocycle as a result of heme relaxation.

Some peak broadening and shoulder band formation also occur below 450 cm^{-1}, where pyrrole deformations are expected to occur. The 423 cm^{-1} peak [$\delta(C_\beta$-vinyl)] in *Tt* H-NOX WT not only downshifts to 417 cm^{-1} (P115A), but also broadens with a weak shoulder band and slight decrease in RR intensity. Several other bands in this region exhibit similar changes. These observations further support the possibility that the *Tt* H-NOX protein pocket no longer firmly holds the heme in a particular conformation.

2.5.3 Possible role for conserved residues in *Tt* H-NOX

The heme deformation in the H-NOX family plausibly plays a role in signal transduction from the chromophore to the protein upon ligand binding; alteration of the heme conformation may induce protein conformational changes, which then regulate the linked signaling protein (*e.g.* histidine kinases, diguanylate cyclases, and MCP domains). Based on our data, we conclude that the single P115A mutation is sufficient to open the *Tt* H-NOX distal pocket and introduce flexibility to the heme structure, enabling the chromophore to relax and sample other conformations. The possibility of the H-NOX domain alternating between closed and open conformations is reasonable based on previously observed varying rotational angles in the H-NOX distal and proximal subdomains [5, 43, 44]. Similar to the protein conformation changes observed by Pellicena *et al*. [5] in the *Tt* H-NOX WT monoclinic structure (heme B), a plausible explanation for P115A's spectral changes is that the distal pocket has more rotational motion, and may sample an open heme pocket more frequently due to the increased flexibility granted by replacing the rigidly kinked proline ring with the more freely rotating alanine methyl group. Thus, the highly conserved Pro-115 and neighboring residues can serve as a hinge point between the N- and C-terminal subdomains, which are necessary for maintaining an enclosed environment, retaining important heme-protein interactions, and conserving specific biochemical properties within the H-NOX protein pocket. A clear example of this is the dramatic changes observed in the

reduction potential and O_2 affinity upon decreasing the amount of heme distortion present in *Tt* H-NOX [44]. The *Tt* H-NOX I5L mutation may also contribute toward opening the pocket, although to a lesser extent based on the more modest spectral changes and shifts exhibited by this single mutant in comparison to those observed by mutating Pro-115. This result is not surprising since the substitution of Ile with Leu is relatively conservative in comparison to the replacement of the proline with alanine. However, this Leu-5 side chain can also plausibly flip inward toward the distal pocket or away from it; thus, the heme may interact differently with the conserved YxSxR motif, depending on whether or not the chromophore is pinned down along pyrrole group A by the aliphatic chain.

In summary, we provide spectral evidence of heme relaxation in the O_2-bound form of *Tt* H-NOX upon mutating the Ile-5 and Pro-115 residues. Our resonance Raman results exhibit the most significant changes in the *Tt* H-NOX P115A mutant, in contrast to the I5L mutation, which bears spectral features more similar to *Tt* H-NOX WT. Furthermore, the double mutant appears to behave more like an admixture of P115A with I5L, rather than a synergistic combination of the two mutations. In addition, we observe some broad shoulder features in the high frequency region that suggest the presence of other heme conformations in the three *Tt* H-NOX mutants. Of the different heme complex forms that we have studied with resonance Raman, the most striking changes occur in the O_2-bound spectra; we see very little change in the unligated and CO complexes. These results provide a clear insight into the actual heme conformation of *Tt* H-NOX P115A in solution; indicating that although it is heterogeneous, the predominant form is significantly relaxed based on both changes in vibrational frequencies and RR out-of-plane mode intensities.

2.6 Acknowledgements

We thank Charles Olea Jr. for providing the structures of *Tt* H-NOX I5L and I5L/P115A, and members of the Mathies and Marletta labs for helpful discussions. We are also grateful to Drs. Kathleen Durkin and Jamin Krinsky at the Molecular Graphics and Computation Facility for their extensive help with MD simulations and DFT calculations.

2.7 Supporting information

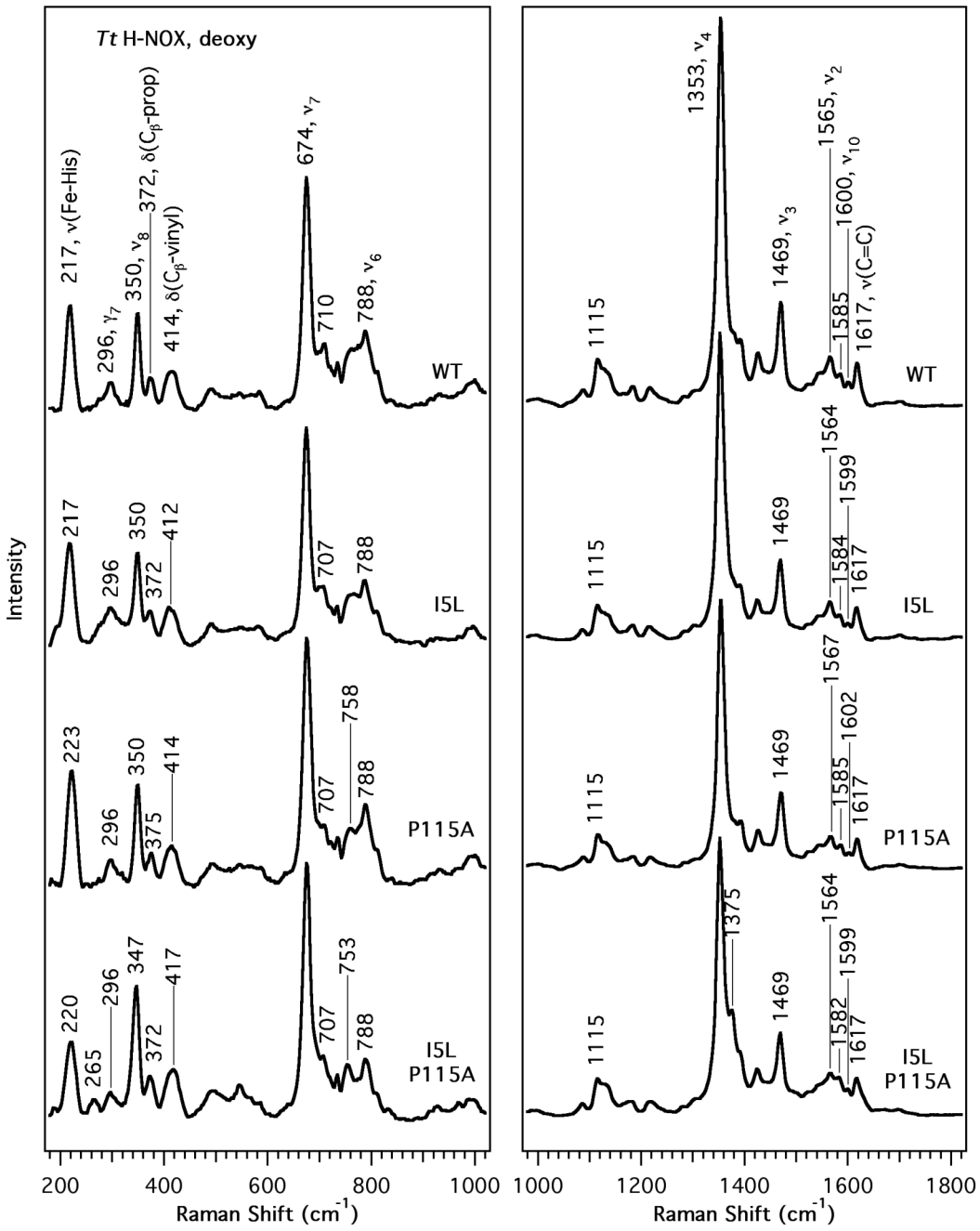

Figure 2.1S Resonance Raman spectra of the Fe^{II}-unligated form of *Tt* H-NOX WT, I5L, P115A, and I5L/P115A. Spectral intensities in the low and high frequency regions were normalized to ν_7 and ν_4, respectively.

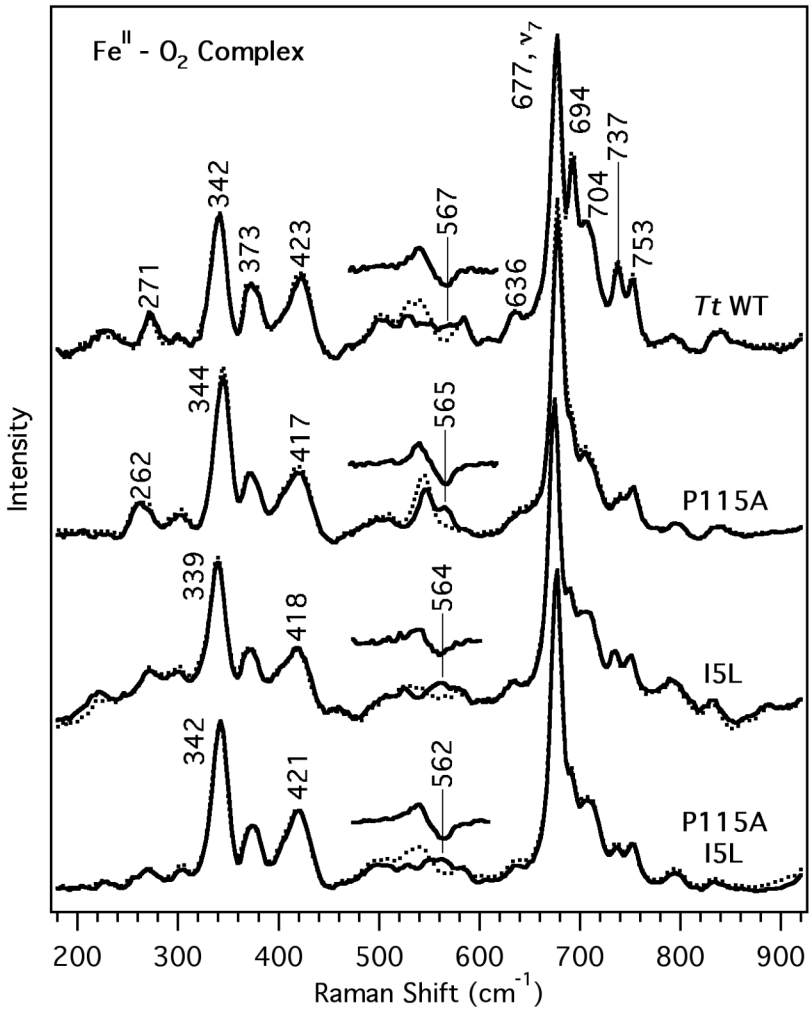

Figure 2.2S Resonance Raman spectra of the O_2 complexes of *Tt* H-NOX WT, I5L, P115A, and I5L/P115A in the low frequency region. $^{18}O_2$ spectra (dotted line) are overlapped over the $^{16}O_2$ spectra to indicate the frequency shifts upon isotopic substitution, and the difference ($^{18}O_2$-$^{16}O_2$) spectra are shown above each protein for clarity in the ν(Fe-O_2) assignment. Spectral intensities were normalized to ν_7.

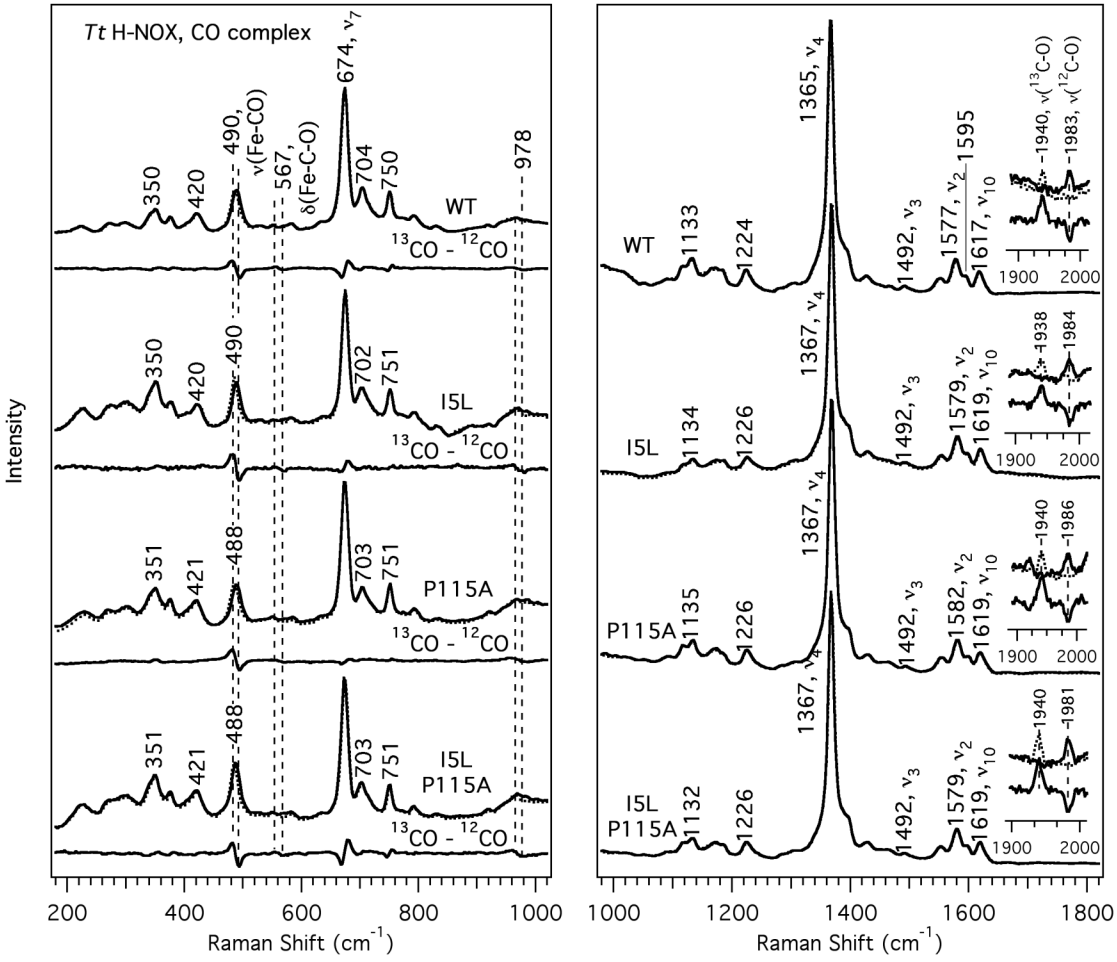

Figure 2.3S Resonance Raman spectra of the CO complexes of *Tt* H-NOX WT, I5L, P115A, and I5L/P115A. ^{13}CO spectra (dotted line) are overlapped over the ^{12}CO spectra to indicate the frequency shifts upon isotopic substitution, and the difference (^{13}CO-^{12}CO) spectra are shown below each protein for clarity. Spectral intensities were normalized to ν_7 and ν_4 for the low and high frequency regions, respectively.

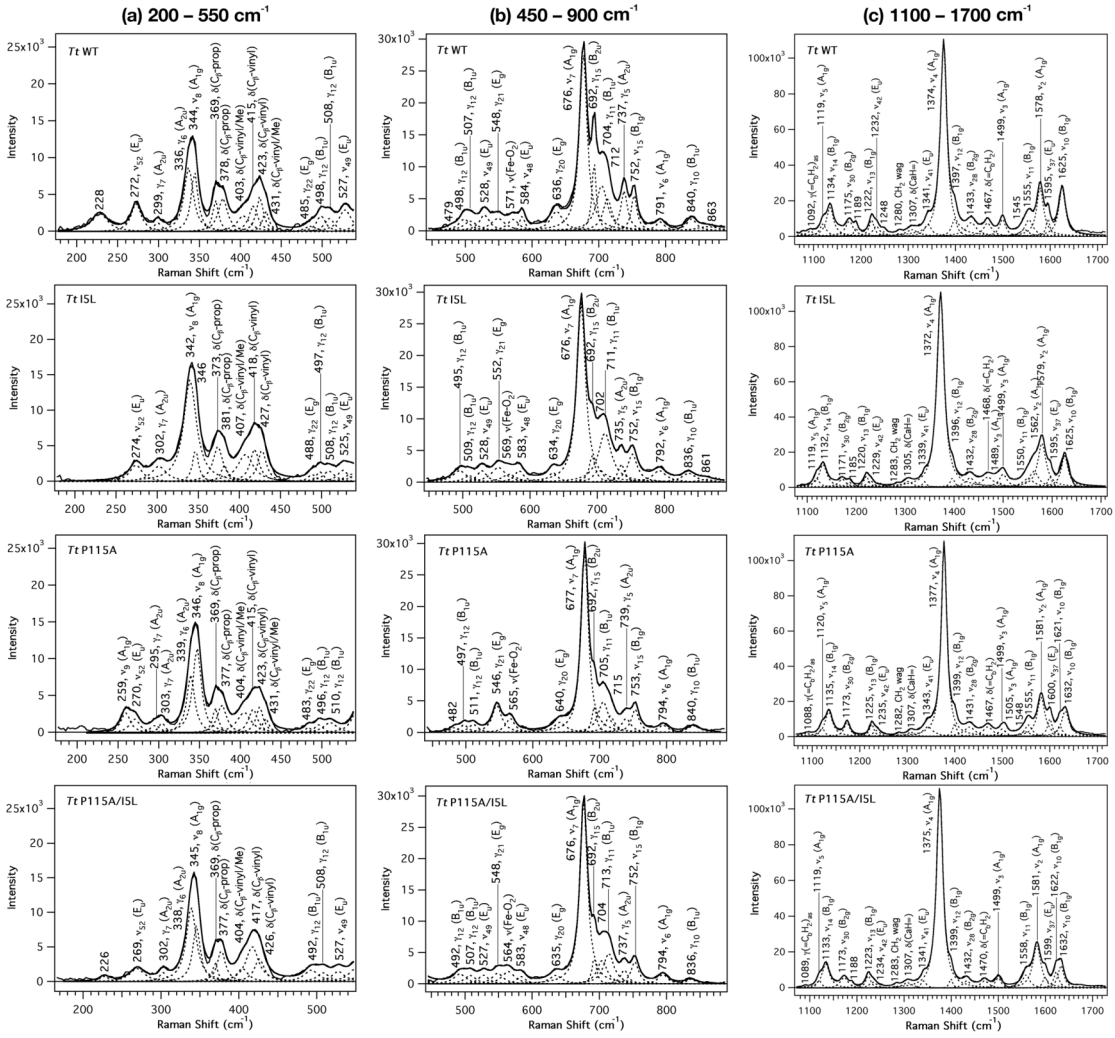

Figure 2.4S Spectral decomposition of resonance Raman spectra for *Tt* H-NOX WT, I5L, P115A, and I5L/P115A in different frequency regions: (a) 200 – 550 cm^{-1}, (b) 450 – 900 cm^{-1}, (c) 1100 – 1700 cm^{-1}.

Chapter 3

Resonance Raman Analysis of the Heme-CO Modes in the H-NOX Family

3.1 Abstract

A unique vibrational feature that is ubiquitous throughout the *H*eme-*N*itric oxide/*OX*ygen binding (H-NOX) family is the presence of a high C-O stretching frequency. The structural determinants of the Fe-CO and C-O stretching frequencies in the H-NOX family were investigated via resonance Raman (RR) spectroscopy to elucidate the protein-ligand interactions responsible for this observation. Mutations made in the distal pocket of the H-NOX domain from *Thermoanaerobacter tengcongensis* (*Tt* H-NOX), as well as the conserved Tyr-Ser-Arg (YxSxR) motif, indicate that important electrostatic interactions occur which can significantly affect the CO bond by modulating the back-donation of the Fe^{II} d_π electrons into the CO π^* orbitals. Multiple CO conformers were revealed upon mutation of the Tyr-140 H-bonding residue, and ν(C-O) exhibited downshifts of up to ~60 cm^{-1}. The most significant change occurred from the disruption of the H-bonds between the YxSxR motif and the heme propionate groups, which produced two dominant CO-bound heme conformations; one was structurally similar to *Tt* H-NOX WT, and the other conformer displayed ν(C-O) downshifts of up to ~70 cm^{-1} with minimal changes in ν(Fe-CO). The influence of the Fe-His bond strength was also examined by substituting several heterocyclic ligands into the proximal cavity of *Tt* H-NOX H102G, thereby shifting the competition for metal σ bonding between the bound CO and the *trans* ligand. Interestingly, these mutants downshifted ν(C-O) by ~30 cm^{-1} and upshifted ν(Fe-CO) by ~40 cm^{-1}. In contrast, mutations on the Ile-5 and Pro-115 residues, which are predicted to influence heme deformations, had little effect on the Fe-CO or C-O stretching modes. Altogether, these RR results show that the electrostatic interactions occurring in the heme pocket of *Tt* H-NOX are primarily responsible for the unusually high ν(C-O) by dampening the Fe $d_\pi \rightarrow$ CO π^* back-donation. In addition, our results indicate that the mechanism by which the protein modulates the Fe^{II}-CO bond predominantly involves the strictly conserved YxSxR motif.

3.2 Introduction

The family of prokaryotic and eukaryotic proteins known as the *H*eme-*N*itric oxide/*OX*ygen binding (H-NOX) domains, which includes the heme domain from the mammalian NO receptor soluble guanylate cyclase (sGC), has the distinctive property in that some members bind only NO and CO, whereas others can also bind O_2 [1, 5, 47]. A unique feature that is shared by all of these H-NOX domains is an unusually high C-O stretching frequency observed in the heme-CO adducts. Despite the availability of NMR and x-ray crystal structures for several of these H-NOX domains [5, 42-44, 46], the factors that are responsible for the high ν(C-O) are unclear.

Due to its selectivity and sensitivity to molecular structure, the use of resonance Raman (RR) spectroscopy with heme-CO adducts is well established as a powerful tool in understanding heme protein-ligand interactions in solution. The nature of these interactions can be elucidated from the Fe-CO and C-O stretching frequencies, especially since these modes are highly sensitive to the electrostatic field of the distal pocket and the donor properties of the proximal ligand. Extensive density functional theory (DFT) computations and vibrational studies on both heme proteins and synthetic model porphyrins have previously shown that the Fe-CO and C-O vibrational frequencies are negatively correlated due to backbonding effects; the Fe^{II} d_π electrons are back-donated to the CO π^* orbitals, strengthening the Fe-CO bond while weakening the C-O bond [72, 75, 76, 80, 83, 84, 91, 107-117]. Thus, a key focus in investigating these H-NOX proteins via RR spectroscopy is to better understand the interactions between the exogenous diatomic ligands and the H-NOX heme binding pocket in solution. A more complete knowledge of the complex protein-ligand interactions will not only reveal how the C-O stretching frequency is modulated in these heme domains, but may also help determine key components that are responsible for controlling ligand specificity in the H-NOX family.

Aside from the unusually high ν(C-O) frequency in the H-NOX family, CO is also an interesting ligand to study due to its ability to weakly catalyze the conversion of GTP to cGMP upon binding to the heme prosthetic group of sGC [35]. Although the 2-4-fold increase in cGMP production upon CO binding is significantly lower than the 100-400-fold increase upon NO binding to sGC, the enzyme activity can be modulated by small molecules such as the benzylindazole derivative, YC-1 [3-(5'-hydroxymethyl-3'-furyl)-1-benzylindazole]. RR investigations have shown changes in the heme conformation upon introduction of these small molecules, suggesting that they interact with the heme prosthetic group [36, 37, 68, 73]. Furthermore, previous work found that truncation of full length sGC to its heme domain, β1(1-194), resulted in a ~20 cm^{-1} ν(C-O) downshift to ~1968 cm^{-1} [34, 67, 77, 118]. These results suggest that the protein structure and conformational flexibility also influences the CO stretching frequency.

In this study, RR spectroscopy is used in conjunction with site-directed mutagenesis and isotopic substitution to evaluate different features within the H-NOX domain from *Thermoanaerobacter tengcongensis* (*Tt* H-NOX), and determine their ability to

modulate the C-O stretching frequency. *Tt* H-NOX is an ideal protein for use as a model to systematically alter these binding site properties through site-directed mutagenesis because it is a stable protein, expresses very well, and several crystal structures are available. The specific heme pocket components investigated in this work include: (i) the presence of H-bonding distal residues, (ii) strength and steric constraints of the proximal ligand, (iii) H-bonding between the conserved Tyr-Ser-Arg (YxSxR) motif and the propionate substituents of the heme, and (iv) heme deformation (Figure 3.1). Our RR spectra provide significant insight into these interactions in solution, and their influence on the Fe-CO bond in *Tt* H-NOX.

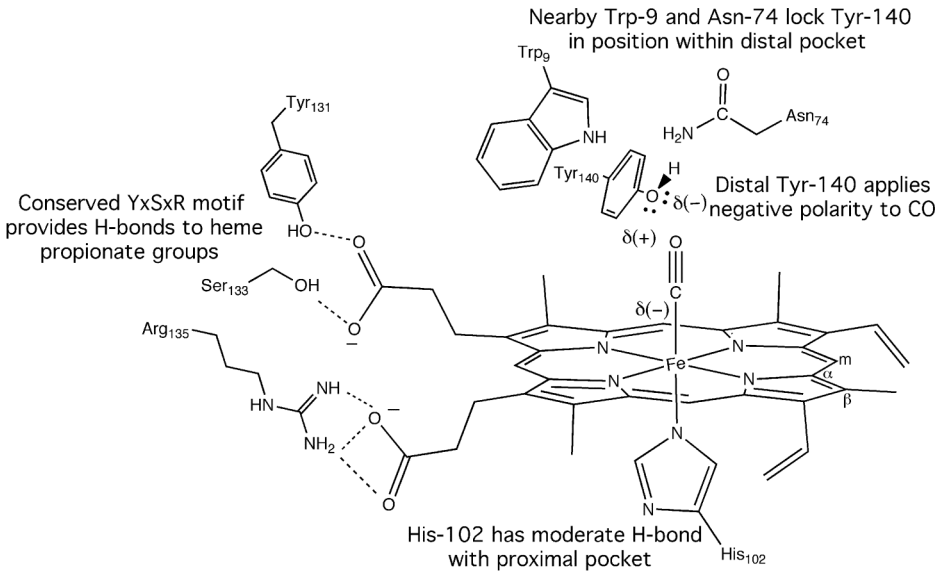

Figure 3.1 Schematic representation of the heme pocket of *Tt* H-NOX. The different components of the *Tt* H-NOX binding site that can influence the Fe^{II} $d_\pi \rightarrow$ CO π^* backdonation are shown in this diagram: (i) the H-bonding network composed of Trp-9, Asn-74, and Tyr-140 affects the polarity of the distal pocket where CO is bound, (ii) modulation of the axial *trans* ligand strength can influence how the proximal ligand competes with CO for σ-orbital overlap with Fe, and (iii) H-bonding interactions between the conserved YxSxR motif and heme propionate groups can withdraw electron density from the heme.

3.3 Materials and Methods

3.3.1 Protein expression and purification.

Expression and purification of the his-tagged (-H_6) *Tt* H-NOX domain were performed as previously described for the original construct [1, 45]. Site-directed mutagenesis was carried out using the QuikChange® protocol (Stratagene), and verified by sequencing (UC Berkeley sequencing core).

The *Tt* H-NOX H102G mutant was expressed and purified with imidazole as the proximal ligand using the same methods described for the WT protein, with the following modifications. Imidazole (Im) (10 mM) was added to the expression cultures at the time of induction with IPTG. In addition, 10 mM imidazole was added to buffer A during purification to ensure retention of the heme in the protein.

3.3.2 Sample preparation

Purified *Tt* H-NOX-H_6 protein was brought into an anaerobic glovebag, and oxidized using ~5-10 mM potassium ferricyanide to remove the bound O_2. The ferricyanide was removed using a PD10 desalting column (Amersham Biosciences) equilibrated with buffer B (50 mM TEA, 50 mM NaCl, pH 7.5). Following oxidation and desalting, the protein was reduced with ~5-20 mM sodium dithionite that was removed using a PD10 desalting column upon complete reduction of the heme. To make the ^{12}CO (Praxair) and ^{13}CO (^{13}C, 99%; ^{18}O, < 2%; Cambridge Isotopes) complexes, gas was added to a sealed Reacti-Vial (Pierce) containing Fe^{II}-unligated protein. Final sample concentrations for the Raman experiments were typically 15 to 30 μM for the ferrous unligated proteins, and between 35 to 75 μM for the CO complexes. All UV/Vis absorption samples were prepared and measured as previously described [1, 52].

Other exogenous proximal ligands were substituted into the *Tt* H-NOX H102G mutant in addition to imidazole (Im); these included 1-methyl-imidazole (1-Me-Im), 2-methyl-imidazole (2-Me-Im), 4-methyl-imidazole (4-Me-Im), 4-bromo-imidazole (4-Br-Im), 4-iodo-imidazole (4-I-Im), pyridine (Pyr), and 3-fluoro-pyridine (3-F-Pyr). To exchange the proximal ligands, the purified *Tt* H-NOX H102G(Im) protein was heated for 1 h at 50 °C with ~5-10 mM potassium ferricyanide, then desalted with a PD10 column equilibrated with buffer B containing 10 mM of the appropriate proximal ligand. The desalted protein was then heated at 50 °C for an additional 30 min, and reduced with ~5-20 mM sodium dithionite that was removed using a PD10 desalting column upon complete reduction of the heme. This method was sufficient to exchange the imidazole with the alternate proximal ligands. Once the proximal ligand was substituted, generation of the ferrous unligated and CO-bound forms were performed as described above.

3.3.3 Resonance Raman spectroscopy

All spectra were collected using the 413.1 nm line from a Kr^+ laser (Spectra-Physics model 2025) focused to a beam diameter of ~60 μm with a 50 mm focal-length excitation lens. Raman scattering was detected with a cooled, back-illuminated CCD (LN/CCD-1100/PB; Roper Scientific) controlled by an ST-133 controller coupled to a subtractive dispersion double spectrograph [95]. The protein samples were

anaerobically loaded into a microspinning Raman sample cell in a glove bag to avoid the possibility of O_2-binding. The power at the sample was 2 mW, except for the CO complexes, where the laser power was reduced to ~250 μW to minimize CO photolysis. Typical data acquisition times were 60 to 90 minutes. Electronic absorption spectra were obtained before and after the Raman experiments to verify that no photoinduced degradation occurred. Raman spectra were corrected for wavelength dependence of the spectrometer efficiency with a white lamp, and the instrument was calibrated using the Raman frequencies from cyclohexane, CCl_4, and toluene. The reported frequencies are accurate to ±1 cm^{-1}, and the spectral bandpass was set to 8 cm^{-1}. For each Raman spectrum, the raw data were baseline-corrected, and the buffer background signal was subtracted. Spectral analysis was performed using Igor Pro (WaveMetrics). Isotopic shifts were approximated on the basis of a simple harmonic oscillator model.

3.4 Results

3.4.1 Electronic absorption characterization

Tables 3.1 and 3.2 show the Soret and α/β bands measured at room temperature for *Tt* H-NOX and the mutants in the ferrous unligated and CO-bound forms, respectively. As noted by Karow *et al*. [1], *Tt* H-NOX WT is 5-coordinate and high spin when ferrous and unligated, with a Soret maximum at 430 nm and a single broad peak at 563 nm in the α/β region. With one exception, the other mutants displayed electronic absorption properties very similar to those observed in the WT protein. In contrast, the *Tt* H-NOX H102G mutant exhibited downshifts of between 5 to 8 nm in the Soret band for the fully reduced, 5-coordinate ferrous unligated form. Similar changes are observed in the α/β band region for these proteins, as shown in Table 3.1.

Upon addition of CO to the anaerobically reduced proteins, the spectra display changes reflective of 6-coordinate, low spin CO-bound complexes. The Soret shifts to lower wavelengths and sharpens at ~423 nm, and the α/β band splits to two peaks at ~567 nm and ~541 nm. As is the case for the fully reduced protein, all the CO-bound mutants summarized in Table 3.2 displayed similar changes in their electronic absorption properties upon binding CO except for the *Tt* H-NOX H102G protein. In comparison to the WT protein, the H102G mutants with imidazolate derivatives show Soret blue shifts of up to 12 nm from the typical ~423-424 nm position. In contrast, the H102G mutants with imidazole, pyridine, and 3-F-pyridine as proximal ligands only display 1-4 nm decreases in wavelength relative to WT.

In summary, there are relatively small spectral shifts observed in these *Tt* H-NOX proteins in comparison to WT. These minor changes may be due to structural rearrangements within the protein pocket upon mutation. The *Tt* H-NOX H102G mutant exhibits the most interesting properties with downshifts to shorter wavelengths at the Soret and α/β regions for both the ferrous unligated and CO-bound forms.

Table 3.1 Electronic absorption properties for *Tt* H-NOX WT and mutants in the 5-coordinate, Fe^{II}-unligated form.[a]

Protein	Ligand	Soret	α/β	Ref.
Tt WT	reduced	430	563	[1]
Tt W9F		430	562	[38]
Tt H102G (Im)[b]		431	561	this work
Tt H102G (1-Me-Im)[b]		428	565	this work
Tt H102G (2-Me-Im)[b]		424	574/545	this work
Tt H102G (4-Me-Im)[b]		425	573/549	this work
Tt H102G (4-Br-Im)[b]		423	574/545	this work
Tt H102G (4-I-Im)[b]		423	575/544	this work
Tt H102G (Pyr)[b]		425	571	this work
Tt H102G (3F-Pyr)[b]		423	574/545	this work
Tt Y131F		430	561	this work
Tt S133A		430	563	this work
Tt S133C		430	561	this work
Tt R135Q		431	563	this work
Tt Y140H		430	563	this work
Tt Y140F		429	566	[38]
Tt P115A/Y140F		430	565	this work
Tt Y140L		429	570	[38]
Tt I5L		431	569	[51]
Tt P115A		432	563	[51]
Tt I5L/P115A		431	566	[51]

[a] All peak positions are reported in nm.
[b] All proximal ligand concentrations were set at 1 mM.

Table 3.2 Electronic absorption properties for *Tt* H-NOX WT and mutants in the 6-coordinate, Fe^{II}-CO complex form.[a]

Protein	Ligand	Soret	α/β	Ref.
Tt WT	CO	423	567/541	[1]
Tt W9F		423	562/541	this work
Tt H102G (Im) [b]		424	571/545	this work
Tt H102G (1-Me-Im) [b]		423	568/545	this work
Tt H102G (2-Me-Im) [b]		412	570/537	this work
Tt H102G (4-Me-Im) [b]		414	568/541	this work
Tt H102G (4-Br-Im) [b]		413	570/539	this work
Tt H102G (4-I-Im) [b]		413	568/537	this work
Tt H102G (pyr) [b]		422	568/542	this work
Tt H102G (3F-pyr) [b]		420	570/539	this work
Tt Y131F		423	567/544	this work
Tt S133A		424	564/545	this work
Tt S133C		423	565/544	this work
Tt R135Q		422	566/545	this work
Tt Y140H		423	562/548	this work
Tt Y140F		424	564/547	this work
Tt P115A/Y140F		424	563/543	this work
Tt Y140L		423	562/548	this work
Tt I5L		424	565/541	[51]
Tt P115A		424	568/538	[51]
Tt I5L/P115A		424	570/542	[51]

[a] All peak positions are reported in nm.
[b] All proximal ligand concentrations were set at 1 mM.

3.4.2 Resonance Raman spectroscopy

To characterize the conformational changes of the *Tt* H-NOX heme chromophore in the mutants and the binding site interactions in solution, we performed RR measurements on the ferrous unligated and CO-bound forms (Figures 3.2, 3.4, 3.6, and 3.8). The main heme skeletal modes, ν(Fe-His), and CO-associated modes are summarized in Tables 3.3 and 3.4, and compared to other proteins [1, 67, 68, 77, 81, 103, 118-120]. The heme skeletal vibrations typically occur in the 1350-1650 cm^{-1} region, and are sensitive to the π-conjugation and core size of the porphyrin macrocycle. The π-electron density marker (ν_4) corresponds to the C_α-N symmetric stretching or pyrrole breathing mode, and is sensitive to the oxidation state of the heme. The other skeletal bands, ν_2 and ν_3, correspond to the C_β-C_β and C_α-C_m stretching vibrations, respectively. These modes are sensitive to the coordination and spin-state of the heme, and can be used to detect conformational changes within the chromophore [56, 64, 79, 103]. In addition, several heme deformation modes in the low frequency region correspond to out-of-plane modes (*e.g.* γ_{15}) and may be used to assess the heme conformation through changes in vibrational frequency or RR intensity.

Table 3.3 summarizes the RR characterization of the fully reduced, 5-coordinate *Tt* H-NOX proteins, H-NOX domains from other prokaryotes, and other histidyl-ligated heme proteins [1, 67, 68, 77, 81, 103, 118-120]. The Fe-His stretching mode, which is sensitive to interactions between the heme and the proximal histidine, can only be observed in the 5-coordinate Fe^{II}-unligated protein. In addition to providing a direct measurement of the Fe-His bond strength, ν(Fe-His) is a unique structural probe of the protein environment surrounding the bound histidine residue [63].

As shown in Table 3.3, the observed skeletal mode frequencies are typical of ferrous, high-spin heme proteins. However, a range of ν(Fe-His) values are exhibited with differences of up to ~30 cm^{-1} among different proteins [*e.g.* 197 cm^{-1}, *Tt* H-NOX H102G(Pyr) versus 231 cm^{-1}, Axcyt c']. The Fe-His stretching frequency for *Tt* H-NOX WT generally occurs at 217-220 cm^{-1} [1, 51], and the majority of the mutations made to the *Tt* H-NOX domain do not significantly perturb it by more than 1-6 cm^{-1} [51]. The exchange of the proximal ligand in the *Tt* H-NOX H102G mutant, however, produces a range of Fe-N_{im} stretching frequencies from 188 to 215 cm^{-1}. Due to the spectral similarities in the skeletal marker bands, it can be inferred that the heme conformation is minimally perturbed by these proximal substitutions for the 5-coordinate *Tt* H-NOX H102G mutant other than altering the Fe-N_{im} bond length.

The RR spectra and correlations of the *Tt* H-NOX CO complexes are partitioned in accordance with the different types of mutations made in the heme pocket (Figure 3.1): distal (Figures 3.2 and 3.3), proximal ligand substitution (Figures 3.4 and 3.5), hydrogen-bonding Tyr-Ser-Arg (YxSxR) motif (Figures 3.6 and 3.6), and heme deformation (Figure 3.8). The ν(Fe-CO)/ν(C-O) plot in Figure 3.9 summarizes and compares the backbonding trends for the *Tt* H-NOX proteins presented in this work,

Table 3.3 Observed heme skeletal mode frequencies for several H-NOX domains and other proteins in the 5-coordinate, Fe^{II}-unligated form. [a]

Protein	ν_2	ν_3	ν_4	ν(Fe-His)	Ref.
Axcyt c'	1577	1469	1351	231	[119]
AxPDEA1H	1557	1469	1354	212	[81]
β1 (1-194)	1568	1478	1359	208	[34]
β1 (1-385)	1561	1473	1355	206	[77, 118]
β1 (1-385) H105G (Im)	1561	1471	1355	221	[77, 118]
sGC	1561	1473	1355	204	[67]
β2 (1-217)	1567	1477	1359	207	[34]
HemAT-Bs	1558	1469	1352	225	[120]
Mb	1563	1471	1357	220	[103]
Vc WT	1561	1471	1354	224	[1]
So WT	1567	1474	1357	213	this work
Tt WT	1567	1471	1354	217	[51]
Tt I5L	1565	1469	1351	217	[51]
Tt P115A	1567	1469	1353	223	[51]
Tt I5L/P115A	1564	1469	1352	220	[51]
Tt W9F	1566	1470	1353	218	this work
Tt H102G (Im)	1566	1471	1354	214	this work
Tt H102G (1-Me-Im)	1566	1472	1355	212	this work
Tt H102G (2-Me-Im)	1566	1472	1357	215	this work
Tt H102G (4-Me-Im)	1566	1471	1356	214	this work
Tt H102G (4-Br-Im)	1569	1471	1356	191	this work
Tt H102G (4-I-Im)	1567	1471	1357	188	this work
Tt H102G (pyr)	1568	1472	1358	203	this work
Tt H102G (3F-pyr)	1566	1472	1358	197	this work
Tt Y131F	1566	1471	1356	218	this work
Tt S133A	1566	1471	1354	218	this work
Tt S133C	1563	1468	1354	218	this work
Tt R135Q	1566	1471	1354	218	this work
Tt Y140F	1565	1469	1353	220	this work
Tt P115A/Y140F	1567	1471	1354	220	this work
Tt Y140H	1561	1470	1353	218	this work
Tt Y140L	1564	1468	1351	220	this work

[a] All vibrational frequencies are reported in cm^{-1}.

H-NOX domains from other prokaryotic and eukaryotic organisms, and other histidyl- and thiolate-ligated heme proteins. In addition, the vibrational frequencies for all of these proteins are summarized in Table 3.4, and are characteristic of 6-coordinate, low spin, histidyl-ligated Fe^{II}-CO complexes. To clarify the frequency shifts, the ^{13}CO-isotopically substituted RR spectra are indicated with dotted lines and either overlaid or staggered beneath the natural abundance ^{12}CO complex spectra in the regions corresponding to the Fe-CO and C-O stretching modes. A simple harmonic oscillator

model was used to predict the downshifts in vibrational frequency upon isotopic substitution.

Table 3.4 Observed heme skeletal mode frequencies for the 6-coordinate Fe^{II}-CO complexes of several H-NOX domains and other proteins.[a]

Protein	ν_2	ν_3	ν_4	ν(Fe-CO)	ν(C-O)	δ(Fe-C-O)	Ref.
Axcyt c'	1596	---	1368	491	1966	572	[119]
AxPDEA1H	---	---	---	493	1973	581	[81]
β1 (1-194)	1586	1502	1375	477/496	1968	574	[34]
β1 (1-385)	1582	1496	1373	**478**[b]/494	**1987**[b]/1964	564	[68, 118]
β1 (1-385) H105G (Im) ± YC-1	1584	1499	1372	478/**495**[b]	1987/**1964**[b]	572	[118]
β1 (1-385) + YC-1	1582	1499	1372	478/491	1985/1967	---	[68]
sGC	1583	1500	1371	**472**[b]/487	1987	562	[67]
sGC + YC-1	1580	1497	1371	474/492	1987	---	[68]
β2 (1-217)	1586	1492	1372	476	1994	559	[34]
HemAT-Bs	1578	1495	1368	494	1964	---	[120]
Mb	1587	1498	1372	512	1944	577	[113, 114]
Vc WT	1578	1492	1368	491	1985	570	[1]
So WT	1581	1496	1368	494	1984	568	this work
Tt WT	1580	1496	1369	490	1989	567	[1]
Tt I5L	1579	1492	1367	490	1984	568	this work
Tt P115A	1582	1494	1370	490	1984	568	this work
Tt I5L/P115A	1579	1492	1367	488	1981	568	this work
Tt W9F	1577	1491	1367	485	1930	579	this work
Tt H102G (Im)	1580	1494	1368	492	1983	570	this work
Tt H102G (1-Me-Im)	1582	1497	1370	**493**[b]/529	1990/1961	570	this work
Tt H102G (2-Me-Im)	1585	1497	1372	497/**531**[b]	1984/**1963**[b]	---	this work
Tt H102G (4-Me-Im)	1585	1502	1372	529	1964	---	this work
Tt H102G (4-Br-Im)	1585	1499	1372	531	1963	---	this work
Tt H102G (4-I-Im)	1585	1502	1372	531	1964	---	this work
Tt H102G (pyr)	1582	1497	1370	487	1997	570	this work
Tt H102G (3F-pyr)	1584	1498	1371	**487**[b]/529	**1997**[b]/1968	570	this work
Tt Y131F	1580	1494	1370	**492**[b]/506	1919/1984	586	this work
Tt S133A	1580	1492	1367	492	1985	583	this work
Tt S133C	1579	1492	1368	**490**[b]/504	1981/1916	570	this work
Tt R135Q	1577	1489	1365	**486**[b]/497	1981/1966	567	this work
Tt Y140F	1577	1489	1367	491	1966	579	this work
Tt P115A/Y140F	1579	1491	1369	492/512	1950/1969	570	this work
Tt Y140H	1576	1491	1369	501/515	1928/1952	578	this work
Tt Y140L	1577	1492	1370	498	1932	584	this work

[a] All vibrational frequencies are reported in cm^{-1}.
[b] Vibrational frequencies in bold lettering indicate dominant CO conformer.

Mutations were generated in the distal pocket of *Tt* H-NOX to investigate how the hydrogen-bonding residues, Trp-9 and Tyr-140, modulate the binding of CO to the heme protein (Figure 3.1). The RR spectra of *Tt* H-NOX WT and proteins with distal pocket mutations at Trp-9 and Tyr-140 are juxtaposed in Figure 3.2. The correlations between the ν(Fe-His), ν(Fe-CO), and ν(C-O) are represented graphically in Figure 3.3. As previously shown [1], *Tt* H-NOX WT displays a ν(Fe-CO) stretching mode at 492 cm^{-1} which downshifts to 486 cm^{-1} upon isotopic substitution. The Fe-C-O bending mode, δ(Fe-C-O), is also detected at 569 cm^{-1}. In the high frequency region, the CO stretching mode is detected at 1987 cm^{-1} and downshifts by 46 cm^{-1} to 1941 cm^{-1} for the ^{13}CO complex. In comparison to *Tt* H-NOX WT, the W9F mutant displays a ν(Fe-CO) frequency downshift to 485 cm^{-1} upon loss of the H-bonding residue. In addition, the CO stretching frequency shows a large decrease of nearly 60 cm^{-1} to ~1930 cm^{-1} upon mutation. It is known that Trp-9 forms H-bonding contacts with Tyr-140, which is within H-bonding distance to the axial ligand [5]. Thus, it is plausible that replacement of Trp-9 with Phe only interrupts the interactions between Tyr-140 and the ligand (Figure 3.1).

Mutations at Tyr-140 with either His, Phe, or Leu produced intriguing results. In the Y140H mutant, the Fe-CO stretching mode is very broad with a peak at 501 cm^{-1} and a shoulder at ~515 cm^{-1}, suggesting that at least two CO conformations are present. This is further supported by the detection of at least two CO stretching modes at 1928 and 1952 cm^{-1}, which decrease in frequency upon isotopic substitution. In contrast, the Y140F mutant predominantly shows a single broad ν(Fe-CO) peak at 491 cm^{-1}, which shifts to 485 cm^{-1} for the ^{13}CO complex. Compared to a spectral bandwidth of ~15 cm^{-1} for the WT protein, the *Tt* H-NOX Y140F mutant ν(Fe-CO) broadens by an additional ~13 cm^{-1}. Similarly, a single weak isotope-sensitive peak is detected at 1966 cm^{-1}, and is assigned as the ν(C-O). The double mutant P115A/Y140F results in the presence of multiple CO conformations. Broad Fe-CO stretching modes are clearly detected at 492 and 512 cm^{-1}, which downshift to 487 and 506 cm^{-1}, respectively; and at least two C-O stretching modes are also detected in the high frequency region (1950 and 1964-1972 cm^{-1} downshift to 1904 and 1918-1926 cm^{-1}, respectively). Finally, the single Y140L mutant displays one CO conformation with a single broad Fe-CO stretching mode at 501 cm^{-1} and C-O stretching mode at 1930 cm^{-1}. For all proteins, the vinyl stretching mode is clearly observed at 1616-1619 cm^{-1}, with a small ~1630 cm^{-1} shoulder peak that corresponds to ν_{10}. The small fluctuations of 1-3 cm^{-1} observed in the skeletal markers for the mutants are likely a result of minor conformational changes in the heme resulting from rearrangements in the distal pocket upon mutation. These introduced conformational changes are also reflected in the subtle differences displayed in the low frequency region for ν_8 and γ_{15} at ~350 and ~704 cm^{-1}, respectively.

Figure 3.4 shows the RR spectra of *Tt* H-NOX WT and the H102G mutant with various proximal ligands. The trends observed across ν(Fe-N_{im}), ν(Fe-CO), and ν(C-O) are graphically represented in Figure 3.5. The Fe-CO frequency increases as the CO stretching frequency decreases, which is reflective of the Fe $d_\pi \rightarrow$ CO π^* back-donation.

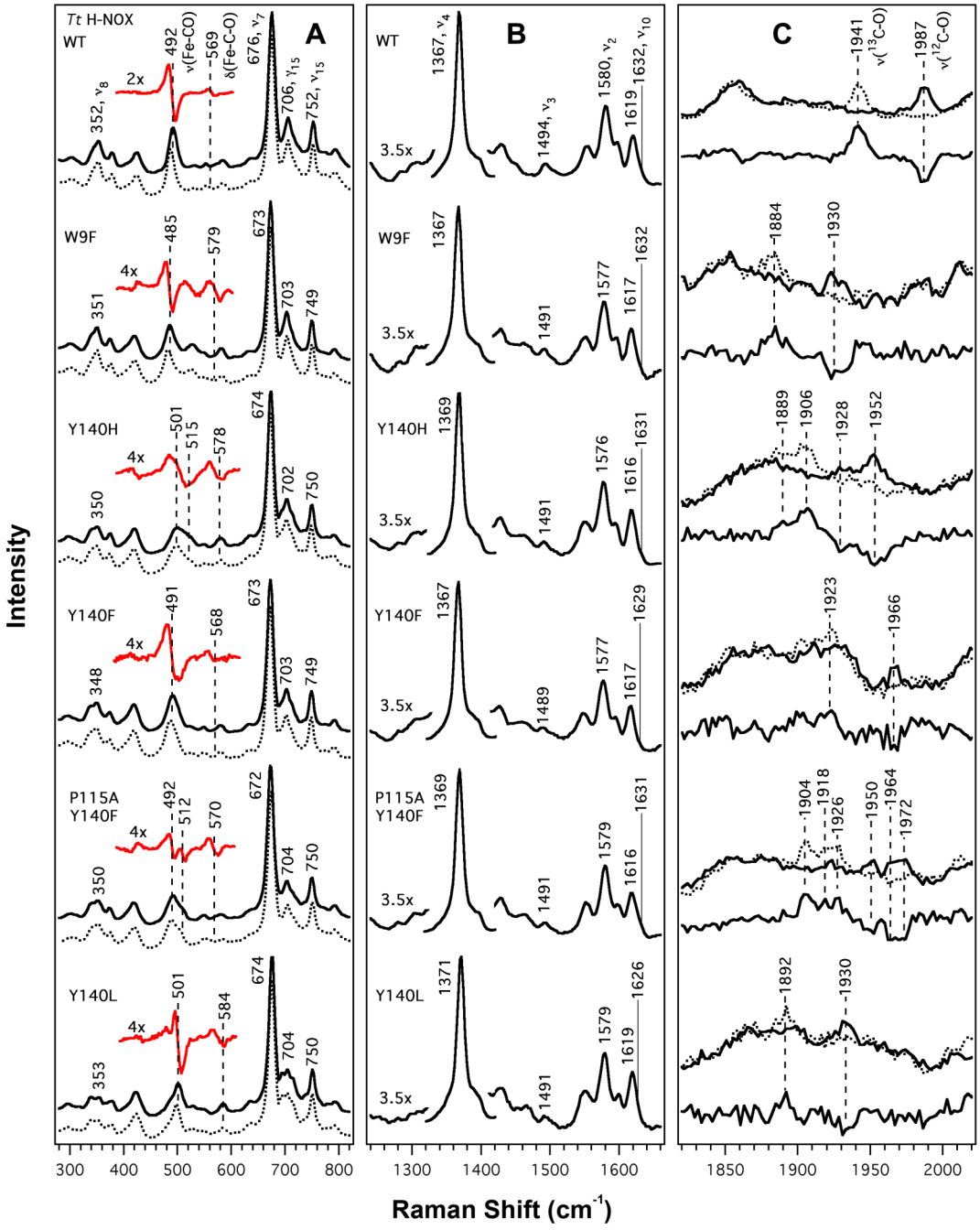

Figure 3.2 Resonance Raman spectra of the CO complexes of *Tt* H-NOX WT, W9F, Y140H, Y140F, P115A/Y140F, and Y140L. Panel (A) shows the low frequency ^{12}CO (solid line), ^{13}CO (dotted line), and magnified (2-4x) difference (^{13}CO-^{12}CO) spectra for clarity. Panel (B) shows the skeletal markers in the high frequency region; ν_4 has been shrunk to clearly display the markers. Panel (C) displays a magnified view of the CO stretch region, with ^{13}CO (dotted) and ^{12}CO (solid) overlaid, and the difference spectra (^{13}CO-^{12}CO) included below. Spectral intensities were normalized to ν_7 and ν_4 for the low and high frequency regions, respectively.

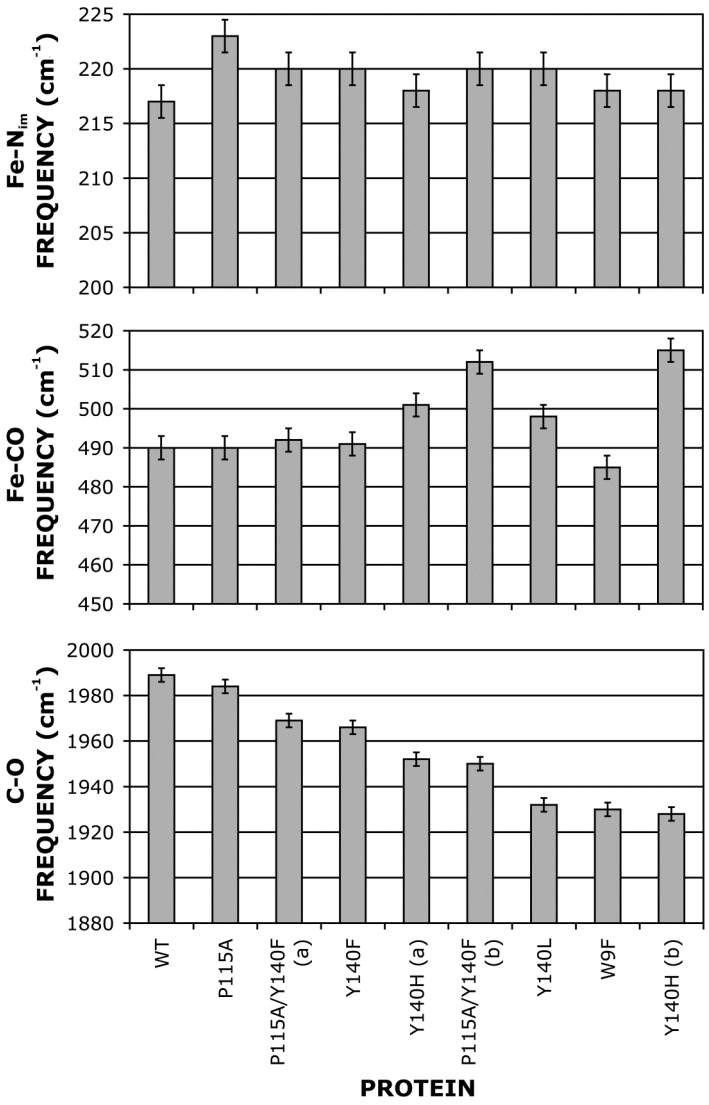

Figure 3.3 Correlation trends between the vibrational frequencies of ν(Fe-N_{im}), ν(Fe-CO) and ν(C-O) in the CO complex for *Tt* H-NOX upon mutating the distal pocket residues, Trp-9 and Tyr-140.

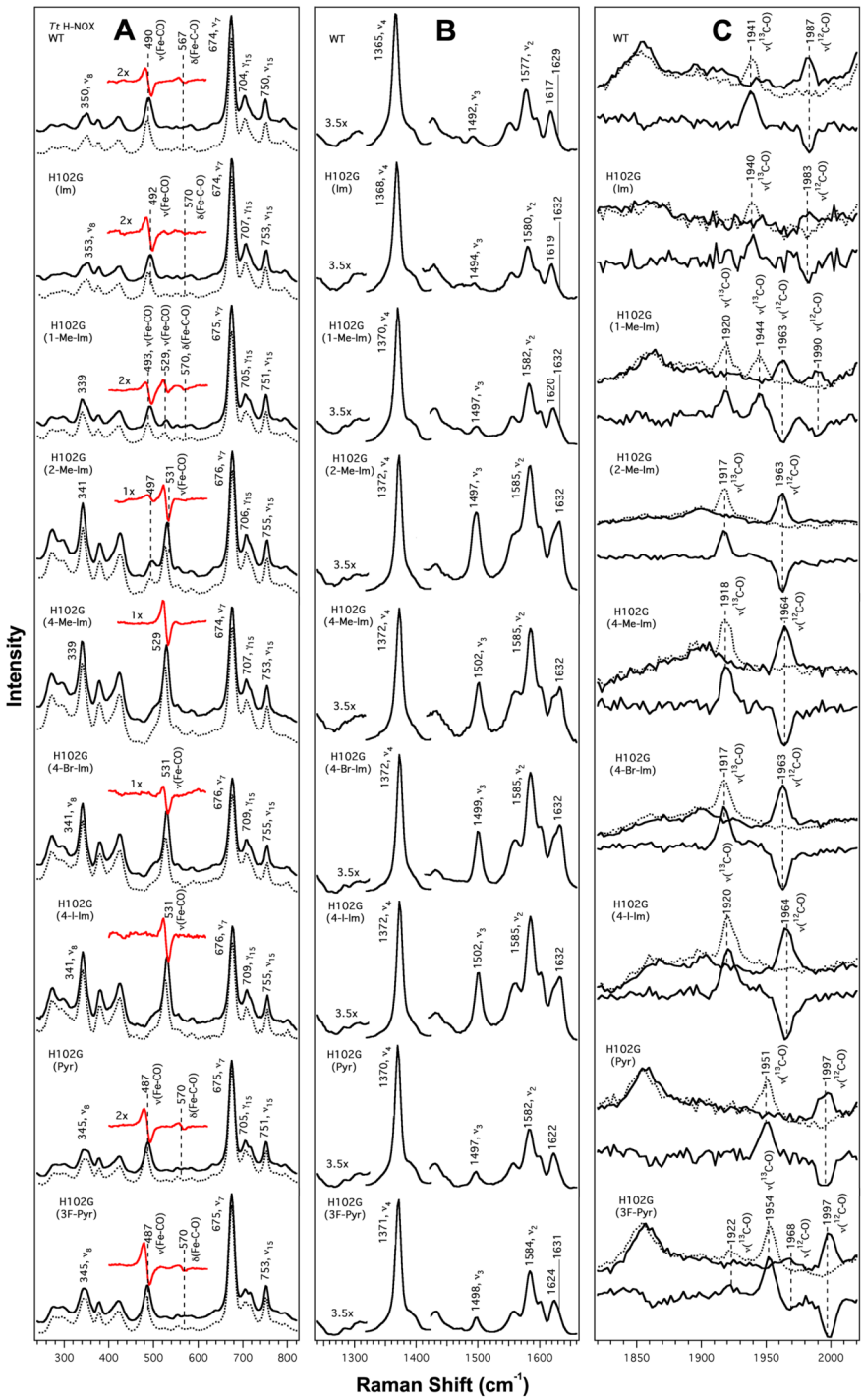

Figure 3.4 Resonance Raman spectra of the CO complexes of *Tt* H-NOX WT and the *Tt* H102G mutant with 1 mM of the following proximal ligands: imidazole (Im), 1-Me-Im, 2-Me-Im, 4-Me-Im, 4-Br-Im, 4-I-Im, pyridine (Pyr), and 3-F-Pyr. ^{13}CO spectra (dotted line) are overlapped over the ^{12}CO spectra, and the difference (^{13}CO-^{12}CO) spectra are shown below each protein. Spectral intensities were normalized to ν_7 and ν_4 for the low and high frequency regions, respectively.

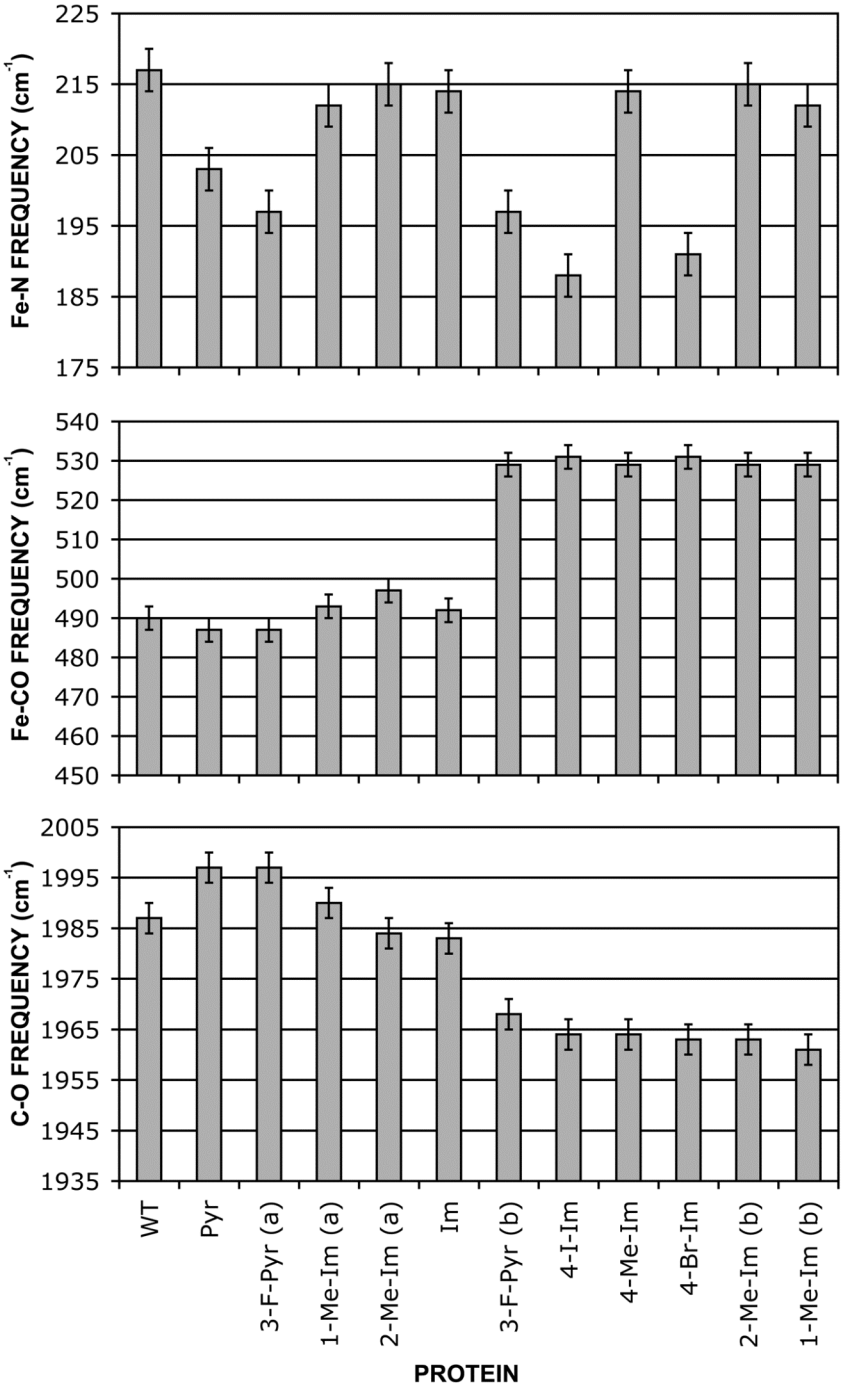

Figure 3.5 Correlation trends between the vibrational frequencies of ν(Fe-N_{im}), ν(Fe-CO) and ν(C-O) in the CO complex for *Tt* H-NOX H102G upon varying the proximal ligand.

As expected, imidazole mimics the proximal histidine residue relatively well with ν(Fe-CO) and ν(C-O) values of 492 and 1983 cm^{-1} for the *Tt* H-NOX H102G(Im) protein, which are similar to the vibrational frequencies observed for the WT protein.

However, upon the addition of single substituents to the 1-, 2-, and 4-positions of the imidazole ring, the spectra exhibit significant shifts in the vibrational frequency and intensity of the CO-related modes (Figures 3.4 and 3.5). Upon substitution of the proximal imidazole ligand to the substituent-containing imidazolate derivatives, the protein displays a dominant CO conformer with a ν(Fe-CO) band that upshifts to 526-531 cm^{-1} from 492 cm^{-1}, and a ν(C-O) peak that downshifts to 1960-1964 cm^{-1} from 1983 cm^{-1}. *Tt* H-NOX H102G proteins containing 1-Me-Im and 2-Me-Im both showed an additional conformer with a ν(Fe-CO) at ~493-497 cm^{-1} and ν(C-O) at ~1984-1990 cm^{-1}. In addition, both the pyridine and 3F-pyridine derivatives displayed a dominant heme-CO conformer with ν(Fe-CO) ~ 487-492 cm^{-1} and ν(C-O) ~ 1997 cm^{-1}. Although ν(Fe-CO) decreases by only ~3 cm^{-1}, ν(C-O) displays an upshift of nearly 10 cm^{-1} in comparison to WT. All of the CO-bound *Tt* H-NOX H102G proteins displayed downshifts of up to 11 cm^{-1} for ν_8 relative to the WT protein (ν_8 ~ 350 cm^{-1}), and small shifts are also observed in the skeletal mode frequencies. This suggests that the heme conformation of the CO-bound *Tt* H-NOX H102G proteins is altered in comparison to the WT protein, which may be due to steric disturbances in the proximal pocket from the imidazolate substituents.

The YxSxR motif is strictly conserved throughout the H-NOX family and is known to form H-bonding contacts with the propionate groups of the heme (Figure 3.1) [1, 5, 42, 47]. To investigate how the H-bonding of these residues with the propionate substituents influenced the CO complex, mutations were generated on Tyr-131, Ser-133, and Arg-135 of *Tt* H-NOX. Figure 3.6 shows the RR spectra of the CO complexes for *Tt* H-NOX WT, Y131F, S133A, S133C, and R135Q; the respective corresponding changes in ν(Fe-His), ν(Fe-CO), and ν(C-O) are summarized graphically in Figure 3.7. For all proteins, two isotope-sensitive bands at ~490 and ~569 cm^{-1} are detected in the low frequency region, which correspond to ν(Fe-CO) and δ(Fe-C-O), respectively. No significant frequency shifts are observed in these bands, although a slight spectral broadening of the Fe-CO stretching mode is evident for the *Tt* H-NOX Y131F, S133C, and R135Q mutants. Relative to the spectral bandwidth of the WT protein (~15 cm^{-1}), the *Tt* H-NOX Y131F protein's ν(Fe-CO) broadens to a width of ~25 cm^{-1}. The overall similarity in vibrational frequency is indicative of similar Fe-CO bond energetics between the WT protein and the four mutants, whereas the slight broadening of the Fe-CO stretching mode would suggest either the presence of some minor alternate conformations or a larger range of fluctuation in the softened distal pocket. The high frequency region exhibits two distinct peaks that downshift upon isotopic substitution for the CO-bound *Tt* H-NOX Y131F (1919 and 1984 cm^{-1}), S133C (1916 and 1981 cm^{-1}), and R135Q (1966 and 1981 cm^{-1}) mutants. These three mutants also display slight decreases in γ_{15} intensity at ~703 cm^{-1} relative to the WT protein, which may be suggestive of some heme relaxation. In contrast, the RR spectra of the *Tt* H-NOX S133A mutant shows a single C-O stretch at 1984 cm^{-1}, which is very similar to WT.

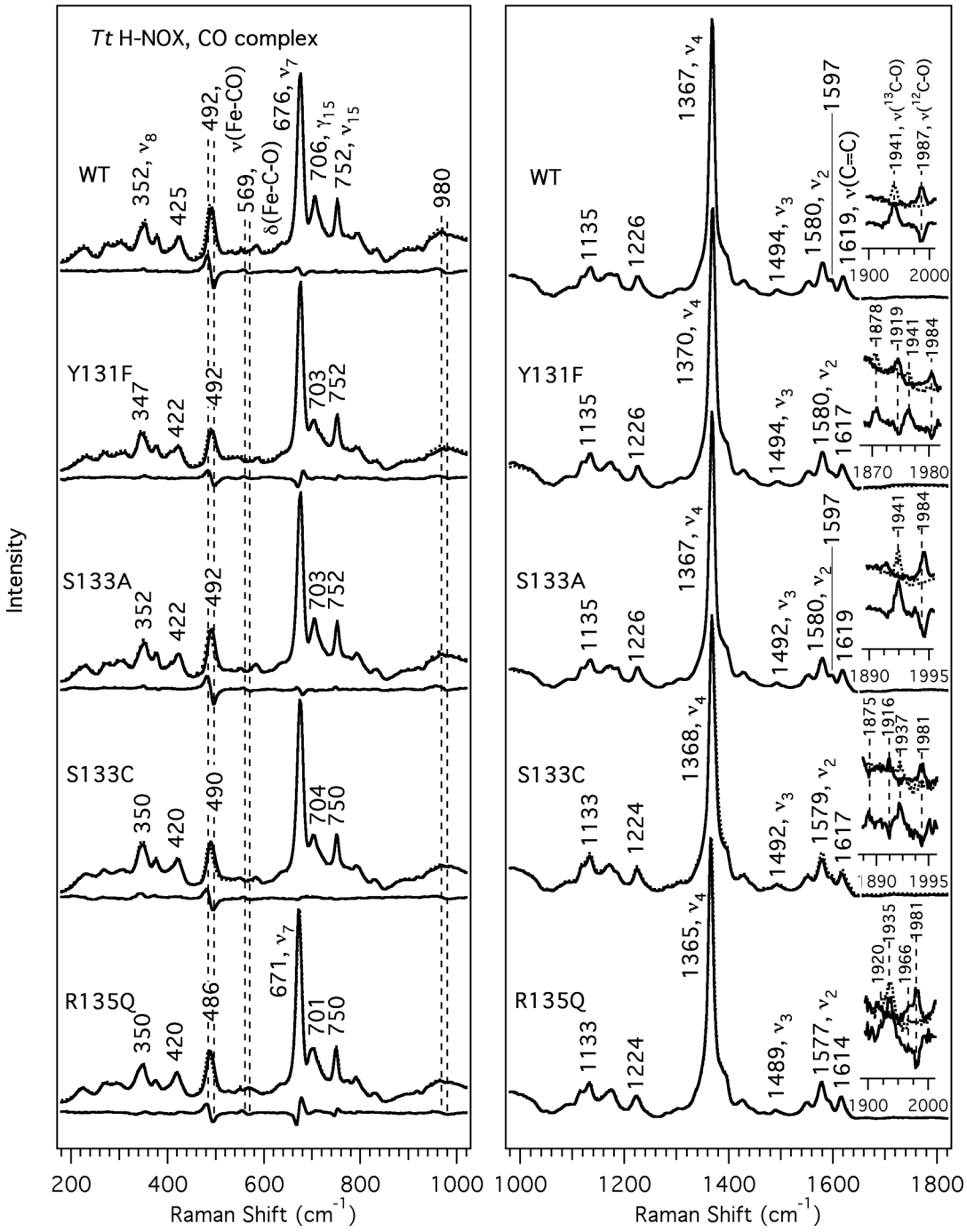

Figure 3.6 Resonance Raman spectra of the CO complexes of *Tt* H-NOX WT, Y131F, S133A, S133C, and R135Q. ^{13}CO spectra (dotted line) are overlapped over the ^{12}CO spectra to indicate the frequency shifts upon isotopic substitution, and the difference (^{13}CO-^{12}CO) spectra are shown below each protein for clarity. Insets show the isotopic shift trends for ν(C-O) in the 1850-2000 cm^{-1} region. Spectral intensities were normalized to ν_7 and ν_4 for the low and high frequency regions, respectively.

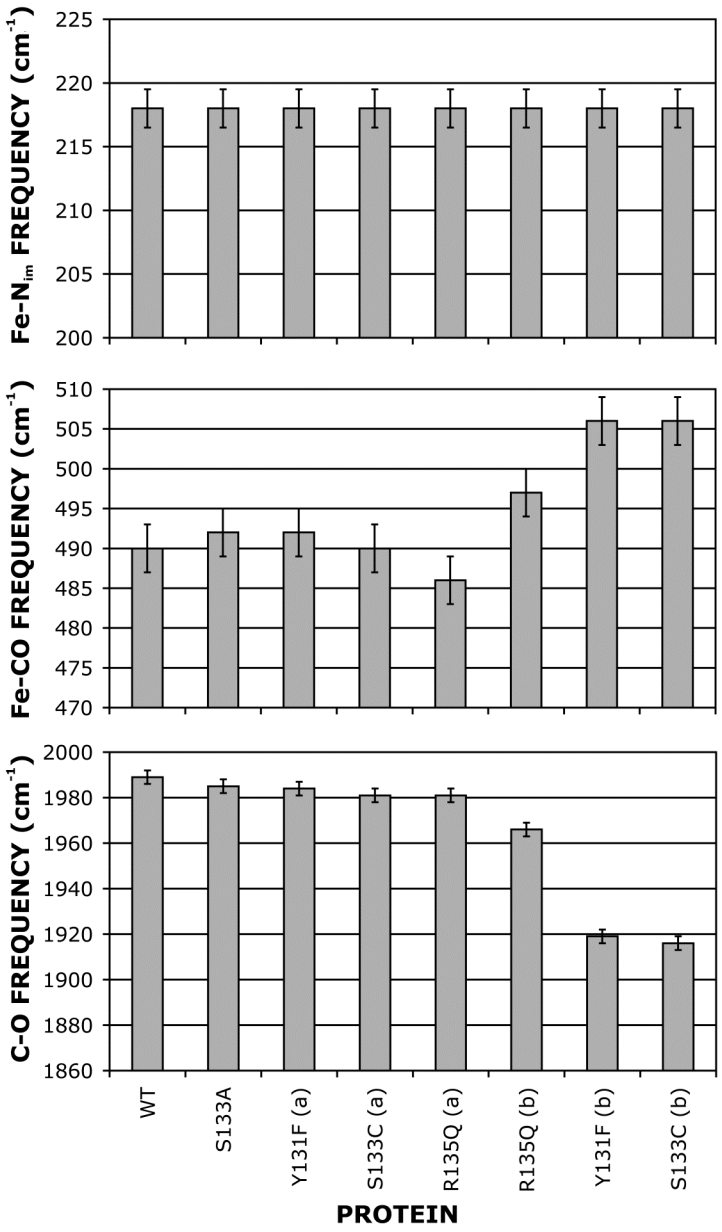

Figure 3.7 Correlation trends between the vibrational frequencies of ν(Fe-N_{im}), ν(Fe-CO) and ν(C-O) in the CO complex for *Tt* H-NOX upon mutating the strictly conserved YxSxR motif.

The difference in the degree of CO bond modulation across the mutants is likely a reflection of the amount of H-bonding that each residue forms with the propionate groups of the heme chromophore. For all proteins, the skeletal mode frequencies are very similar and the vinyl stretching mode is clearly observed at 1616-1619 cm^{-1}, with a small ~1630 cm^{-1} shoulder peak that corresponds to ν_{10}. These similarities indicate that the dominant heme conformation does not appreciably change across the different mutations.

To examine the effect of heme deformation on the CO complex, mutations were generated at Ile-5 and Pro-115, which are known to influence the heme conformation of the O_2-bound WT *Tt* H-NOX domain [5, 44, 51]. Figure 3.8 shows the RR spectra for the CO complexes of *Tt* H-NOX WT, I5L, P115A, and the double mutant. In the low frequency region, the Fe-CO stretching mode is detected at 490 cm^{-1} for the I5L mutant, and at 488 cm^{-1} for both the P115A and I5L/P115A mutants. In the high frequency region, a single C-O stretching mode is detected between 1981-1986 cm^{-1} for the three mutants. In addition to the heme skeletal modes, these measured frequencies are very similar to *Tt* H-NOX WT. Thus, these mutations do not appear to significantly disrupt the nature of the CO bond or affect the ν(Fe-CO)/ν(C-O) backbonding correlation.

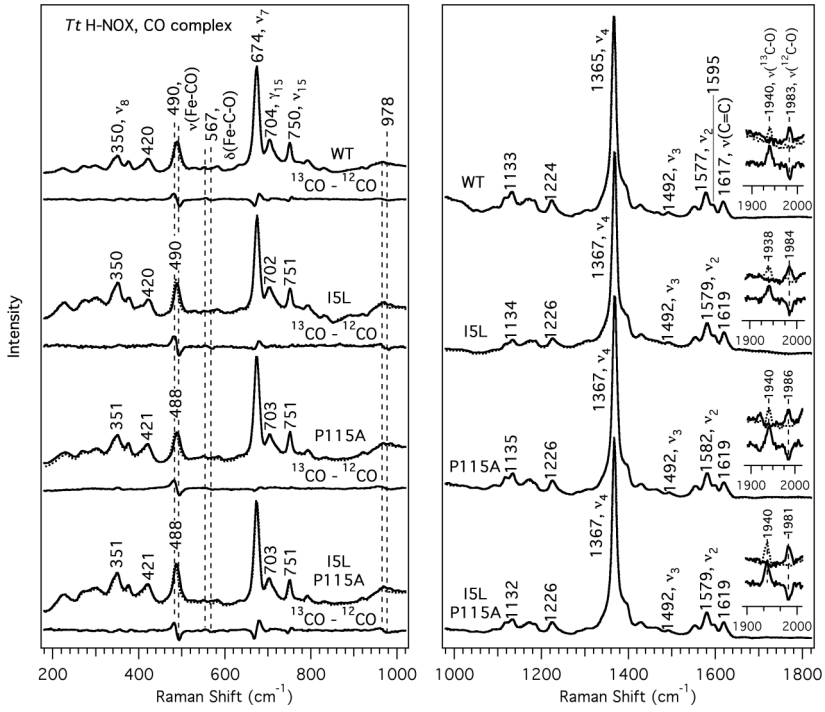

Figure 3.8 Resonance Raman spectra of the CO complexes of *Tt* H-NOX WT, I5L, P115A, and I5L/P115A. ^{13}CO spectra (dotted line) are overlapped over the ^{12}CO spectra to indicate the frequency shifts upon isotopic substitution, and the difference (^{13}CO-^{12}CO) spectra are shown below each protein for clarity. Insets show the isotopic shift trends for ν(C-O) in the 1850-2000 cm^{-1} region. Spectral intensities were normalized to ν_7 and ν_4 for the low and high frequency regions, respectively.

3.5 Discussion

A detailed interpretation of the vibrational shifts observed in the RR spectra of the CO-bound H-NOX domains allow for explanations of what these changes indicate about the possible electrostatic binding site interactions occurring in the solution solubilized H-NOX protein. In overview, the absence of these important intermolecular contacts significantly alters the tightly held heme-CO adduct, resulting in alternate CO conformations and a weakened CO bond. The ν(Fe-CO)/ν(C-O) backbonding correlation for the H-NOX domains and *Tt* H-NOX mutants are plotted and compared to other proteins, including the globins, other histidyl-ligated heme proteins, and thiolate-ligated P450s (Figure 3.9); the differences in the slope of the ν(Fe-CO)/ν(C-O) correlation line is reflective of the sensitivity of ν(Fe-CO) to backbonding. By comparing the RR data with the available NMR and x-ray crystallographic results [5, 42-44, 46], a more comprehensive understanding of the heme structure and its interactions with the H-NOX protein environment is obtained.

3.5.1 Distal electrostatic effects on CO-bound Tt H-NOX

Previous studies on heme-CO distal pocket mutations in other proteins clearly demonstrated a modulation of the ν(Fe-CO)/ν(C-O) backbonding correlation upon altering the polar interactions between the CO ligand and distal residues [75, 76, 80, 81, 84, 108, 112, 114-116]. These changes in ν(Fe-CO) and ν(C-O) are illustrated in Figures 3.9 and 3.10. Many CO-bound myoglobin variants exhibited an increase in the ν(C-O) frequency upon replacement of the distal histidine residue with nonpolar ones that cannot form H-bonding contacts with the bound CO in the distal pocket [80]. This phenomenon can be readily explained by the increased electron density that is returned to the CO moiety upon removal of the H-bond from the distal histidine residue, decreasing the effects of back donation from the Fe^{II} d_π electrons into the CO π^* orbitals and increasing the CO bond order. Of notable interest to our work with the H-NOX family is the Mb double mutant H64V/V68T, which produced vibrational frequencies of 479 and 1984 cm^{-1} for the Fe-CO and C-O stretching modes, respectively, in comparison to the native Mb protein [ν(Fe-CO) ~ 512 cm^{-1}; ν(C-O) ~1944 cm^{-1}] [80]. The diminished backbonding in this double mutant was thought to result from negative polarity in the distal pocket due to lone electron pairs from the oxygen in Thr-68 being directed at the CO ligand, forcing the electron density back to the C-O bond and increasing its bond order. Similar trends were previously demonstrated in superstructured model porphyrins with naphthalene hydroxyl groups overhanging the bound CO moiety [121].

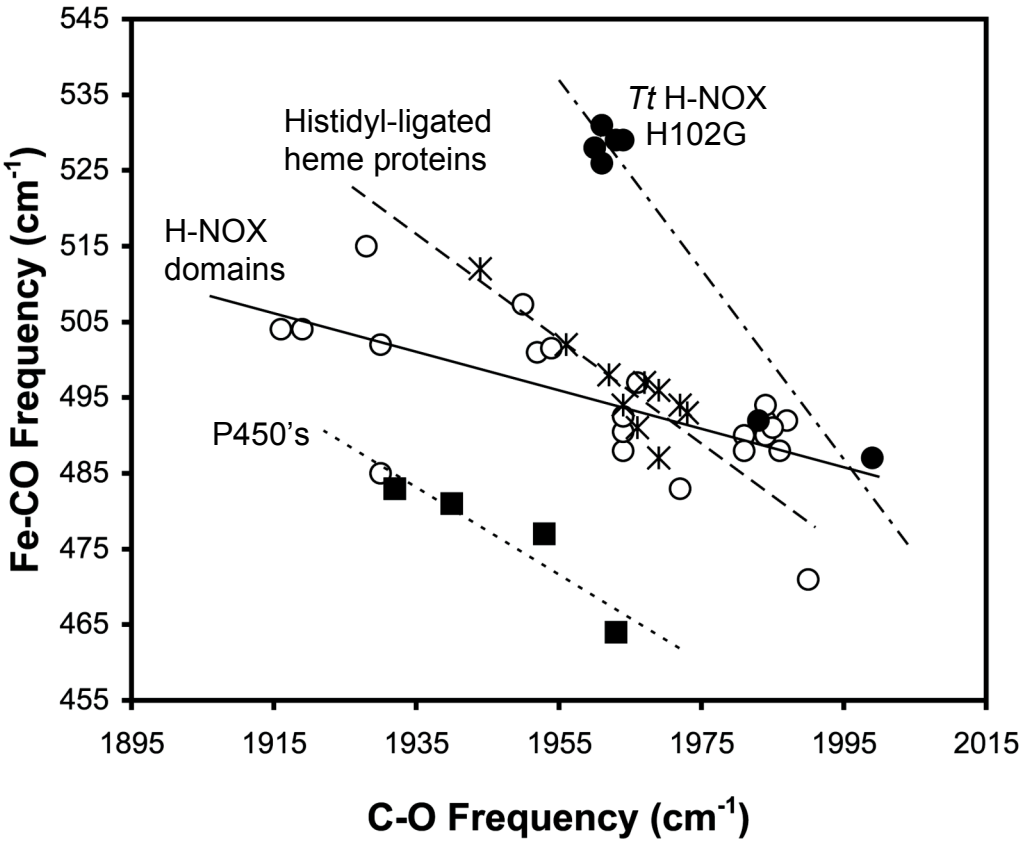

Figure 3.9 Backbonding correlation plot between ν(Fe-CO) and ν(C-O) for several H-NOX domains and other heme proteins. The CO-bound heme proteins and their corresponding symbols for the plot are as follows: H-NOX domains (○); *Tt* H-NOX H102G with substituted proximal ligands (●); other histidyl-ligated heme proteins (⁕); P450's (■).

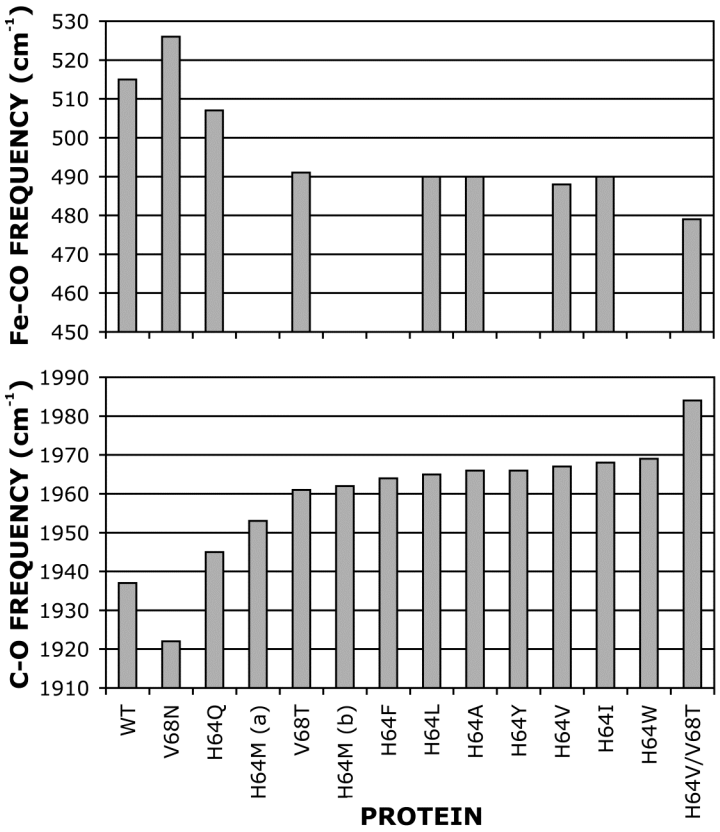

Figure 3.10 Correlation trends between the vibrational frequencies of ν(Fe-CO) and ν(C-O) in the CO complex for myoglobin and its distal pocket mutations. The majority of the C-O measurements came from FTIR studies; thus, some Fe-CO frequencies were not observed [80, 113, 114].

The *Tt* H-NOX WT protein has a CO stretching frequency very similar to that of the Mb H64V/V68T double mutant; thus, the *Tt* H-NOX distal pocket may also contain a localized negative polarity with the oxygen from Tyr-140 directly above the CO ligand (Figure 3.1). Although no crystal structures of the CO-bound *Tt* H-NOX domain are available, the previous crystallographic and structural studies from Pellicena *et al.* [5], Ma *et al*. [43], and Erbil *et al*. [42], strongly indicate that the CO would bind in a mostly linear conformation in the heme pocket and be close enough to directly interact with the hydroxyl group of the Tyr-140 distal residue as indicated in the simplified schematic representation of the *Tt* H-NOX distal pocket (Figure 3.1). Interestingly, our RR spectra indicate a decrease in the C-O stretching frequency upon disruption of the H-bonding network in *Tt* H-NOX, which is the opposite of the trends previously observed in Mb (Figure 3.10) [76, 80, 108, 112-114]. Initially, we conjectured that a water molecule entered the heme pocket of the distal mutants and formed strong H-bonds with the CO ligand. To test this hypothesis, RR spectra of the CO-bound *Tt* H-NOX Y140L mutant were collected in buffer containing D_2O (unpublished spectra). However, no shift was observed for the C-O stretching mode; hence, we conclude that no H-bonds

existed between the axial CO ligand and water. If we follow the original argument of the Mb H64V/V68T double mutant and consider the possibility of the lone e- pairs from the Tyr-140 oxygen being pointed toward the CO moiety, then the negative polarity is abolished upon substitution of Tyr-140 with a hydrophobic residue (Figure 3.11). A hydrophobic residue, such as phenylalanine, would not have the two lone pairs of electrons to reduce the Fe $d_\pi \rightarrow$ CO π^* backbonding in the way that the distal Tyr-140 does, resulting in a weaker C-O bond as observed in our RR spectra.

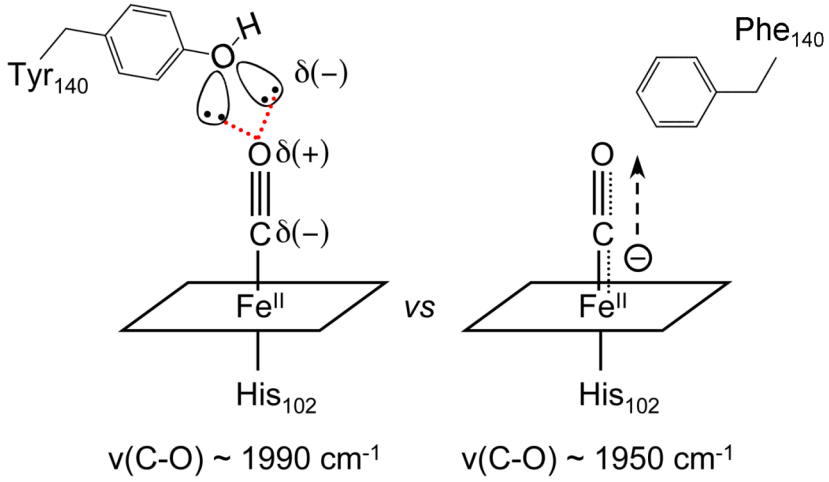

Figure 3.11 Interaction between Tyr-140 and CO in *Tt* H-NOX. The electron lone pairs from Tyr-140 point toward the CO moiety in *Tt* H-NOX WT. Upon mutation to a hydrophobic residue, the negative polarity introduced by Tyr-140 is abolished so back-donation from the Fe^{II} d_π orbital into the CO π^* orbital increases, weakening the CO bond strength.

To further investigate the influence of H-bonding residues on the C-O stretching frequency, we focused our attention to the nearby Trp-9 residue in the distal pocket of *Tt* H-NOX. Trp-9 is within H-bonding contact with Tyr-140, and is thought to hold Tyr-140 in place for H-bonding with exogenous diatomic ligands bound to the H-NOX domain (Figure 3.1). Mutation of Trp-9 to phenylalanine disrupts this H-bonding network, and a significant downshift of ~60 cm^{-1} is observed in ν(C-O). The ν(Fe-CO) similarly downshifts to 485 cm^{-1} and broadens relative to the WT protein. The observed broadening of the Fe-CO stretching mode may reflect the fact that the Tyr-140 residue is held less tightly in place upon disruption of the H-bonding network; thus, the interactions between the distal residues and CO are likely more transient. As a result, the Tyr-140 residue may not be pointed directly at the CO ligand, and its oxygen lone pairs would have a weaker effect on the CO stretching frequency. The fact that the Fe-CO stretch actually displays a decrease in frequency despite such a large decrease in the C-O stretching frequency strongly suggests that there are other effects counterbalancing the increased back donation from the Fe^{II} d_π electrons into the CO π^* orbitals due to

structural rearrangements in the heme pocket upon mutation. Distal electrostatic interactions with the CO ligand have already been shown to significantly influence the C-O stretching frequency [76, 108, 109, 113, 116]. In the case of *Tt* H-NOX, even mutations to secondary H-bonding residues produce significant shifts in vibrational frequency, reflecting the structural rearrangements within the distal pocket and changes in binding site interactions upon mutation of the distal pocket.

Another unique aspect of the RR spectra was the presence of multiple CO conformers upon mutation of Tyr-140 to histidine, with two observed ν(C-O) frequencies at 1928 cm^{-1} and 1952 cm^{-1}. This downshift in vibrational frequency suggests that the distal environment in *Tt* H-NOX Y140H more closely resembles Mb, sharing similar backbonding properties with the weaker H-bonding histidine residue in place of tyrosine. The only other distal pocket mutant to display multiple CO conformations was the double mutant, *Tt* H-NOX P115A/Y140F, which displayed broad CO stretching modes at 1950 and 1964-1972 cm^{-1}. We have previously suggested that the single P115A mutation may sufficiently disrupt the hinging region of the H-NOX domain, resulting in a more 'open' conformation that relaxes the heme [42, 51]. This increased opening of the distal and proximal halves of the H-NOX domain would certainly provide more dynamic disorder within the heme pocket, making accessible protein-ligand contacts more transient. This effect, in combination with the additional structural rearrangements to accommodate the Y140F mutation, is plausibly responsible for the multiple conformations observed in the P115A/Y140F double mutant.

Although the idea of a localized negative polarity from the hydroxyl group of the Tyr-140 residue in the distal pocket provides a reasonable interpretation for the high ν(C-O) in *Tt* H-NOX and the consequent downshifts in frequency upon distal pocket mutation, it does not extend to the rest of the H-NOX family due to the absence of this residue in many of the H-NOX domains from the facultative aerobes. In fact, structural studies on the H-NOX domains from *Shewanella oneidensis* and *Nostoc sp* indicate a predominantly nonpolar distal pocket lined with mostly hydrophobic residues [42, 43]. Thus, other contributing factors (*e.g.* electrostatic or steric) from the H-NOX heme pocket must also play a role in the unusually high ν(C-O) frequency.

3.5.2 Modulation via the proximal ligand

It is well known that the ligand at the axial coordination site *trans* to the CO influences the backbonding between the Fe^{II} and CO. This occurrence is readily observed from the backbonding plots showing the ν(Fe-CO)/ν(C-O) correlations among heme proteins with different proximal ligands (*e.g.* imidazole versus thiolate) [63, 69, 80, 84, 109, 110, 116]. Vogel *et al*. also previously showed that the ligand *trans* to the CO can displace the backbonding plots, altering the slopes and lower the Fe-CO stretching frequency. Changes in the backbonding slope depends on the donor strength of the proximal ligand, and occur due to the competition between the proximal ligand

and CO for σ-orbital overlap with the Fe^{II} acceptor orbital, d_z^2 [116, 117]. With the increased electron density on the heme metal, backdonation from Fe^{II} d_π to CO π^* is increased and the C-O bond weakens.

Tt H-NOX WT has a Fe-His stretching frequency of ~217 cm^{-1}, indicative of a moderate H-bond to the proximal ligand in comparison to no H-bond [ν(Fe-His) ~200 cm^{-1}] and a strong H-bond [ν(Fe-His) ~240 cm^{-1}] [63]. Based on its similarity in vibrational frequency, it is possible that the *Tt* H-NOX WT protein contains a Mb-like imidazole H-bond to either a carbonyl group of the protein backbone, a nearby proximal residue, or water. No crystal structures of the Fe^{II}-unligated *Tt* H-NOX exist, so it cannot be said for certain what is forming this moderate H-bond with His-102 in *Tt* H-NOX. Given the importance of the Fe-His linkage in signal transduction, changes in the proximal pocket and alteration of electrostatic contacts to the histidine residue upon ligand binding may be employed in signaling in the H-NOX family.

Despite the varying Fe-His strength among the different members of the H-NOX family, the observed ν(Fe-CO) and ν(C-O) frequencies remain remarkably similar. Thus, it does not appear that the strength of the Fe-His bond alone contributes to the unusually high C-O stretching frequency despite differences in ν(Fe-His) of up to ~15 cm^{-1} among the various members of the H-NOX family (Tables 3.3 and 3.4). In contrast, the *Tt* H-NOX H102G mutant displayed ν(Fe-CO) upshifts of ~30-40 cm^{-1} and ν(C-O) downshifts of ~25-30 cm^{-1} with different proximal ligands. There are several possible explanations for these spectral differences between the *Tt* H-NOX H102G proteins and WT, including: (i) the changes in the ligand pKa, (ii) the size and strain of the ligand within the proximal pocket, (iii) the ability to form H-bonds with nearby proximal residues or the protein backbone, and (iv) the orientation and tilt angle of the proximal ligand plane with respect to the heme normal plane. Since the vibrational frequencies for the Fe-CO and C-O stretching modes in *Tt* H-NOX H102G(Im) are similar to those of the WT protein, it is clear that the substantial shifts observed for the other proximal ligands are directly related to the additional substituents. From the inverse relationship between the Fe-CO and C-O stretching mode frequencies, it is evident that these modes are coupled. Depending on the change in the net coupling between these two modes, the vibrational frequencies for ν(Fe-CO) and ν(C-O) will shift accordingly. Thus, geometric distortions in either the Fe-N_{im} or Fe-CO bonds are likely to alter this vibrational coupling, modulating the Fe $d_\pi \rightarrow$ CO π^* backdonation and affecting the magnitude of the ν(Fe-CO) and ν(C-O) shifts.

Our results suggest that the proximal ligands with substituents serve as *trans* ligand electron donors which enhance the backbonding effect, thereby diminishing the ν(C-O) and increasing ν(Fe-CO). As shown in the backbonding correlation plot (Figure 3.9), the slope for the *Tt* H-NOX H102G mutants is steeper relative to that for the globins and the other H-NOX domains. The observed changes in ν_8, low frequency mode intensities, and high frequency skeletal modes strongly support changes in the heme conformation to accommodate the substitution of the proximal ligand. Although the decrease in the ν(Fe-N_{im}) frequency upon addition of electronegative substituents may partially be responsible for the increased ν(Fe-CO) frequency, the proximal steric bulk

from the imidazolate substituents can also alter the binding site interactions. Due to these steric interactions, the heme deformation and/or position within the pocket may change, causing structural rearrangements within the pocket that introduce different distal interactions with the CO ligand. This may explain the increased ν(C-O) frequency for the *Tt* H-NOX H102G(Pyr) and H102G(3F-Pyr) proteins to 1997 cm^{-1} in comparison to the WT protein [ν(C-O) ~ 1987 cm^{-1}] despite the significantly reduced ν(Fe-N_{pyr}) frequencies of 203 and 197 cm^{-1} for pyridine and 3-F-pyridine, respectively. Furthermore, NMR structures of the CO-bound WT H-NOX and homologous H103G mutant from *Shewanella oneidensis* (*So* H-NOX) were solved by Erbil *et al.* [42], and found notable ensemble differences between the two structures which suggested changes in the van der Waals contacts between the protein and the heme. The majority of these shifts occurred in the secondary structure region flanking the proximal pocket. In addition, Erbil *et al.* showed that the heme deformation changed between the *So* H-NOX WT and H103G mutant structures, which is in agreement with the observed changes in the RR spectra for the CO-bound *Tt* H-NOX WT and H102G mutants containing proximal ligands with substituents. Thus, it is possible that changing the proximal ligand from imidazole to imidazolate derivatives containing substituents forces the heme into alternate conformations that interact differently with the binding pocket, causing more pronounced changes in ν(Fe-CO) and ν(C-O) than previously observed with Mb H93G and with other H-NOX domains containing Fe-His bonds of varying strengths [1, 34, 69, 109, 110].

3.5.3 Importance of the conserved YxSxR motif

The x-ray crystal structure of WT *Tt* H-NOX first demonstrated the importance of the conserved YxSxR motif in maintaining the heme orientation in the H-NOX family via the H-bonds between these residues and the propionate substituents of the heme prosthetic group [5]. The x-ray crystal structure shows that Tyr-131 and Ser-133 are within H-bonding distance to one of the propionates, whereas Arg-135 makes contacts with both propionate groups. Recent DFT calculations by Xu *et al.* indicate that the neutralization of these negatively charged propionate groups on the heme can modulate the ν(Fe-CO)/ν(CO) backbonding correlations in a manner similar to electron-withdrawing substituents on porphines, and alters the ν(C-O) frequency by up to ~20 cm^{-1} [91]. Our RR spectra not only show significant changes in the ν(Fe-CO) and ν(C-O) frequencies for these YxSxR mutants in *Tt* H-NOX [*i.e.* up to ~70 cm^{-1} shift for ν(C-O)], but also exhibit surprising dynamics within the heme pocket upon mutation of these residues which have not previously been reported. These results provide direct evidence for the importance of the YxSxR motif in stabilizing the heme position and orientation in the H-NOX pocket in the solution supported protein (Figure 3.1).

Mutation of Tyr-131 to phenylalanine in *Tt* H-NOX results in the presence of two dominant CO conformers. One form exhibits vibrational features similar to the WT protein, with ν(Fe-CO) and ν(C-O) at ~492 cm^{-1} and 1984 cm^{-1}, respectively. The second conformer displays a significantly lower ν(C-O) at 1919 cm^{-1}, yet no other

isotope-sensitive band was detected in the lower frequency region for the Fe-CO stretching mode. This mutation abolishes one of the H-bonding contacts between the YSR motif and a propionate group. Similarly, the S133C and R135Q mutants display two ν(C-O) bands, but only one dominant ν(Fe-CO) band. Whereas S133C disrupts only one H-bonding contact to one propionate group, the R135Q mutation disrupts H-bonding interactions with both propionate groups. Closer inspection and spectral deconvolution of the low frequency region in all three RR spectra revealed that a small shoulder upshifted from the ~490-492 cm^{-1} Fe-CO stretching band is present at ~504 cm^{-1} that can be attributed to the second CO conformer. Due to its proximity to the dominant ~492 cm^{-1} mode, the minor ~504 cm^{-1} band could not be detected in the isotope difference spectra. The presence of two CO stretching frequencies, one of which is very similar to the WT protein, may be resulting from a fluctuating swivel motion of the heme prosthetic group upon destabilization of the H-bonding residues that fix it in place. The heme plausibly interchanges between a conformation that retains similar protein-ligand contacts as *Tt* H-NOX WT, and another conformation that suggests a very strong H-bond with the CO ligand based on the significantly reduced ν(C-O) frequency of ~1916-1919 cm^{-1}. The source of this strong H-bond could be a water molecule that enters the distal pocket upon mutation due to increased accessibility. The lack of a more appreciable shift in the Fe-CO stretching mode despite such a huge change in the C-O stretching frequency indicates that there are likely two processes occurring which counterbalance each others' effects on the Fe-CO bond strength. DFT calculations have shown that the transition moment essentially lies along the vector formed by the Fe-C bond, so C-O stretching vibrations induce electrons to travel throughout the π system [80, 107, 122, 123]. Thus, it is not unreasonable to consider a redistribution of the heme π-conjugation system upon disruption of the neutralizing H-bonds between the propionate groups and the YxSxR motif, which could affect the Fe-CO bond strength.

In contrast, only a single CO conformation is observed in the *Tt* H-NOX S133A mutant with similar Fe-CO and C-O stretching frequencies to those of the WT protein. Ser-133 is sandwiched between Tyr-131 and Arg-135 in the YxSxR motif, and is only within H-bonding distance of one of the propionate groups. It is likely that its replacement with alanine resulted in a rearrangement of the remaining Tyr-131 and Arg-135 H-bonds such that the propionate groups still retained electrostatic interactions with the other two residues; thus, the heme remains in its tightly held position within the H-NOX pocket as in the WT protein. This interpretation is further supported by the spectral similarities between the CO complexes of *Tt* H-NOX WT and S133A in both the vibrational frequencies of the skeletal modes and the relative intensities of the low frequency out-of-plane modes (*i.e.* γ_{15} ~ 706 cm^{-1}). In contrast, the *Tt* H-NOX Y131F, S133C, and R135Q mutants all exhibit small shoulder bands [*e.g.* δ(C_β-vinyl) and δ(C_β-CH_3)] or slightly decreased RR intensity with broad shoulder peaks (*i.e.* γ_{15} ~ 701-704 cm^{-1}) in comparison to the WT protein; this is indicative of alternate heme conformations and/or interactions within the protein pocket.

3.5.4 Influence of the Ile-5 and Pro-115 residues on CO adducts

Our RR spectra agree with the DFT calculations of Xu *et al.* in that there is minimal effect of mutating the residues responsible for heme distortion on the Fe-CO and C-O stretching modes in *Tt* H-NOX [91]. Although the Ile-5 and Pro-115 mutations have been shown to slightly alter the Fe-His strength and influence the heme conformation for the O_2 complexes [51], both the Fe-CO and C-O frequencies remain remarkably similar to the WT protein at ~490 and ~1985 cm^{-1}, respectively. The skeletal heme modes do not appreciably shift in frequency, nor do the heme deformation modes display changes in RR intensity. Thus, the heme-CO adduct retains binding site interactions similar to those of the WT protein.

3.5.5 Modulation of the CO bond in sGC and the H-NOX family

It is clear from the RR studies on *Tt* H-NOX and its mutants that a number of factors can influence and likely contribute to the ν(Fe-CO) and ν(C-O) frequencies (Figure 3.1). Some protein-ligand interactions, such as the H-bonding in the heme pocket, have a more significant impact in modulating the back donation of the Fe^{II} d_π electrons into the CO π^* orbitals. Unexpectedly, in the case of the H-NOX family, the most important factor contributing to the ν(C-O) stretch may be the neutralization of the negative charges on the propionate groups via the YxSxR motif. Not only is this motif conserved throughout this class of heme proteins, but it clearly plays an important role in retaining the position of the heme molecule within the protein pocket, as is evident from the RR spectra. Disruption of the tightly held H-bonds results in altered protein-heme and protein-ligand interactions that modulate the properties of the H-NOX domain. Not only would electron density from the H-bonds between the YxSxR motif and the propionate groups be redistributed to the heme π-conjugated macrocycle, but the increased electron density at the metal center would also increase the Fe^{II} $d_\pi \rightarrow$ CO π^* donation. The subsequent heme swiveling motion within the binding site of these YxSxR mutants would also introduce the H-NOX domain to alternate interactions that are very different from the WT protein. It is well known that electron donating and withdrawing groups, whether from porphyrin substituents or nearby polar residues, influence the extent of backbonding in heme proteins [69, 72, 75, 76, 80, 84, 107-110, 112-114, 116, 117, 123, 124]. As the backbonding increases, the Fe-CO stretching frequency rises and the C-O stretching frequency falls. Thus, the YxSxR motif is a critical feature throughout the H-NOX family, not only for the maintenance of both proximal and distal contacts with the heme-CO adduct, but for its electrostatic interactions with the porphyrin's propionate substituent groups that clearly influence the ν(C-O) frequency.

Previous RR studies on sGC and the truncated β1 heme domain showed the presence of two CO conformers based on the detection of two Fe-CO stretching frequencies at ~478 and ~487-496 cm^{-1} [34, 36, 37, 68, 73, 77, 118]. The majority of these results

only reported one stretching frequency for ν(C-O); this discrepancy is likely due to the weak intensity inherent to the C-O stretching mode in RR spectra and the difficulty in obtaining large quantities of full length sGC. Still, an interesting aspect of these prior investigations was that the heme conformer population would shift in favor of one conformation [ν(Fe-CO) ~ 492 cm^{-1}] over the other [ν(Fe-CO) ~ 474 cm^{-1}] upon addition of the benzylindazole derivative, YC-1 [3-(5'-hydroxylmethyl-3'-furyl)-1-benzylindazole]. Although much is still unknown about how this small molecule works with the 6-coordinate CO-bound sGC to mimic the fully activated 5-coordinate NO-bound enzyme, it may involve the electrostatic interactions between the conserved YxSxR motif and the propionate side chains of the heme. Our RR results with the YxSxR mutants of *Tt* H-NOX show remarkable vibrational shifts that are indicative of significant changes in the binding site interactions; thus, these residues may also play an important role in modulating the activation of CO-bound sGC by altering the heme conformation from inactive to active.

3.6 Acknowledgements

We would like to thank Drs. Emily E. Weinert and Hans K. Carlson for their help with preparing some of the protein samples for resonance Raman measurements, members of the Mathies and Marletta labs for helpful discussions, and former Marletta lab rotation student, Patrick Visperas, for preliminary characterization of the YxSxR mutants. We also thank Drs. Mohammed Ibrahim and Thomas G. Spiro at the University of Washington for providing useful feedback and suggestions on the RR spectra. Dr. Kathleen Durkin at the Molecular Graphics and Computation Facility is also gratefully acknowledged for her help with modeling the dynamics of the *Tt* H-NOX Y131F CO complex.

Chapter 4

Resonance Raman Characterization of the Fe-O_2 Bond in *Tt* H-NOX

4.1 Abstract

An accurate description of the chemical nature of the O_2 moiety in the *H*eme *N*itric oxide/*OX*ygen binding (H-NOX) domain from *Thermoanaerobacter tengcongensis* (*Tt* H-NOX) is important for elucidating its ligand binding properties. Thus, resonance Raman (RR) spectroscopy was used to investigate the effect of mutations that either disrupt the distal H-bonding network between Trp-9, Asn-74, and Tyr-140 or add steric bulk within the binding site. Evidence of H-bonds to the bound O_2 was demonstrated by changes in its Fe-O_2 stretching frequency in the W9F, Y140H, and P115A/Y140F mutants. These mutations increase ν(Fe-O_2) in *Tt* H-NOX by returning electron density to the Fe-O_2 bond due to the abolished electrostatic interaction between the distal residues and O_2, suggesting that Tyr-140 predominantly interacts with the proximal rather than terminal oxygen atom of the O_2 moiety. Furthermore, substitution of a distal phenylalanine residue (Phe-142) with tyrosine in the second H-NOX domain from *Legionella pneumophila* (*Lp* H-NOX2) was previously shown to convert this protein into one that binds O_2. Here, the importance of this H-bond in *Lp* H-NOX2 F142Y for O_2 discrimination is demonstrated through RR spectroscopy. *Tt* H-NOX mutations at Ile-5, Ile-75, and Leu-144 were also generated to add steric bulk to the heme pocket. The RR spectra of these mutants exhibited ν(Fe-O_2) downshifts relative to the WT protein, indicative of a lengthened Fe-O_2 bond. These shifts suggest that the bulky residues increased the distance between Tyr-140 and O_2, reducing the ability of Tyr-140 to pin the diatomic molecule down into a stable O_2 complex. Our results indicate two distinct factors influence ν(Fe-O_2): (i) electrostatic effects from the H-bonding of Tyr-140, which increase the ν(Fe-O_2) frequency upon its removal; and (ii) steric effects which decrease ν(Fe-O_2) due to bond lengthening from a loosely held O_2 ligand.

4.2 Introduction

Insight into the energetics and protein-ligand interactions in many heme proteins is a critical aspect of understanding their vastly diverse structures and functions. Despite extensive studies on hemoglobin (Hb), myoglobin (Mb), and synthetic heme models, there is still much to be elucidated, not only in the globins, but also in the novel classes of heme sensor proteins that have emerged over the years [2, 39, 47, 81, 94, 124, 125]. In particular, comparisons across these different families of heme proteins is inevitably complicated due to differences in protein fold, divergence in the types of residues that line the heme-binding cavity, and variation in the kinds of interactions that occur within the protein pocket. Thus, among the novel families of heme proteins, it is important to ascertain the chemical and physical properties that are specific to each group.

With the discovery of the *H*eme-*N*itric oxide/*OX*ygen (H-NOX) binding domain and the subsequent structural determination of several H-NOX domains from different organisms, site-directed mutagenesis can be readily coupled with biophysical characterization to systematically probe the interactions between the distal diatomic ligand (*i.e.* CO, NO, or O_2), the heme prosthetic group, and the surrounding protein environment [1, 2, 5, 42, 43, 46]. It is well known that soluble guanylate cyclase (sGC), the mammalian NO receptor, contains a protoporphyrin IX prosthetic group like the O_2-binding globins, but discriminates against O_2 binding in favor of NO [27]. Boon *et al.* demonstrated that a distal tyrosine (Tyr-140) in the H-NOX domain from *Thermoanaerobacter tengcongensis* (*Tt* H-NOX) was a major factor in the ability of this protein to bind O_2 and form a stable complex (Figure 4.1) [38]. Subsequent structural and vibrational studies have also established the role of the conserved Pro-115 residue in maintaining the heme conformation in *Tt* H-NOX [44, 51]. It is clear from these and other studies that the surrounding residues control the immediate heme environment through polar, hydrophobic, or steric interactions within the binding site. However, there are still questions that remain about how these interactions specifically modulate the protein pocket in the H-NOX family to allow some domains to bind CO, NO, and O_2, while others discriminate against O_2.

Due to its selectivity for the heme chromophore, resonance Raman spectroscopy is a powerful tool for investigating heme conformational changes in a protein environment [56, 57]. Since the ligands are coupled electronically to the heme, vibrational modes from both the heme and bound ligand are enhanced upon resonance excitation with the Soret band. These vibrational frequencies are sensitive to molecular conformation and chemical interactions, providing significant insight into the strength of the bonds and how the diatomic ligands bound to the heme protein interact with nearby residues. An understanding of these protein-ligand interactions within heme proteins is particularly crucial for elucidating their function because much of the biological activities involved with the heme prosthetic group can be modulated through interactions with specific residues in the surrounding environment.

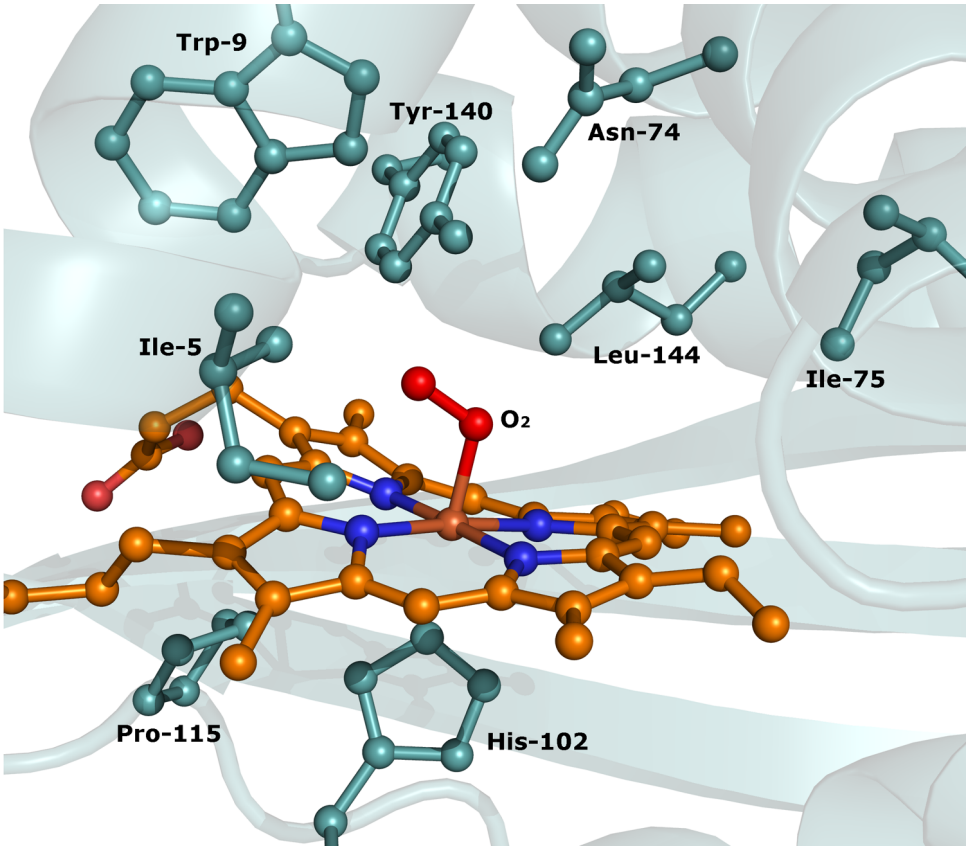

Figure 4.1 Structure of the heme pocket of the *Tt* H-NOX WT O_2 complex. The location of important residues (Ile-5, Trp-9, Ile-75, Pro-115, Tyr-140, and Leu-144) are indicated in the heme pocket. Mutations were made at these positions to either disrupt the H-bonding network or add steric bulk to the heme-binding pocket (adapted from PDB 1U55).

The H-NOX family provides an excellent model from which to work toward understanding ligand discrimination in sGC due to the availability of structural data [5, 42-44] and the fact that this family encompasses both O_2 and non-O_2-binding proteins. A wealth of information has already been acquired to investigate the effects of various distal and proximal pocket mutations on O_2 and NO ligand affinity in *Tt* H-NOX [38, 45, 47]. Figure 4.1 shows the heme pocket of *Tt* H-NOX, highlighting the locations of several important residues. To bring insight into the intermolecular interactions that regulate these properties, we have applied resonance Raman spectroscopy and isotopic substitution to probe the bond energetics and heme conformational changes by site-directed mutagenesis. In this work, we examine several distal pocket properties within *Tt* H-NOX and their effects on the stability of the O_2 complex through the direct measurement of the $\nu(Fe\text{-}O_2)$ and $\nu(O\text{-}O)$ frequencies via resonance Raman spectroscopy. In order to measure $\nu(O\text{-}O)$ for *Tt* H-NOX, a Co^{II}-protoporphyrin IX (PPIX) based derivative was generated using expression methodology developed by Woodward *et al.* [126] since the O-O stretching mode is typically not visible in native

proteins containing Fe^{II}-PPIX. The changes in the vibrational frequencies upon mutation of conserved residues are discussed in the context of how these amino acids form H-bonds with the ligand, and how the stability of the O_2 complex is weakened upon altering these specific interactions within the heme pocket.

4.3 Materials and Methods

4.3.1 Protein expression and purification

Expression and purification of the native Fe^{II} his-tagged (-H_6) *Tt* H-NOX domain were performed as previously described for the original construct [1, 45]. Site-directed mutagenesis was carried out using the QuikChange® protocol (Stratagene), and verified by sequencing (UC Berkeley sequencing core).

The Co^{II}-PPIX substituted *Tt* H-NOX-H_6 were expressed as previously described by Woodward *et al.* using the E. coli RP523 strain [126]. Purification procedures for the Co^{II}-PPIX substituted *Tt* H-NOX were identical to the methods described for the native protein.

4.3.2 Sample preparation

The purified *Tt* H-NOX-H_6 protein was brought into an anaerobic glovebag, and oxidized using ~5-10 mM potassium ferricyanide to remove the bound O_2. The ferricyanide was removed using a PD10 desalting column (Amersham Biosciences) equilibrated with buffer B (50 mM TEA, 50 mM NaCl, pH 7.5). Following oxidation and desalting, the protein was reduced with ~5-20 mM sodium dithionite that was removed using a PD10 desalting column upon complete reduction of the heme. The $^{16}O_2$ complexes were generated by opening the reduced protein to air. To make the $^{18}O_2$ (98% $^{18}O_2$; Cambridge Isotopes) complexes, gas was added to a sealed Reacti-Vial (Pierce) containing Fe^{II}-unligated protein. Final sample concentrations for the Raman experiments were typically 30 to 50 μM. All UV/Vis absorption samples were prepared and measured as previously described [1, 38, 52].

4.3.3 Resonance Raman spectroscopy

All spectra were collected using the 413.1 nm line from a Kr^+ laser (Spectra-Physics model 2025) focused to a beam diameter of ~60 μm with a 50 mm focal-length excitation lens. Raman scattering was detected with a cooled, back-illuminated CCD (LN/CCD-1100/PB; Roper Scientific) controlled by an ST-133 controller coupled to a

subtractive dispersion double spectrograph [95]. The laser power at the sample was ~2 mW, and a microspinning sample cell was used to minimize photolysis. Typical data acquisition times were 60 min. Electronic absorption spectra were obtained before and after the Raman experiments to verify that no photoinduced degradation occurred. Raman spectra were corrected for wavelength dependence of the spectrometer efficiency with a white lamp, and the instrument was calibrated using the Raman frequencies from cyclohexane, CCl_4, and toluene. The reported frequencies are accurate to ±1 cm^{-1}, and the spectral bandpass was set to 8 cm^{-1}. For each Raman spectrum, the raw data were baseline-corrected, and the buffer background signal was subtracted. Spectral analysis and decomposition were performed using Igor Pro (WaveMetrics). Isotopic shifts were approximated on the basis of a simple harmonic oscillator model.

4.4 Results

4.4.1 Electronic absorption spectroscopy

To ensure proper incorporation of the Co^{II}-PPIX into the heme-binding pocket of *Tt* H-NOX, the proteins were examined by UV-vis spectroscopy (Figure 4.2, Table 4.1). Figure 4.2 shows the differences in electronic absorption properties between the native WT *Tt* H-NOX and the Co^{II}-PPIX substituted proteins in the 5-coordinate, fully reduced and 6-coordinate, O_2-bound forms. These changes upon porphyrin substitution are also compared to myoglobin (Mb) for reference (Table 4.1). As previously reported by Karow *et al*. [1], the native WT *Tt* H-NOX protein exhibits a Soret band at 430 nm and a single broad peak centered at 563 nm in the α/β region for the fully reduced, 5-coordinate high spin (5c-hs) species. Upon binding O_2, the Soret shifts to 416 nm and the broad band in the α/β region splits into two distinct peaks at 591 and 556 nm.

As purified, the Co^{II}-PPIX substituted *Tt* H-NOX displays a Soret band at 433 nm, which is characteristic of Co^{III}-PPIX heme proteins. Upon reduction, the Soret shifts from 433 to 406 nm with a broad peak at 560 nm in the α/β region, which is consistent with the observed Soret blue shift to 406 nm in Co^{II}-PPIX Mb. Exposure of the fully reduced 5c-hs Co^{II}-PPIX *Tt* H-NOX to air results in a Soret red shift from 406 to 436 nm upon O_2-binding. This 30 nm shift is larger in *Tt* H-NOX than in the Co^{II}-PPIX substituted Mb, which increases by 20 nm to 426 nm upon O_2-binding. The difference in the extent of Soret shift may reflect differences between the two proteins in their distal and/or proximal pocket interactions with the O_2-bound Co^{II}-PPIX. The α/β band in the *Tt* H-NOX cobalt derivative also shifts from 560 nm to split bands at 581 and 549 nm; by comparison, the Co^{II}-PPIX substituted Mb has split α/β bands centered at 577 and 539 nm.

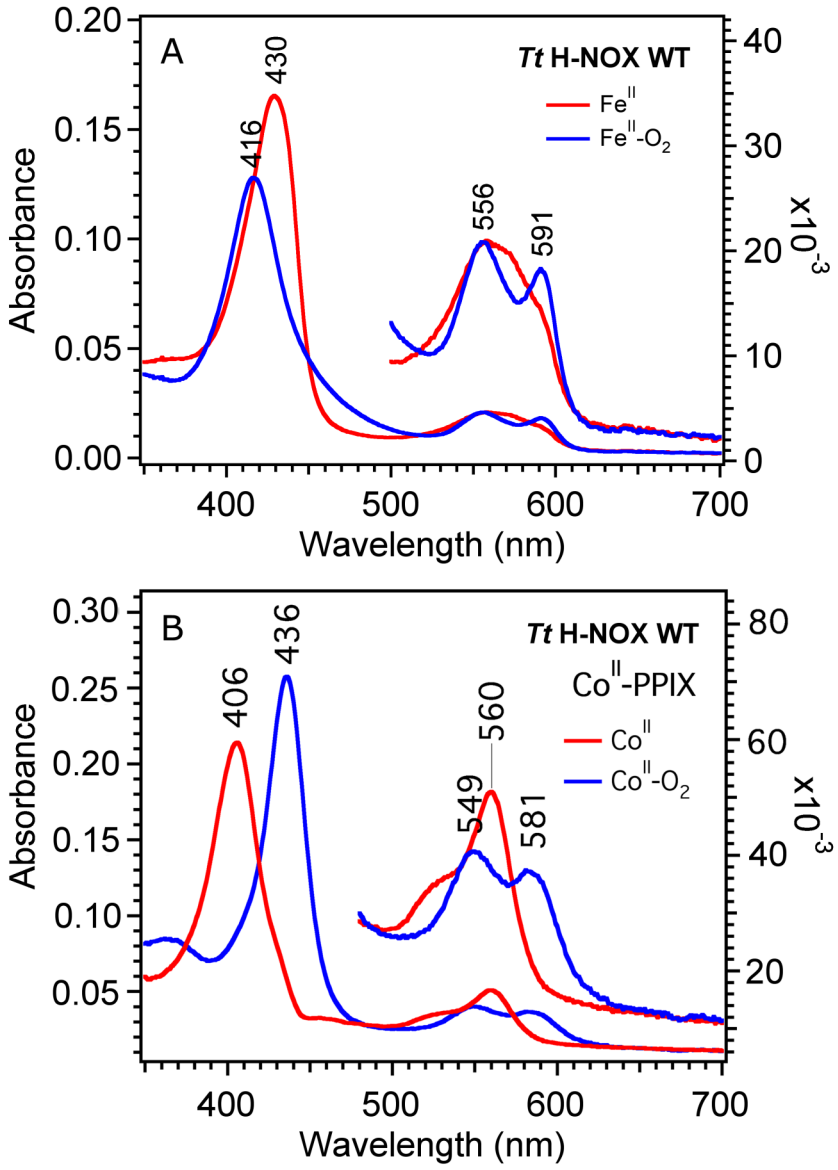

Figure 4.2 Electronic absorption spectra of *Tt* H-NOX. Spectral characteristics of *Tt* H-NOX in its native form (Panel A) are compared to those of the cobalt PPIX substituted protein (Panel B). Traces are shown for the 5-coordinate deoxy (red) and 6-coordinate O_2-bound forms (blue).

Table 4.1 Electronic absorption properties for native WT *Tt* H-NOX and Mb compared to the substituted Co^{II} PPIX proteins. [a]

Protein	Ligand	Soret	α/β	Ref
Tt WT	reduced	430	563	[1]
Tt WT (Co^{II})		406	560	this work
Mb WT		434	556	[99]
Mb WT (Co^{II})		406	556	[127]
Tt WT	O_2	416	591/556	[1]
Tt WT (Co^{II})		436	581/549	this work
Mb WT		418	580/542	[99]
Mb WT (Co^{II})		426	577/539	[127]

[a] All wavelengths are reported in nm.

4.4.2 Resonance Raman spectroscopy

To probe the binding interactions between the O_2-bound heme and protein pocket of *Tt* H-NOX, we investigated the influence of several conserved residues on the properties of the H-NOX domain using site-directed mutagenesis and resonance Raman spectroscopy (Figures 4.3-4.6). Different mutations were generated in the heme pocket to target the hydrogen-bonding network (Trp-9, Tyr-140), and to add steric bulk to the binding pocket (Ile-5, Ile-75, Leu-144). The observed resonance Raman frequencies for the heme skeletal modes and the Fe-O_2 stretching mode are summarized for *Tt* H-NOX WT and these mutants in Table 4.2.

As shown in Figure 4.3 and summarized in Table 4.2, disruption of the hydrogen-bonding network (Trp-9, Tyr-140) in *Tt* H-NOX destabilized the strong electrostatic interaction between the distal Tyr-140 and the O_2 molecule, resulting in the 2-6 cm^{-1} increase in ν(Fe-O_2) from the reported 567 cm^{-1} frequency for the WT protein. Crystallographic studies indicate that Trp-9 is part of a distal H-bonding network with Asn-74 that positions Tyr-140 directly above the axial ligand [5]. Thus, mutation of Trp-9 to phenylalanine produced a modest change in ν(Fe-O_2), upshifting by 2 cm^{-1} to 569 cm^{-1} upon replacement of the indole group with a phenyl ring. The assignment of this band as ν(Fe-O_2) is validated by its downshift to 541 cm^{-1} upon $^{18}O_2$ isotopic substitution, consistent with the 25 cm^{-1} downshift predicted from a simple harmonic oscillator model. Mutation of Tyr-140 resulted in larger ν(Fe-O_2) upshifts to 571 and 573 cm^{-1} as observed in the Y140H and P115A/Y140F spectra, respectively; this larger change is expected due to the disruption of the direct H-bonding interaction of Tyr-140 with O_2. $^{18}O_2$ Isotopic substitution in the *Tt* H-NOX Y140H and P115A/Y140F mutants downshifted ν(Fe-O_2) to 543 and 548 cm^{-1}, respectively, in agreement with calculated shifts. Interestingly, the *Tt* Y140L mutant displayed a 2 cm^{-1} decrease in ν(Fe-O_2) upon abolishing the Tyr-140 hydrogen bond, with a ν(Fe-O_2) of 565 cm^{-1} which downshifts to 538 cm^{-1} for the $^{18}O_2$ complex. This spectrum also displays a reduced ν_8 frequency in

comparison to the other proteins shown in Figure 4.3 (338 cm^{-1}, Y140L versus ~346 cm^{-1}, WT), suggesting that there may be other changes in either the heme deformation or protein environment at the binding site which alter the protein-ligand interactions in the distal pocket. All of the mutants display small frequency shifts of 2-5 cm^{-1} in the heme skeletal modes relative to the WT protein; these may be a result of heme structural rearrangements within the distal pocket to accommodate the substituted amino acids.

To further test the hypothesis that a hydrogen-bonding distal residue was required to reverse the NO/O_2 ligand discrimination in non-O_2-binding H-NOX domains, Phe-142 in the second H-NOX domain from *Legionella pneumophila* (*Lp* H-NOX2) was mutated to tyrosine [38]. Resonance Raman spectra of this mutant were obtained with O_2 isotopic substitution in order to look for direct evidence of an O_2 bond via the Fe-O_2 stretching mode (Figure 4.4). An isotope sensitive band is observed at 563 cm^{-1} in the *Lp* H-NOX2 F142Y resonance Raman spectra, which downshifts to 538 cm^{-1} upon $^{18}O_2$ substitution. This band is assigned as the Fe-O_2 stretching mode based on its observed downshift by 25 cm^{-1}, which agrees well with the harmonic oscillator model. The weak signal for the Fe-O_2 stretching mode is likely due to the presence of a small amount of 5c-hs Fe^{II}-unligated *Lp* H-NOX2 F142Y in the resonance Raman sample; this heterogeneity is reflected in the 1354 cm^{-1} shoulder off of ν_4 (1374 cm^{-1}), in addition to the split skeletal mode frequencies for ν_3 (1505 cm^{-1}) and ν_{10} (1628 cm^{-1}). Relative to the resonance Raman spectra for the WT *Tt* H-NOX O_2 complex, the low frequency region of this *Lp* H-NOX F142Y mutant exhibits very few heme out-of-plane modes suggestive of a less distorted heme structure.

Table 4.2 Observed heme skeletal mode frequencies for 6-coordinate, O_2-bound *Tt* H-NOX and several mutants with native Fe^{II} PPIX as the prosthetic group. [a]

Protein	ν_8	ν_{10}	ν_2	ν_3	ν_4	ν(Fe-O_2)	Ref
Tt H-NOX WT	346	1625	1580	1502	1376	567	[1]
Tt I5A	343	1630	1579	1501	1374	567	this work
Tt I5L	339	1627	1580	1499	1372	562	[51]
Tt I5F	342	1625	1577	1499	1369	562	[128]
Tt W9F	341	1628	1581	1502	1374	569	this work
Tt I75F	339	1625	1578	1498	1373	563	this work
Tt P115A	349	1633	1583	1505	1378	565	[51]
Tt I5L/P115A	342	1630	1582	1502	1375	562	[51]
Tt Y140F	344	1621	1580	1496	1370	nd [b]	this work
Tt P115A/Y140F	347	1630	1580	1502	1375	573	this work
Tt Y140H	346	1624	1579	1498	1374	571	this work
Tt Y140L	338	1626	1578	1497	1372	565	this work
Tt L144F	339	1623	1578	1500	1373	563	this work

[a] All vibrational frequencies are reported in cm^{-1}.
[b] nd = not determined.

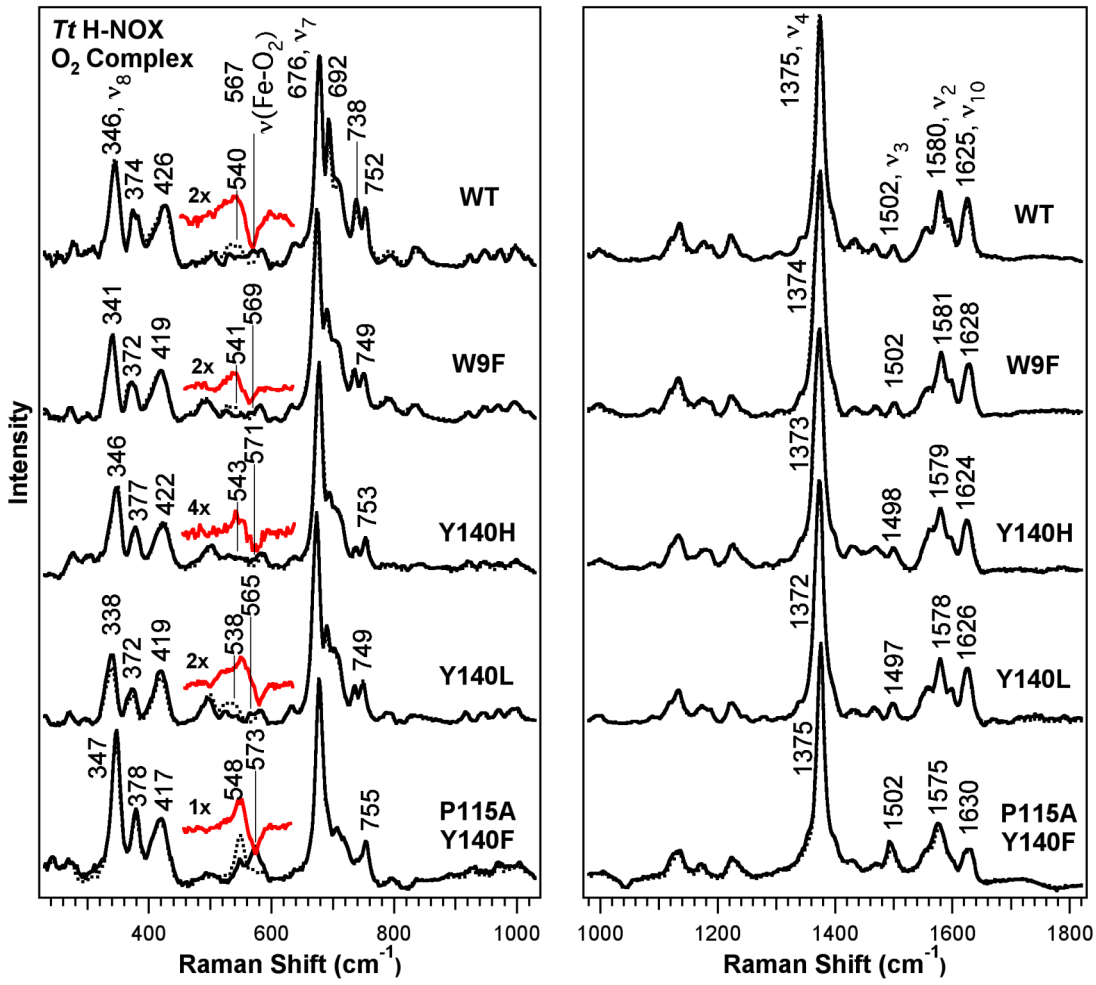

Figure 4.3 Resonance Raman spectra of the O_2 complexes of *Tt* H-NOX WT and various distal pocket mutants. $^{18}O_2$ spectra (dotted line) are overlapped with the $^{16}O_2$ spectra to indicate the frequency shifts upon isotopic substitution, and the difference ($^{18}O_2 - {}^{16}O_2$) spectra are shown below each protein for clarity. Spectral intensities were normalized to ν_7 and ν_4 for the low and high frequency regions, respectively.

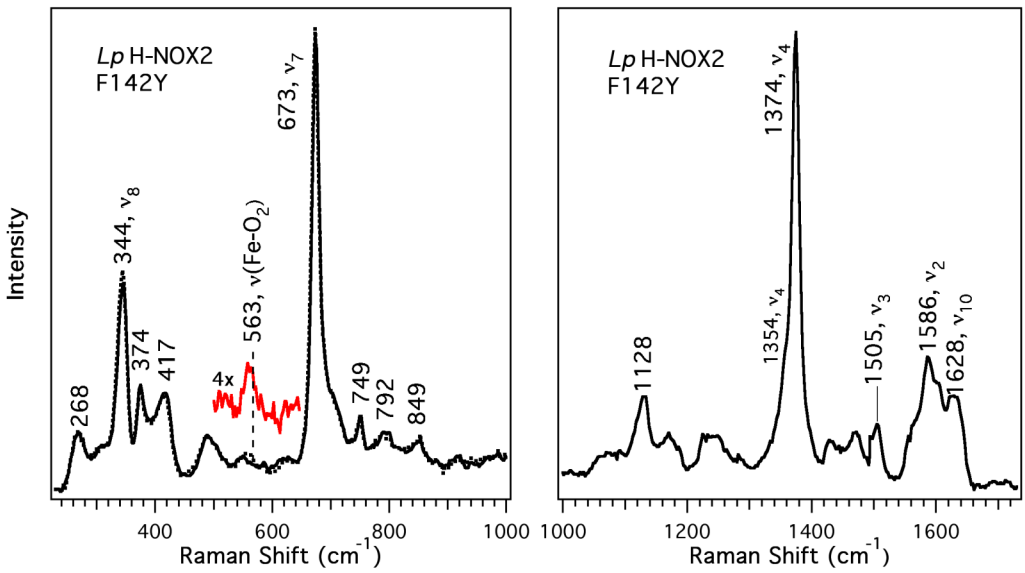

Figure 4.4 Resonance Raman spectra of the *Lp* H-NOX2 F142Y mutant. Addition of tyrosine at the Phe-142 position allows the F142Y mutant to weakly bind O_2, unlike the *Lp* H-NOX2 WT protein. The $^{18}O_2$ spectrum (dotted line) is overlapped with the $^{16}O_2$ spectrum to indicate the frequency shifts upon isotopic substitution, and the difference ($^{18}O_2 - {}^{16}O_2$) spectrum is shown at a 4-fold magnification for clarity. Spectral intensities were normalized to ν_7 and ν_4 for the low and high frequency regions, respectively.

Another subgroup of *Tt* H-NOX mutants involved altering the distal and proximal cavities to either reduce or increase steric bulk by targeting the Ile-5, Ile-75, Pro-115 and Leu-144 residues [45, 128]. Figure 4.5 compares the RR spectra of O_2-bound *Tt* H-NOX I5F, I75F, and L144F with the WT protein, and the skeletal vibrations for these proteins and other mutants are summarized in Table 4.2. The changes in the RR features for the *Tt* H-NOX I5L, P115A, and I5L/P115A mutants have already been previously presented and discussed [51]. As shown in Figure 4.5, the Fe-O_2 stretching frequency decreased by 5-6 cm^{-1} as steric bulk was added to the distal pocket of *Tt* H-NOX with the replacement of smaller nonpolar residues with phenylalanine. The I5F mutant displays a band at 562 cm^{-1} which downshifted by 25 cm^{-1} to 537 cm^{-1} upon $^{18}O_2$ isotopic substitution. Similarly, the I75F and L144F exhibited 25 cm^{-1} downshifts from 563 cm^{-1} to 538 cm^{-1} for $^{16}O_2 \rightarrow {}^{18}O_2$. Furthermore, heme out-of-plane (oop) modes (*i.e.* γ_{15} ~ 691 cm^{-1}, γ_{11} ~ 704 cm^{-1}, γ_5 ~737 cm^{-1}) in the low frequency region show substantial decreases in RR intensity upon mutation. These low frequency modes correspond to heme deformations and reflect changes in the heme conformation for the mutants relative to the WT protein [51, 56]. Striking changes are also observed in the high frequency region where the main heme skeletal modes (*i.e.* ν_4 ~1375 cm^{-1}, ν_3 ~1500 cm^{-1}, ν_2 ~1580 cm^{-1}, ν_{10} ~ 1625 cm^{-1}) occur. Compared to the WT protein, all three mutants display significantly broadened skeletal marker bands with minor shifts in vibrational frequency. In contrast, the *Tt* H-NOX I5A mutation produced minimal changes in vibrational frequency in comparison to the WT protein (Table 4.2).

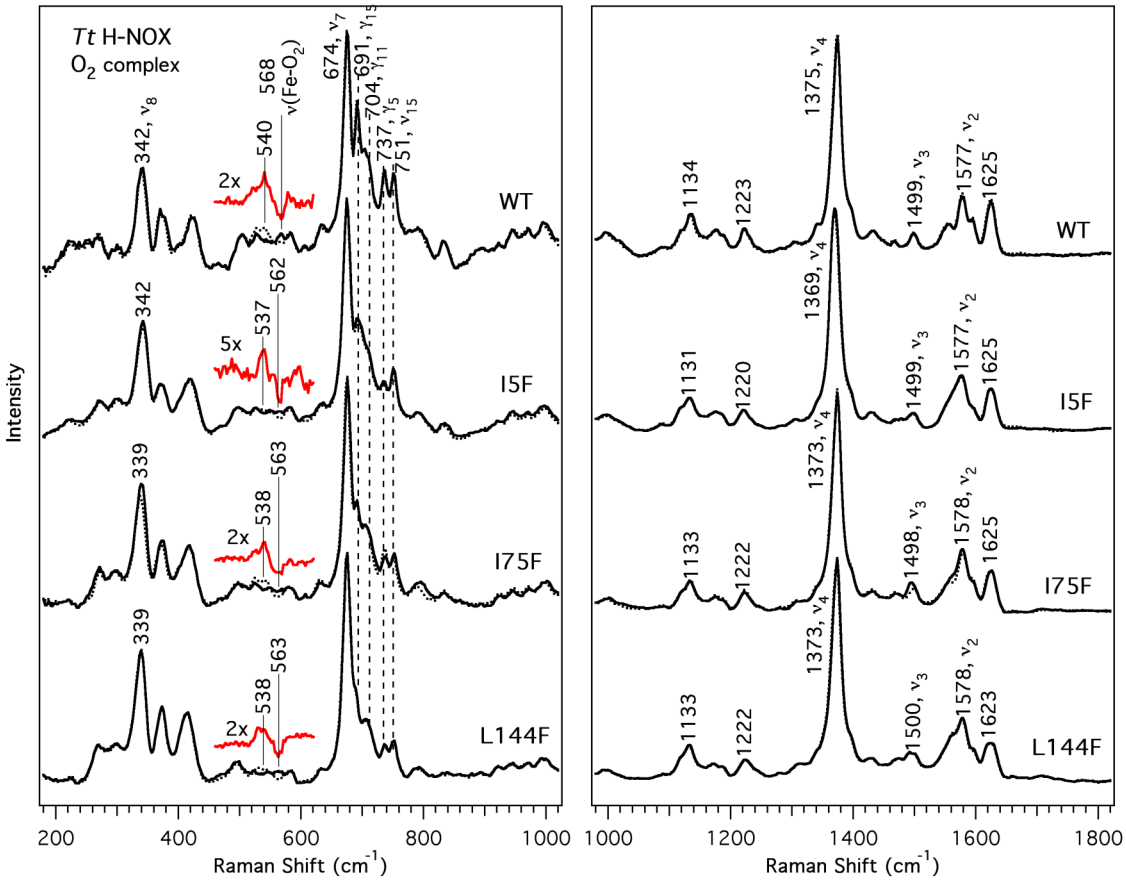

Figure 4.5 Resonance Raman spectra of the O_2 complexes of *Tt* H-NOX WT, I5F, I75F, and L144F. $^{18}O_2$ spectra (dotted line) are overlapped with the $^{16}O_2$ spectra to indicate the frequency shifts upon isotopic substitution, and the difference ($^{18}O_2 - {}^{16}O_2$) spectra are shown below each protein for clarity. Spectral intensities were normalized to ν_7 and ν_4 for the low and high frequency regions, respectively.

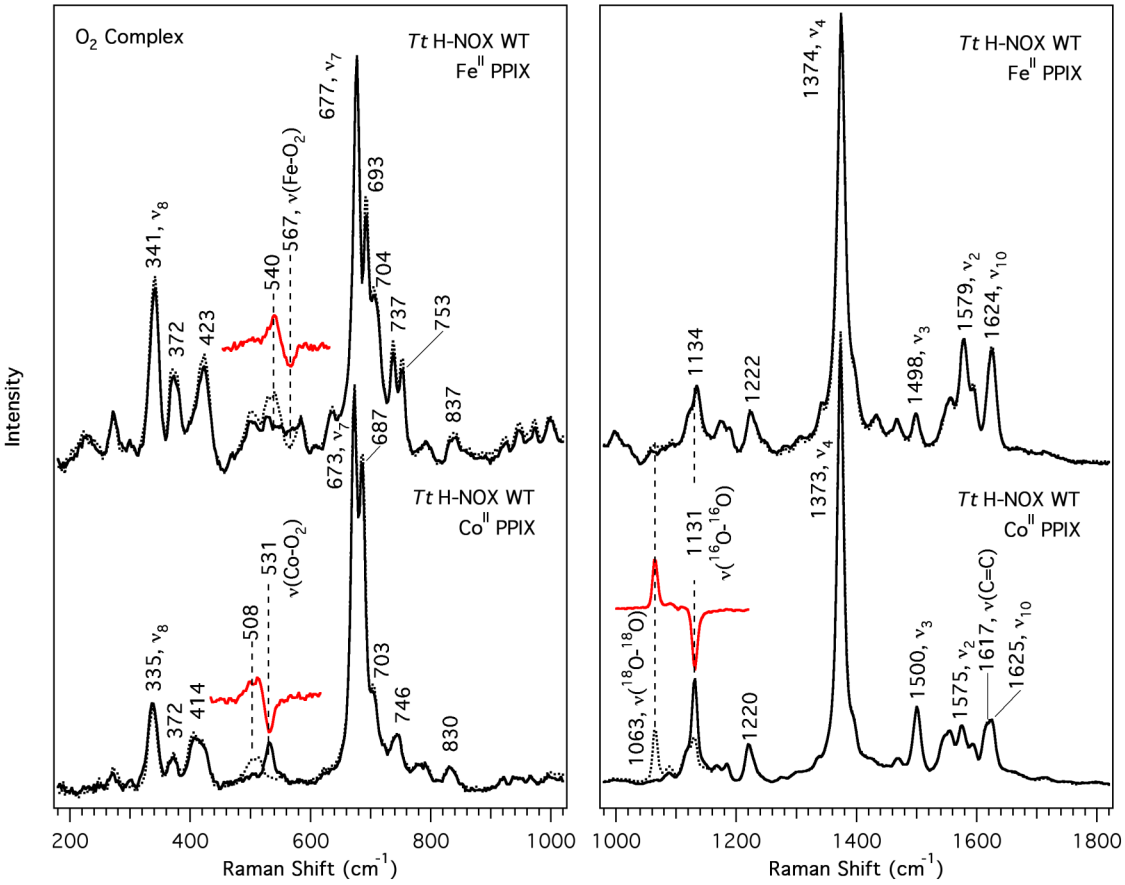

Figure 4.6 Resonance Raman spectra of the O_2-bound native WT *Tt* H-NOX protein in comparison to the cobalt PPIX-substituted WT *Tt* H-NOX protein. The $^{18}O_2$ spectra (dotted line) are overlapped with the $^{16}O_2$ spectra to indicate the frequency shifts upon isotopic substitution, and the difference ($^{18}O_2 - {}^{16}O_2$) spectra are shown for clarity. Spectral intensities were normalized to ν_7 and ν_4 for the low and high frequency regions, respectively.

Upon characterization of the native *Tt* H-NOX domain and various mutants thought to influence the O_2-binding properties of this protein, we wanted to elucidate the chemical nature of the Fe-O_2 bond in *Tt* H-NOX. In order to do this, resonance Raman spectra of the native protein and its Co^{II}-PPIX derivative were obtained (Figure 4.6). The skeletal frequencies, ν(Co-O_2) and ν(O-O) for the Co^{II}-PPIX substituted *Tt* H-NOX WT and mutants are summarized in Table 4.3. In addition, the vibrational frequencies for the Co-O_2 and O-O stretching modes of hemoglobin (Hb) and Mb are provided for reference. $^{18}O_2$ isotopic substitution indicates that the Fe-O_2 and Co-O_2 stretching frequencies occur at 567 and 531 cm^{-1}, respectively; these assignments are based on their downshifts to 540 and 508 cm^{-1}. In addition, the O-O stretching mode is observed at 1131-1134 cm^{-1} in the Co^{II}-PPIX substituted *Tt* H-NOX spectra, downshifting by ~68 cm^{-1} to 1063 cm^{-1} for the $^{18}O_2$ complex. This agrees relatively well with the predicted 65 cm^{-1} downshift for an isolated O-O bond.

Table 4.3 Observed heme skeletal mode frequencies for the 6-coordinate, O_2-bound *Tt* H-NOX and several mutants with substituted Co^{II} PPIX as the prosthetic group.

Protein (CoPPIX)	ν_8	ν_{10}	ν_2	ν_3	ν_4	ν(Co-O_2)	ν(O-O)	Ref
Tt WT recon. [b]	346	1630	1580	1504	1377	534	1134	this work
Tt WT exp. [c]	335	1625	1575	1500	1373	531	1131	this work
Tt P115A exp.	341	1627	1580	1505	1376	528	1131	this work
Tt Y140L exp.	342	1632	1585	1507	1377	521	1137	this work
Hb	nr [d]	nr	nr	nr	nr	537	1122, 1153	[66]
Mb	nr	nr	nr	nr	nr	539	1136	[129]

[a] All vibrational frequencies are reported in cm^{-1}.
[b] recon. = protein reconstitution with Co^{III} PPIX via Teale's Method [130].
[c] exp. = protein expression with Co^{III} PPIX as described by Woodward *et al*. [126].
[d] nr = not reported.

We found subtle differences in frequency and intensity between the resonance Raman spectra of the Co^{II}-PPIX substituted *Tt* H-NOX WT protein depending on the procedure used to perform the Co^{II}-PPIX incorporation (*i.e.* reconstitution via Teale's Method versus protein expression using *E. coli* RP523 heme uptake strain) [126, 130]. Teale's Method did not properly substitute Co^{II}-PPIX in the *Tt* H-NOX mutants, so these proteins had to be expressed using the heme uptake method by Woodward *et al*. Mutation of the distal Tyr-140 and proximal Pro-115 produced small changes in vibrational frequency in the skeletal modes, as well as the O_2-associated modes, and are summarized in Table 4.3. In comparison to the WT Co^{II}-PPIX substituted protein, the Co^{II}-PPIX mutants showed downshifts in ν(Co-O_2) by 3-6 cm^{-1} and upshifts in ν(O-O) to 1137 cm^{-1} (*Tt* H-NOX Co^{II}-PPIX Y140L). In addition, ν_8 displayed 6-10 cm^{-1} upshifts for the mutants relative to the expressed Co^{II}-PPIX substituted WT protein (ν_8 ~ 335 cm^{-1}).

4.5 Discussion

Although both native and Co^{II}-PPIX substituted globins and model compounds have been extensively studied by resonance Raman spectroscopy and other methods [66, 74, 82, 125, 131, 132], the H-NOX domains are still a relatively new class of heme proteins, with significantly less spectroscopic information available to aid in the understanding of observed O_2 kinetic measurements. Through a more comprehensive knowledge of the mechanism by which the protein pocket tunes the ligand binding in these proteins, we hope to better understand how they discriminate between NO and O_2 in the H-NOX family. In this paper, we present our main findings that: (i) the vibrational shifts in the ν(Fe-O_2) frequency upon mutation of Trp-9 and Tyr-140 indicate the presence of important hydrogen-bonding interactions which stabilize the O_2

complex, (ii) the addition of steric bulk via site-directed mutagenesis to the heme pocket of *Tt* H-NOX forces the domain into a more open conformation which causes the Fe-O_2 bond to lengthen upon increased separation between the Tyr-140 residue and O_2 ligand, and (iii) the ν(O-O) frequency for *Tt* H-NOX is ~1131-1134 cm^{-1}, which suggests a formalized designation of Fe^{III}-O_2^- rather than Fe^{II}-O_2 for the *Tt* H-NOX O_2 complex.

We now provide a detailed interpretation of the vibrational frequency and intensity shifts observed in the RR spectra of the O2-bound H-NOX domains, and discuss what these changes indicate regarding the possible electrostatic protein-ligand interactions and/or heme conformational changes occurring in solution within this family. Specifically, the elimination of these important intermolecular interactions alters the ability of *Tt* H-NOX to bind O_2 tightly, as reflected by the shifts in ν(Fe-O_2) and ν(O-O) frequencies. By combining our RR results with the available NMR and X-ray crystallographic data on the H-NOX family [5, 42-44, 46], we can obtain a more complete understanding of the dynamic heme conformation and its interactions with the H-NOX protein environment.

4.5.1 Distal effects on O_2 bonding in *Tt* H-NOX

Figure 4.1 indicates that Trp-9, Asn-74, and Tyr-140 form the tightly held H-bonding network in the distal pocket. Based on the crystal structure of the O_2 complex [5], Asn-74 and Trp-9 are located ~2.9 Å and ~2.7 Å away from the phenolic oxygen in Tyr-140. In addition, Tyr-140 is located ~2.8 Å away from O_2, and points directly at the ligand. Our resonance Raman spectra of the *Tt* H-NOX O_2 complex exhibit upshifts in the Fe-O_2 stretching mode upon mutating either Trp-9 or Tyr-140, indicative of disrupted H-bonds between the O_2 complex and these residues. Upon loss of this electrostatic interaction between the complex and the distal residue, the withdrawn electron density from the H-bond is donated back into the Fe-O_2 bond and increases the ν(Fe-O_2) frequency although a distal residue is still in place to trap the O_2 within the pocket. Similar increases in ν(Fe-O_2) have been observed in other heme proteins when the H-bond was weakened by site-directed mutagenesis in the distal pocket [66]. In particular, the *Tt* H-NOX W9F mutant displays a much more modest ν(Fe-O_2) vibrational shift [$\Delta\nu$ = +2 cm^{-1} relative to WT] in comparison to the Y140H [$\Delta\nu$ = +4 cm^{-1}] and P115A/Y140F [$\Delta\nu$ = +6 cm^{-1}] mutants; these shifts are reflective of the stronger, more direct electrostatic contact between Tyr-140 and O_2. The fact that ν(Fe-O_2) increases upon loss of the H-bond also suggests that Tyr-140 interacts more strongly with the proximal oxygen atom (that is closer to iron) than the terminal oxygen in O_2. Our results showing the weakened H-bonding contacts in the *Tt* H-NOX mutants agree with the kinetic studies by Boon *et al*., which demonstrated up to a 20-fold change in the O_2 dissociation rate upon removal of Tyr-140 (*i.e. Tt* H-NOX WT, O_2 k_{off} ~ 1.22 ± 0.09 s^{-1} versus *Tt* H-NOX Y140L, O_2 k_{off} ~ 20.1±2.0 s^{-1}) [38]. In contrast, the O_2 k_{off} rate for the *Tt* H-NOX W9F mutant showed a modest change (Δk_{off} = +0.6 s^{-1} relative to WT) [38], which is consistent with our smaller ν(Fe-O_2) frequency shift in the resonance Raman spectra for this mutant. Together, these results demonstrate that the stability of the O_2

complex in *Tt* H-NOX is compromised upon disruption of the Tyr-140 hydrogen bond that traps the diatomic ligand in place.

In contrast to the other distal pocket mutants, *Tt* H-NOX Y140L displayed a $\nu(Fe\text{-}O_2)$ downshift of 2 cm^{-1} relative to the WT protein. Although the downshift does indicate a longer $Fe\text{-}O_2$ bond length (and consequently, a smaller force constant) for the *Tt* H-NOX Y140L protein relative to WT, this observation initially seems to counter the previous observed trends of an increased $\nu(Fe\text{-}O_2)$ frequency upon loss of the hydrogen-bonding Tyr-140 in *Tt* H-NOX. However, the observed vibrational frequency shifts of other modes in the resonance Raman spectra of this mutant indicate that there may be additional rearrangements within the heme-binding pocket which alter other interactions between the heme and nearby residues. The low frequency region exhibits downshifts for ν_8 (*Tt* Y140L ~ 338 cm^{-1}; *Tt* WT ~ 346 cm^{-1}) and other modes at 372 and 419 cm^{-1} that are associated with the heme substituent groups. These 7-8 cm^{-1} downshifts indicate changes in the heme pocket interactions upon mutation. In addition, the high frequency region displays changes in the skeletal mode frequencies, which further support differences in the heme electronics and electrostatic interactions with the surrounding protein pocket. The measured O_2 off-rate for the *Tt* H-NOX Y140L mutant is 20-fold faster than the WT protein, which agrees well with our observations of a weaker $Fe\text{-}O_2$ bond. Previous resonance Raman investigations on the *Tt* H-NOX proteins studying the influence of the Tyr-Ser-Arg (YxSxR) motif indicate that the electrostatic contacts between these residues and the heme propionate groups can greatly influence the metal-ligand bonding interactions [133]. Thus, it is possible that in *Tt* H-NOX Y140L, interactions such as that between the heme substituents and the YxSxR motif have been compromised upon mutation and structural rearrangement, resulting in other effects on the vibrational frequency that counter the initial increase in $\nu(Fe\text{-}O_2)$ upon removal of the H-bonding Tyr-140.

The importance of a distal pocket H-bonding residue for stabilizing the O_2 complex has been widely known for the globins, and this is also true for the H-NOX family. Boon *et al*. replaced the distal Phe-142 in the non-O_2-binding *Lp* H-NOX2 with a tyrosine residue to mimic the Tyr-140 in the O_2-binding *Tt* H-NOX domain. Upon exposure to air, the *Lp* H-NOX2 F142Y protein displayed a Soret band centered at 417 nm and split α/β bands, which differs from the WT protein with a 428 nm Soret band and a single broad α/β band in the 500-600 nm region [38]. In addition to the exhibited isotopic shift patterns, the heme skeletal frequencies of this *Lp* H-NOX2 F142Y mutant also support the presence of a 6-coordinate, low-spin, O_2-bound heme protein based on its similarity to other O_2-bound heme proteins. The difference in the $\nu(Fe\text{-}O_2)$ stretching frequency between the *Lp* H-NOX2 F142Y mutant and *Tt* H-NOX WT protein is likely a reflection of differences in interaction between the O_2 ligand and the other residues lining the protein pocket. The lower $\nu(Fe\text{-}O_2)$ for *Lp* H-NOX2 F142Y can be attributed to a longer $Fe\text{-}O_2$ bond length, resulting in a smaller force constant and stretching frequency [134]. Thus, despite the presence of a hydrogen bonding tyrosine residue in the distal pocket of *Lp* H-NOX2 F142Y, the O_2 is not held tightly in place, but is trapped just enough to form a bond with the iron metal. It is plausible that a stronger $Fe\text{-}O_2$ bond could be formed in *Lp* H-NOX2 if additional hydrogen bonding

residues, such as those observed in the distal pocket of *Tt* H-NOX, are added to incorporate a network that would not only trap the O_2, but keep it stabilized by properly orientating the Tyr-142 in place to optimize electrostatic contacts. In addition, the ν(Fe-His) for *Lp* H-NOX2 WT is 214 cm^{-1} (Appendix, Table 1A) [133], and is weaker in comparison to *Tt* H-NOX (218 cm^{-1}) and the globins (~220 cm^{-1}) [1, 63]. Mutations that would strengthen the Fe-His bond, such as the Pro-115 mutation in *Tt* H-NOX [51], may also help support a tighter O_2 affinity in *Lp* H-NOX2.

4.5.2 Steric bulk effects on O_2 binding in *Tt* H-NOX

Of the key residues, Ile-5, Ile-75, Pro-115, and Leu-144, all but Pro-115 are located in the distal pocket, and previous work suggested that these residues influence the heme conformation [1, 5, 42, 44, 45, 51, 128]. Our resonance Raman spectra reveal downshifts of 5-6 cm^{-1} in the ν(Fe-O_2) frequency relative to *Tt* H-NOX WT when phenylalanine is introduced in the distal pocket at the Ile-5, Ile-75, and Leu-144 positions. By application of Badger's Rule [134], the decrease in vibrational frequency indicates that the Fe-O_2 bond has lengthened as a result of the distal pocket mutation; this suggests that the distal hydrogen-bonding network are displaced away from O_2 such that they no longer trap it in place above the heme. Weinert *et al*. have previously characterized the kinetic influence of steric bulk at these positions on the ligand binding affinity in *Tt* H-NOX [45]. Addition of phenylalanine at the Ile-75 and Leu-144 positions each increased the k_{off} rate by 11- and 16-fold, respectively, in comparison to the WT protein (k_{off} = 1.20±0.02 s^{-1}). Based on our resonance Raman spectra and the O_2 kinetics from Weinert *et al*., it appears that the steric phenyl group from the substituted phenylalanine causes structural rearrangements in the distal pocket such that the H-NOX domain occupies a more open conformation. This 'open' form would then trap O_2 within the distal pocket less efficiently, especially if Tyr-140 is located farther away so that it cannot form the electrostatic contacts necessary to stabilize the O_2 complex. As a result, the Fe-O_2 bond should lengthen relative to the WT protein without the Tyr-140 in place due to the 'open' H-NOX conformation, which is reflected in the resonance Raman spectra. The plausibility of these explanations for the observed ν(Fe-O_2) frequency downshift are further supported by the crystal structure of the *Tt* H-NOX I75F/L144F mutant, which indicates that the H-NOX domain does assume a more elongated and open structure in order to accommodate the bulky phenyl groups occupying the back of the distal pocket [45].

In addition to the ν(Fe-O_2) downshift observed for the I5F, I75F, and L144F mutants, the resonance Raman spectra for these mutants display decreased intensities in the heme out-of-plane (oop) modes in the low frequency region relative to the WT protein. Dramatic changes are also exhibited in the high frequency region, where the mutants all display largely broadened heme skeletal bands in contrast to *Tt* H-NOX WT. These observations correspond well with our description of the H-NOX domain assuming a more open conformation upon mutation. With more space in the distal pocket, the heme can adopt a more relaxed conformation relative to the largely distorted WT heme

structure; this relaxation is demonstrated by the loss of Raman intensity in the low frequency oop modes (*i.e.* γ_{15}, γ_{11}, γ_5) as previously discussed for the P115A mutant [51]. The increased flexibility and more dynamic nature of the heme chromophore upon opening the H-NOX pocket is further supported by the large broadening of the skeletal mode bands in the 1550-1650 cm^{-1} region. These bands correspond to C_α-C_m, C_β-C_β, and C=C stretching modes associated with the porphyrin ring and appear more distinct in the resonance Raman spectra of the WT protein in comparison to the three bulky mutants.

4.5.3 Chemical nature and stability of the Fe-O_2 bond in *Tt* H-NOX.

Despite the fact that a designated formal description of the Fe-O_2 bond in a heme protein rarely matches the actual measured or calculated electron distributions, it can be very useful toward rationalizing the chemical or physical properties of the complex [125]. In the case of *Tt* H-NOX, this can contribute toward a better understanding of the Fe-O_2 bond with the availability of both spectroscopic, kinetic and crystallographic data [5]. Boon *et al*. speculated that the electronic structure of the *Tt* H-NOX O_2 complex was a resonance mixture between Fe^{II}-O_2 and Fe^{III}-O_2^- (*i.e.* $[FeO_2]^8$ system) based on observed kinetics, O_2-rebinding abilities, and wavelength shifts in the electronic absorption spectra [38]. We can now use resonance Raman spectroscopy to measure both the ν(Fe-O_2) and ν(O-O), and directly probe the nature of this bond in *Tt* H-NOX.

Although Das *et al*. reportedly observed both the ν(Fe-O_2) and ν(O-O) simultaneously in their resonance Raman spectra of hemoglobins from *Chlamydomonas eugametos* and *Synechocystis* PCC6803 [66], the ν(O-O) band is typically RR silent for most heme proteins and requires the substitution of the Fe^{II}-PPIX with Co^{II}-PPIX. Upon replacement of the heme iron with cobalt, it is thought that a charge transfer (CT) transition from $\pi^*(\pi_g^*O_2/d_{xz})$ to $\sigma^*(d_z^2/Co/\pi_g^*)$ sufficiently overlaps with the intense Soret band from the porphyrin, allowing for enhancement of the ν(O-O) band [82]. Crystallographic studies by Brucker *et al*. also indicate that Co^{II}-PPIX substitution does not significantly alter the protein fold, as the Co^{II}-PPIX derivative of Mb was found to closely resemble native Mb [131]. However, the O_2 affinity decreases by 50 to 100-fold upon Co^{II}-PPIX substitution in the globins [132], and a decreased affinity for O_2 was similarly observed in our *Tt* H-NOX derivative.

In the *Tt* H-NOX resonance Raman spectra for both the native and Co^{II}-PPIX derivative, we see a decrease in the metal-O_2 stretching mode from iron (567 cm^{-1}) to cobalt (531 cm^{-1}). This downshift is attributed to the extra electron in the $\pi^*(\pi_g^*/d_\pi)$ antibonding molecular orbital that is mainly localized on O_2 in the Co-O_2 complex [74]. In comparison to iron, the greater nuclear charge in cobalt contracts and lowers the d-orbital energy, which results in a weaker d_π/π_g^* interaction and lower vibrational frequency for ν(Co-O_2). The *Tt* H-NOX cobalt derivative also exhibits an $^{18}O_2$ isotope-sensitive band at 1131 cm^{-1}, which downshifts to 1063 cm^{-1}, that we attribute to ν(O-O).

By comparison, the ν(O-O) frequency is 1556 and 1100-1150 cm^{-1} for O_2 gas and O_2^-, respectively [66]. Despite the fact that the ν(O-O) stretching frequency in *Tt* H-NOX is very similar to that of the free superoxide ion, it is unlikely that there is a full transfer of one electron from the iron to the O_2 ligand given the observed rebinding kinetics by Boon *et al*. on *Tt* H-NOX [38]. From the 1.77 Å resolution *Tt* H-NOX crystal structure, the O-O bond length is ~1.30 Å [5], which is between the bond distances for O_2 and O_2^-. Figure 4.7 shows the ν(Fe-O_2)/ν(O-O) correlations plot for the *Tt* H-NOX domains, the globins, 5- and 6-coordinate synthetic heme models, and the thiolate-ligated P450s. This plot provides a way for determining the sensitivity of these modes to the heme environment in these different proteins. Although the O_2 complex assumes a bent configuration in the heme pocket, backbonding influences are still important due to the presence of an empty π^* orbital that lies perpendicular to the Fe-O_2 bending plane [116]. The effects of metal-to-ligand backbonding can be readily observed from the negative ν(Fe-O_2)/ν(O-O) slope. As shown in Figure 4.7, the ν(Fe-O_2)/ν(O-O) correlation for *Tt* H-NOX resembles the 6-coordinate globins, and is reflective of their similarities in both the extent of metal-to-ligand backdonation and ferric superoxide-like character.

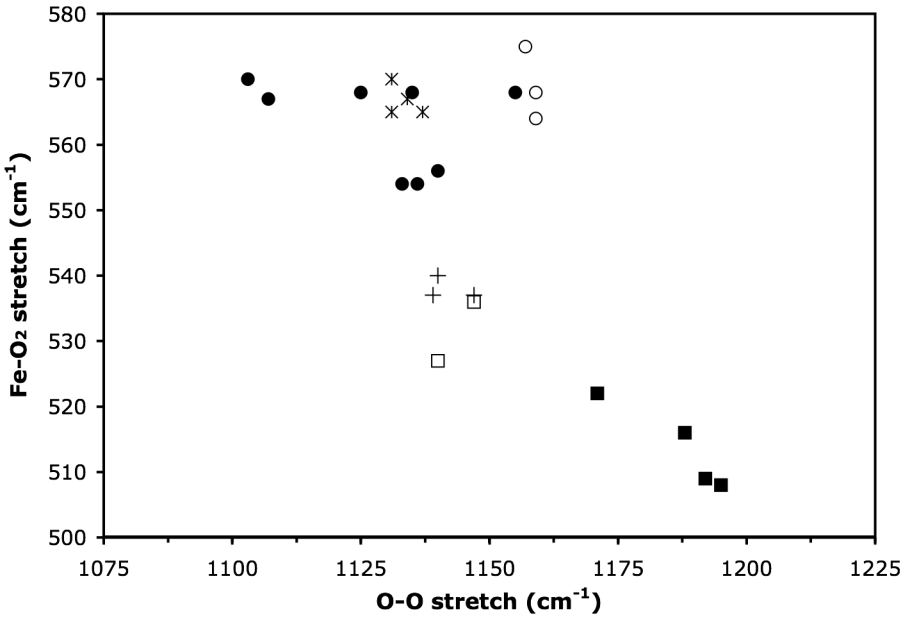

Figure 4.7 Correlation plot between ν(Fe-O_2) and ν(O-O) for different heme proteins indicating modest backbonding effects. The O_2-bound heme proteins (histidyl-ligated unless otherwise noted) and their corresponding symbols are as follows: globins (●); 6-coordinate synthetic heme models (○); 5-coordinate synthetic heme models (■); thiolate-ligated 6-coordinate synthetic models (□); thiolate-ligated P450s (+); *Tt* H-NOX (×).

In summary, the weakening of the distal H-bonding network in *Tt* H-NOX upon mutation of Trp-9 and Tyr-140 in *Tt* H-NOX is supported in our RR spectra by the

observed upshift of ν(Fe-O_2) and by the increased O_2 off-rates of up to 20-fold observed for these proteins. Interestingly, the addition of steric bulk to the distal pocket of *Tt* H-NOX caused the Fe-O_2 stretching frequency to decrease. The decreased frequency is indicative of a longer Fe-O_2 bond, which may be due to the bulky residues forcing the H-NOX domain into a more 'open' conformation that separates Tyr-140 and O_2 such that the diatomic ligand is no longer as effectively trapped in the distal pocket. This structural rearrangement plausibly disrupts the H-bond stabilization network involving Trp-9, Asn-74, and Tyr-140. Our explanation is also supported by the measured O_2 off-rates for the I75F and L144F, which were significantly faster than for the WT protein. Thus, it appears that there are two separate factors that can influence the ν(Fe-O_2) frequency and O_2 stability in *Tt* H-NOX. One involves the abolished H-bond with O_2, which produces a ν(Fe-O_2) upshift upon restoration of the withdrawn electron density to the Fe-O_2 bond. Here, the predominant effect is from the lost H-bond; O_2 is still trapped in the distal pocket with a similar Fe-O_2 internuclear distance to WT. In the second case, as observed for the steric bulk mutants, the Fe-O_2 stretching frequency decreases upon mutation so the internuclear distances between iron and O_2 increases much more relative to the WT protein. Since the Tyr-140 can no longer trap the O_2 ligand in place in the 'open' H-NOX conformation, the previously observed H-bond influence has little effect on the Fe-O_2 stretching frequency and the dominant factor becomes the larger bond distance from the more loosely held O_2 ligand. These insights into how the surrounding distal residues differentially influence the ν(Fe-O_2) may help to elucidate its ligand binding properties and, ultimately, the ligand specificity exhibited within the H-NOX family.

4.6 Acknowledgements

We thank members of the Marletta and Mathies laboratories for their helpful discussions and critical input. Drs. Emily E. Weinert and Elizabeth M. Boon are gratefully acknowledged as collaborators in this project, and for their assistance with sample preparation. This work was supported in part by the Mathies Royalty Fund and NIH Grant GM070671 (M.A.M.).

Chapter 5

Conclusions and Prospects

Through the application of resonance Raman (RR) spectroscopy and site-directed mutagenesis in *Tt* H-NOX, this dissertation has provided a better understanding of the mechanisms by which the H-NOX domain selectively binds its target molecule, and elucidated the heme conformational changes associated with ligand binding. This final chapter summarizes the contributions made in this dissertation, and gives recommendations for future areas of investigation.

5.1 Probing the H-NOX Heme Pocket with RR Spectroscopy

In Chapter 2, the role of conserved residues, Ile-5 and Pro-115, in modulating the heme conformation of *Tt* H-NOX was investigated via RR spectroscopy. Interpretation of the heme skeletal mode frequency shifts and intensity changes in the heme out-of-plane modes indicated that the single P115A mutation is most influential in significantly relaxing the O_2-bound heme from its native distorted conformer. In contrast, the conservative I5L mutation more closely resembled the WT protein, and the RR spectra of the I5L/P115A double mutant suggested that its effects on the heme resembled an admixture of the two individual mutations rather than a synergistic combination. Based on these results and recent structural characterization of the H-NOX domain [5, 42-44], we concluded that the strictly conserved Pro-115 residue plays a role in maintaining the heme conformation by serving as a hinging point between the distal and proximal subdomains. Upon mutating Pro-115 to alanine, the *Tt* H-NOX domain no longer holds the heme in a rigid and distorted conformation, resulting in its sampling of multiple conformations that are significantly relaxed with respect to the WT protein.

Chapter 3 describes the use of RR spectroscopy to probe the *Tt* H-NOX heme pocket, examining the basis for the unusually high C-O stretching frequency that is ubiquitous throughout the H-NOX family. To investigate the potential protein-ligand interactions responsible for the high ν(C-O), mutations were generated to perturb specific regions in *Tt* H-NOX, including: (i) the distal H-bonding network, (ii) the conserved YxSxR motif, (iii) the Fe-His linkage, and (iv) residues contributing toward the heme deformation. Our resonance Raman spectra demonstrated that strong

electrostatic interactions between the heme and the surrounding protein pocket residues increase the backdonation of the Fe^{II} d_π electrons into the CO π^* orbitals, contributing to the unusually high C-O stretching frequency in the H-NOX domains. With the exception of the heme deformation, all other attributes in *Tt* H-NOX showed varying effects on the ν(Fe-CO) and ν(C-O) frequencies upon mutation. The most dramatic change was observed upon disrupting the H-bonding interactions between the YxSxR motif and the heme propionate groups, with ν(C-O) frequency downshifts of up to ~70 cm^{-1}. In addition, these YxSxR mutants displayed two dominant CO conformers, one of which was spectroscopically similar to the WT protein. The presence of these two CO conformers suggests that the heme undergoes a fluctuating swivel motion upon destabilization of the H-bonds between the YxSxR residues and the heme propionate groups. One conformer maintained protein-ligand contacts that are remarkably similar to the WT protein and shares its spectroscopic features. In contrast, the other conformer presumably gained a strong H-bond interaction with the CO ligand based on the dramatic ν(C-O) downshift to ~1917 cm^{-1}. Thus, these RR spectra provided direct evidence in the solution protein for the importance of the YxSxR motif in stabilizing the heme position and orientation within the H-NOX pocket, in addition to its significant effect on modulating the C-O stretching frequency.

In Chapter 4, RR spectroscopy was used to directly measure the Fe-O_2 and O-O bond strengths in *Tt* H-NOX upon disruption of key factors previously shown to influence O_2 ligand affinity through biochemical characterization [38, 45]. Through the substitution of Co^{III}-PPIX into the *Tt* H-NOX, it was possible to directly measure the O-O stretching mode at 1131 cm^{-1}. In addition, two distinct effects were observed on the Fe-O_2 stretching frequency upon either disruption of distal H-bonding residues or addition of steric bulk to the heme pocket. Removal of the H-bonding Tyr-140 resulted in an increased ν(Fe-O_2) relative to WT due to the return of electron density to the Fe-O_2 bond upon elimination of the electrostatic interaction between Tyr-140 and O_2. In contrast, the addition of steric bulk to the heme pocket shifted ν(Fe-O_2) to lower frequencies relative to WT, indicating that the Fe-O_2 bond lengthened upon mutation. In combination with the observed broad heme skeletal mode bands, the ν(Fe-O_2) downshift suggested that the H-NOX domain adopted a more 'open' conformation to accommodate the steric bulk, thereby increasing the distance between Tyr-140 and O_2 and weakening the H-bond that held the diatomic ligand in place. Finally, the importance of a distal H-bond in contributing toward a stable O_2 complex in the H-NOX heme pocket was demonstrated in the *Lp* F142Y mutant with the direct measurement of ν(Fe-O_2) at 563 cm^{-1}.

5.2 Future Studies toward Elucidating the H-NOX Structure-Function Relationship

Genomic analysis has revealed that the H-NOX domains are typically linked to histidine kinases or diguanylate cyclases in the case of facultative aerobes, or to methyl-accepting chemotaxis proteins in obligate anaerobes [2]. It is likely that the H-NOX

domain plays a biological role in the signal transduction to these linked downstream proteins, but the specific details are currently unclear. In addition to understanding how the H-NOX domains control ligand affinity and selectivity, other interesting questions involve the elucidation of how these domains regulate their associated signaling proteins and their functional roles *in vivo*. Much of the current structural characterization on the H-NOX family has been limited to the ~20-25 kDa H-NOX domains due to difficulties with crystallizing full length constructs that include the adjacent proteins. In addition, all of the RR studies conducted thus far on the prokaryotic H-NOX domains have also excluded these adjacently linked proteins. In order to directly address questions regarding the relationship between heme structure and protein function, the use of RR spectroscopy to further characterize constructs containing both the H-NOX domain and its adjacent protein are highly recommended. In combination with some of the current biochemical characterization on these proteins, additional spectroscopic studies on the full length constructs may provide insight to how the heme is involved in the activation of these linked proteins.

5.2.1 Suggestions for Future Experiments on *Tt* H-NOX

As previously mentioned, the majority of the RR spectroscopic, crystallographic, and biochemical characterization of *Tt* H-NOX has involved the construct containing only the first 188 amino acids of the 602-aa length Tar4 MCP [1, 5, 38, 44, 45, 51]. An ongoing hypothesis regarding this protein's *in vivo* role in the thermophilic obligate anaerobe, *Thermoanaerobacter tengcongensis*, is that the binding of O_2 to the heme results in a conformational change that initiates communication from the H-NOX domain to the adjacent MCP, which then signals for the organism to flee from regions of higher O_2 concentration [1, 5, 44]. Thus far, there have been no spectral or structural studies to address this hypothesis.

A clear starting point for investigating this hypothesis would be to express, purify, and characterize the full length Tar4 protein that contains both the *Tt* H-NOX domain and the associated MCP. Steady state Soret-enhanced RR measurements could be made on O_2, NO, and CO-bound complexes of this full length construct to characterize the heme conformation and detect any differences between the types of protein-ligand interactions present in the full length construct versus the *Tt* H-NOX construct alone. Differences in protein-ligand interaction have been previously shown between the CO-bound full length sGC construct and the β1(1-194) heme domain [34], so it is possible that differences would also exist between Tar4 and *Tt* H-NOX. Although the shorter constructs provide a useful basis for initial structural and spectroscopic characterization, it is crucial to conduct spectroscopic studies on the full length proteins since these would ultimately provide the most correct structural observations toward understanding the *in vivo* functional role of the heme and ligand binding in signal transduction.

Once the initial steady state RR characterization is complete, both UV and visible time-resolved RR spectroscopy could be utilized to specifically address the role of the

heme in signal transduction by temporally monitoring the changes in the RR spectra upon ligand binding. From the visible time-resolved RR measurements, one can gain insight into the changes occurring at the heme site and the surrounding protein pocket. In addition, UV time-resolved RR spectroscopy would follow the structural dynamics of any aromatic residues in the H-NOX domain (*i.e.* tyrosine, phenylalanine, tryptophan), focusing more on the protein backbone dynamics [135-138]. However, in order to isolate specific aromatic residues and properly interpret the time-resolved UV RR results, multiple mutations targeting the specific aromatic residues would have to be generated. Still, the combined efforts of both the steady state and time-resolved RR measurements on the *Tt* H-NOX and Tar4 constructs would provide an *in situ* method of probing the heme and protein reactive dynamics in solution.

Another point of interest for the *Tt* H-NOX domain involves the physiological relevance of heme distortion in the thermophilic organism. Thus far, the majority of the biochemical, spectroscopic, and crystallographic characterization of this particular H-NOX domain has been conducted at room temperature or lower [1, 5, 44, 51, 52]. The strictly anaerobic bacteria, *Thermoanaerobacter tengcongensis*, was originally discovered in hot springs from Tengcong, located in the Yunnan Province in China [139]. The temperature of the hot spring from which the organisms were isolated was ~86 °C [139]. At temperatures this high (k_BT = 249 cm^{-1} at 359 K), one would expect more dynamic motion and flexibility within the H-NOX domain so it would seem improbable that the observed heme distortions (normal mode energy < 50 cm^{-1}) should play any functional role due to rapid sampling of different heme conformations. In addition, preliminary RR characterization of O_2-bound *Tt* H-NOX at ~75 °C suggested that the heme sampled a more relaxed conformation at the higher temperature in comparison to room temperature; RR intensity decreases in the low frequency heme out-of-plane modes supported this observation (Figure 5.1). To specifically address this question, additional spectroscopic and biochemical characterization of both the *Tt* H-NOX domain and Tar4 at the physiologically relevant temperature of 75-85 °C should be conducted to determine the importance of heme distortion in signal transduction for *Thermoanaerobacter tengcongensis*. Furthermore, *in vivo* chemotaxis experiments with *T. tengcongensis* involving *Tt* H-NOX mutations that relax the heme could be used to test whether a more relaxed prosthetic group hinders the ability of the H-NOX domain to communicate with the MCP. Until additional characterization is conducted at the biologically relevant temperatures, it remains unclear whether or not heme distortion plays any significant functional role *in vivo*.

5.2.2 Future Experiments with Other Prokaryotic H-NOX Domains

There is currently very little RR characterization of the non-O_2-binding H-NOX domains from facultative aerobes aside from the work by Karow *et al*. and Boon *et al*. [1, 52]. However, phosphorylation assays have been extensively used to probe the role of the H-NOX domain *Shewanella oneidensis* (*So* H-NOX) on the adjacently linked kinase autophosphorylation activity, in addition to other H-NOX domains [42, 140].

Price *et al*. previously demonstrated that the *So* H-NOX protein (SO2144) directly interacted with the sensor histidine kinase (SO2145), and that the kinase was inactivated when NO was bound to the H-NOX domain as a 5-coordinate complex [140]. Erbil *et al*. subsequently used NMR to characterize the CO-bound WT *So* H-NOX and a H103G(im) mutant as structural mimics for the activated and inactivated complexes. This work suggested that concomitant changes occurred in both the heme and the H-NOX domain upon ligand binding; thus, Erbil *et al*. proposed a 'strained heme model' as a means of activation in this H-NOX domain [42]. A change in the heme pocket interactions due to the addition of small molecules is not uncommon. Previous RR studies on full length sGC in the presence of its substrate (GTP) or product (cGMP) have shown that spectral changes occur as a result of these additional molecules [36, 73, 141, 142]. This strongly suggested that the heme pocket is altered upon the binding of these molecules to the enzyme active site.

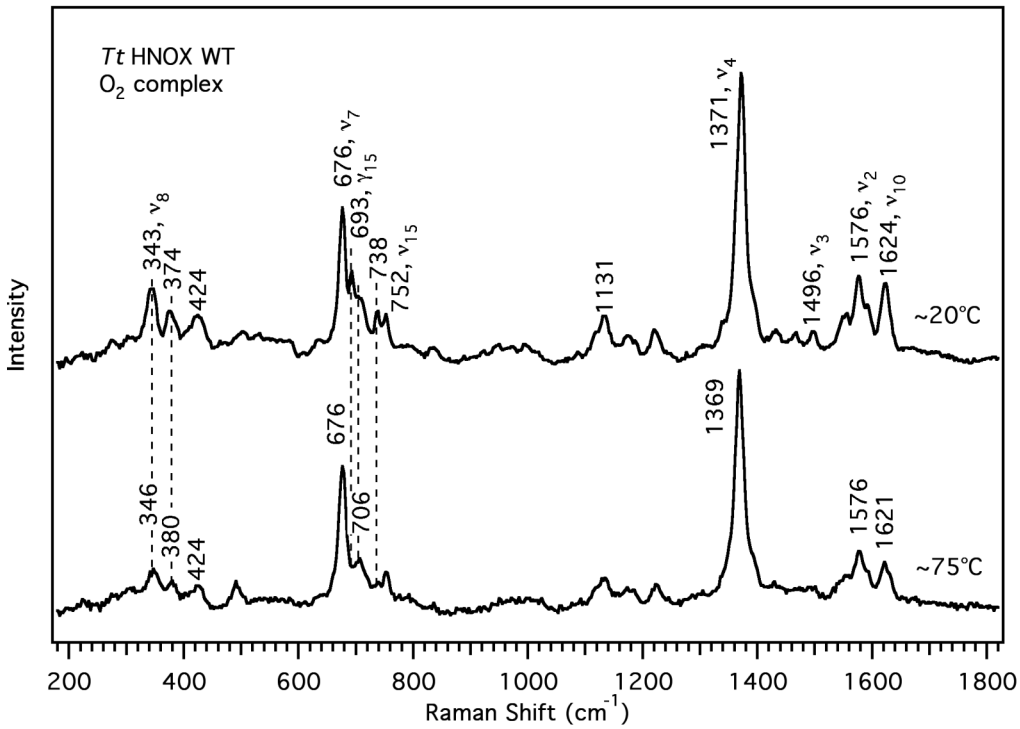

Figure 5.1 Preliminary resonance Raman spectra of O_2-bound *Tt* H-NOX at ~20 °C and ~75 °C. Spectra were acquired for 30 min with 413.1 nm excitation from a Kr^+ source. The laser power was set to ~200 μW due to photolysis of O_2 at higher temperatures.

RR spectroscopy can be applied to *So* H-NOX to specifically probe the heme conformational changes upon binding NO which may be involved in the inhibition of the SO2145 kinase activity. Since it has already been established by Price *et al*. that the *So* H-NOX domain communicates with the *So* histidine kinase as part of a two-component signaling pathway, it would be interesting to explore how the presence of

the histidine kinase affects the *So* H-NOX spectra. Comparisons between the RR spectra of *So* H-NOX in different ligation states, in addition to parallel experiments on the H-NOX domain with its adjacent histidine kinase could potentially reveal detailed information on the changes in the heme conformation.

5.3 Final Remarks

It has been seven years since Iyer *et al*. first demonstrated, through sequence profile searches, the existence of an ancient conserved heme domain that is shared by both eukaryotic sGCs and bacterial signaling proteins [2]. Now identified as the H-NOX domains, a number of structural, biochemical, and functional studies have since been initiated to understand these novel prokaryotic heme domains. However, there is still so much to learn about the vastly diverse H-NOX family, both structurally and functionally as part of multi-component signaling mechanisms. In addition to their potential use as models for the mammalian NO receptor sGC, these bacterial H-NOX domains are interesting due to their divergent ligand binding properties and potential role in signaling. In summary, the work presented in my dissertation has provided a comparative analysis of the heme environmental effects in *Tt* H-NOX. Using a combination of RR spectroscopy and site-directed mutagenesis, I directly probed the interactions between the heme chromophore and the protein pocket *in situ*. It is my hope that this dissertation has contributed toward elucidating the biochemical properties of these H-NOX domains, and provided a starting point for understanding the relationship between heme structure and protein function in this diverse family of diatomic heme sensor domains.

References

1. Karow, D. S., Pan, D., Tran, R., Pellicena, P., Presley, A., Mathies, R. A., and Marletta, M. A. (2004) Spectroscopic characterization of the soluble guanylate cyclase-like heme domains from *Vibrio cholerae* and *Thermoanaerobacter tengcongensis. Biochemistry*, **43**, 10203-10211.
2. Iyer, L. M., Anantharaman, V., and Aravind, L. (2003) Ancient conserved domains shared by animal soluble guanylyl cyclases and bacterial signaling proteins. *BMC Genomics*, **4**, 5.
3. Huang, S. H., Rio, D. C., and Marletta, M. A. (2007) Ligand binding and inhibition of an oxygen-sensitive soluble guanylate cyclase, Gyc-88E, from Drosophila. *Biochemistry*, **46**, 15115-15122.
4. Gray, J. M., Karow, D. S., Lu, H., Chang, A. J., Chang, J. S., Ellis, R. E., Marletta, M. A., and Bargmann, C. I. (2004) Oxygen sensation and social feeding mediated by a *C. elegans* guanylate cyclase homologue. *Nature*, **430**, 317-322.
5. Pellicena, P., Karow, D. S., Boon, E. M., Marletta, M. A., and Kuriyan, J. (2004) Crystal structure of an oxygen-binding heme domain related to soluble guanylate cyclases. *Proc. Natl. Acad. Sci. U.S.A.*, **101**, 12854-12859.
6. Bredt, D. S. and Snyder, S. H. (1994) Nitric-Oxide - a Physiological Messenger Molecule. *Annual Review of Biochemistry*, **63**, 175-195.
7. Gross, S. S. and Wolin, M. S. (1995) Nitric-Oxide - Pathophysiological Mechanisms. *Annual Review of Physiology*, **57**, 737-769.
8. Moncada, S., Palmer, R. M. J., and Higgs, E. A. (1991) Nitric-Oxide - Physiology, Pathophysiology, and Pharmacology. *Pharmacological Reviews*, **43**, 109-142.
9. Wink, D. A., Feelisch, M., Fukuto, J., Chistodoulou, D., Jourd'heuil, D., Grisham, M. B., Vodovotz, Y., Cook, J. A., Krishna, M., DeGraff, W. G., Kim, S., Gamson, J., and Mitchell, J. B. (1998) The cytotoxicity of nitroxyl: Possible implications for the pathophysiological role of NO. *Archives of Biochemistry and Biophysics*, **351**, 66-74.
10. Thomas, D. D., Ridnour, L. A., Isenberg, J. S., Flores-Santana, W., Switzer, C. H., Donzelli, S., Hussain, P., Vecoli, C., Paolocci, N., Ambs, S., Colton, C. A., Harris, C. C., Roberts, D. D., and Wink, D. A. (2008) The chemical biology of nitric oxide: Implications in cellular signaling. *Free Radical Biology and Medicine*, **45**, 18-31.
11. Wink, D. A., Hanbauer, I., Grisham, M. B., Laval, F., Nims, R. W., Lavals, J., Cook, J., Pacelli, R., Liebmann, J., Krishna, M., Ford, P. C., and Mitchell, J. B. (1996) Chemical biology of nitric oxide: Regulation and protective and toxic mechanisms. *Current Topics in Cellular Regulation*, **34**, 159-187.
12. Beckman, J. S. and Koppenol, W. H. (1996) Nitric oxide, superoxide, and peroxynitrite: The good, the bad, and the ugly. *American Journal of Physiology-Cell Physiology*, **40**, C1424-C1437.

13. Furchgott, R. F. and Vanhoutte, P. M. (1989) Endothelium-Derived Relaxing and Contracting Factors. *FASEB Journal*, **3**, 2007-2018.
14. Osto, E., Tona, F., De Bon, E., Iliceto, S., and Cella, G. (2010) Endothelial Dysfunction in Cardiac Allograft Vasculopathy: Potential Pharmacological Interventions. *Current Vascular Pharmacology*, **8**, 169-188.
15. Granger, D. L. and Hibbs, J. B. (1996) High-output nitric oxide: Weapon against infection? *Trends in Microbiology*, **4**, 46-47.
16. Granger, D. N. and Kubes, P. (1996) Nitric oxide as antiinflammatory agent. *Nitric Oxide, Pt B*, **269**, 434-442.
17. Stuehr, D. J. and Nathan, C. F. (1989) Nitric-Oxide - a Macrophage Product Responsible for Cytostasis and Respiratory Inhibition in Tumor Target-Cells. *Journal of Experimental Medicine*, **169**, 1543-1555.
18. Nathan, C. F. and Hibbs, J. B. (1991) Role of Nitric-Oxide Synthesis in Macrophage Antimicrobial Activity. *Current Opinion in Immunology*, **3**, 65-70.
19. Bogdan, C. (2001) Nitric oxide and the immune response. *Nature Immunology*, **2**, 907-916.
20. Dedon, P. C. and Tannenbaum, S. R. (2004) Reactive nitrogen species in the chemical biology of inflammation. *Archives of Biochemistry and Biophysics*, **423**, 12-22.
21. Miranda, K. M., Espey, M. G., and Wink, D. A. (2000) A discussion of the chemistry of oxidative and nitrosative stress in cytotoxicity. *J. Inorg. Biochem.*, **79**, 237-240.
22. Ignarro, L. J. (1990) Biosynthesis and Metabolism of Endothelium-Derived Nitric-Oxide. *Annual Review of Pharmacology and Toxicology*, **30**, 535-560.
23. Murad, F. (1994) The Nitric-Oxide Cyclic-Gmp Signal-Transduction System for Intracellular and Intercellular Communication. *Recent Progress in Hormone Research*, **49**, 239-248.
24. Garthwaite, J. (1995) Neural Nitric-Oxide Signaling. *Trends in Neurosciences*, **18**, 51-52.
25. Garthwaite, J. and Boulton, C. L. (1995) Nitric-Oxide Signaling in the Central-Nervous-System. *Annual Review of Physiology*, **57**, 683-706.
26. Denninger, J. W. and Marletta, M. A. (1999) Guanylate cyclase and the .NO/cGMP signaling pathway. *Biochim Biophys Acta*, **1411**, 334-350.
27. Derbyshire, E. R. and Marletta, M. A. (2009) Biochemistry of soluble guanylate cyclase. *Handb Exp Pharmacol*, 17-31.
28. Alderton, W. K., Cooper, C. E., and Knowles, R. G. (2001) Nitric oxide synthases: structure, function and inhibition. *Biochemical Journal*, **357**, 593-615.
29. Marletta, M. A. (1994) Nitric-Oxide Synthase - Aspects Concerning Structure and Catalysis. *Cell*, **78**, 927-930.
30. Lewis, R. S., Tamir, S., Tannenbaum, S. R., and Deen, W. M. (1995) Kinetic-Analysis of the Fate of Nitric-Oxide Synthesized by Macrophages in-Vitro. *J. Biol. Chem.*, **270**, 29350-29355.
31. Mungrue, I. N., Husain, M., and Stewart, D. J. (2002) The role of NOS in heart failure: lessons from murine genetic models. *Heart Fail Rev*, **7**, 407-422.

32. Poulos, T. L. (2006) Soluble guanylate cyclase. *Curr Opin Struct Biol*, **16**, 736-743.
33. Winger, J. A. and Marletta, M. A. (2005) Expression and characterization of the catalytic domains of soluble guanylate cyclase: Interaction with the heme domain. *Biochemistry*, **44**, 4083-4090.
34. Karow, D. S., Pan, D. H., Davis, J. H., Behrends, S., Mathies, R. A., and Marletta, M. A. (2005) Characterization of functional heme domains from soluble guanylate cyclase. *Biochemistry*, **44**, 16266-16274.
35. Stone, J. R. and Marletta, M. A. (1994) Soluble Guanylate-Cyclase from Bovine Lung - Activation with Nitric-Oxide and Carbon-Monoxide and Spectral Characterization of the Ferrous and Ferric States. *Biochemistry*, **33**, 5636-5640.
36. Pal, B., Li, Z. Q., Ohta, T., Takenaka, S., Tsuyama, S., and Kitagawa, T. (2004) Resonance Raman study on synergistic activation of soluble guanylate cyclase by imidazole, YC-1 and GTP. *J. Inorg. Biochem.*, **98**, 824-832.
37. Makino, R., Obayashi, E., Homma, N., Shiro, Y., and Hori, H. (2003) YC-1 facilitates release of the proximal his residue in the NO and CO complexes of soluble guanylate cyclase. *J. Biol. Chem.*, **278**, 11130-11137.
38. Boon, E. M., Huang, S. H., and Marletta, M. A. (2005) A molecular basis for NO selectivity in soluble guanylate cyclase. *Nat Chem Biol*, **1**, 53-59.
39. Boon, E. M. and Marletta, M. A. (2005) Ligand discrimination in soluble guanylate cyclase and the H-NOX family of heme sensor proteins. *Curr Opin Chem Biol*, **9**, 441-446.
40. Kim, S. Y., Deinum, G., Gardner, M. T., Marletta, M. A., and Babcock, G. T. (1996) Distal pocket polarity in the unusual ligand binding site of soluble guanylate cyclase: Implications for the control of center dot NO binding. *J. Am. Chem. Soc.*, **118**, 8769-8770.
41. Martin, E., Berka, V., Bogatenkova, E., Murad, F., and Tsai, A. L. (2006) Ligand selectivity of soluble guanylyl cyclase - Effect of the hydrogen-bonding tyrosine in the distal heme pocket on binding of oxygen, nitric oxide, and carbon monoxide. *J. Biol. Chem.*, **281**, 27836-27845.
42. Erbil, W. K., Price, M. S., Wemmer, D. E., and Marletta, M. A. (2009) A structural basis for H-NOX signaling in Shewanella oneidensis by trapping a histidine kinase inhibitory conformation. *Proc. Natl. Acad. Sci. U.S.A.*, **106**, 19753-19760.
43. Ma, X. L., Sayed, N., Beuve, A., and van den Akker, F. (2007) NO and CO differentially activate soluble guanylyl cyclase via a heme pivot-bend mechanism. *EMBO J.*, **26**, 578-588.
44. Olea, C., Boon, E. M., Pellicena, P., Kuriyan, J., and Marletta, M. A. (2008) Probing the Function of Heme Distortion in the H-NOX Family. *ACS Chem. Biol.*, **3**, 703-710.
45. Weinert, E. E., Plate, L., Whited, C. A., Olea, C., and Marletta, M. A. (2010) Determinants of Ligand Affinity and Heme Reactivity in H-NOX Domains. *Angew Chem Int Edit*, **49**, 720-723.
46. Nioche, P., Berka, V., Vipond, J., Minton, N., Tsai, A. L., and Raman, C. S. (2004) Femtomolar sensitivity of a NO sensor from *Clostridium botulinum*. *Science*, **306**, 1550-1553.

47. Boon, E. M. and Marletta, M. A. (2005) Ligand specificity of H-NOX domains: from sGC to bacterial NO sensors. *J. Inorg. Biochem.*, **99**, 892-902.
48. Jentzen, W., Ma, J. G., and Shelnutt, J. A. (1998) Conservation of the conformation of the porphyrin macrocycle in hemoproteins. *Biophys. J.*, **74**, 753-763.
49. Jentzen, W., Song, X. Z., and Shelnutt, J. A. (1997) Structural characterization of synthetic and protein-bound porphyrins in terms of the lowest-frequency normal coordinates of the macrocycle. *J. Phys. Chem. B*, **101**, 1684-1699.
50. Shelnutt, J. A., Song, X. Z., Ma, J. G., Jia, S. L., Jentzen, W., and Medforth, C. J. (1998) Nonplanar porphyrins and their significance in proteins. *Chem. Soc. Rev.*, **27**, 31-41.
51. Tran, R., Boon, E. M., Marletta, M. A., and Mathies, R. A. (2009) Resonance Raman Spectra of an O_2-Binding H-NOX Domain Reveal Heme Relaxation upon Mutation. *Biochemistry*, **48**, 8568-8577.
52. Boon, E. M., Davis, J. H., Tran, R., Karow, D. S., Huang, S. H., Pan, D., Miazgowicz, M. M., Mathies, R. A., and Marletta, M. A. (2006) Nitric oxide binding to prokaryotic homologs of the soluble guanylate cyclase β1 H-NOX domain. *J. Biol. Chem.*, **281**, 21892-21902.
53. Yang, J., Kloek, A. P., Goldberg, D. E., and Mathews, F. S. (1995) The structure of Ascaris hemoglobin domain I at 2.2 Å resolution: molecular features of oxygen avidity. *Proc. Natl. Acad. Sci. U.S.A.*, **92**, 4224-4228.
54. Rothkegel, C., Schmidt, P. M., Stoll, F., Schroder, H., Schmidt, H. H. H. W., and Stasch, J. P. (2006) Identification of residues crucially involved in soluble guanylate cyclase activation. *FEBS Lett.*, **580**, 4205-4213.
55. Gouterman, M., Snyder, L. C., and Wagniere, G. H. (1963) Spectra of Porphyrins .2. 4 Orbital Model. *J Mol Spectrosc*, **11**, 108-127.
56. Spiro, T. G. and Li, X. Y., *Resonance Raman Spectroscopy of Metalloporphyrins*, in *Biological Applications of Raman Spectroscopy: Resonance Raman spectra of heme and metalloproteins*, T.G. Spiro, Editor. 1988, John Wiley & Sons: New York. p. 1-37.
57. Myers, A. B. and Mathies, R., *Resonance Raman Intensities: A Probe of Excited State Structure and Dynamics*, in *Biological applications of Raman spectroscopy: Resonance Raman spectra of polyenes and aromatics*, T.G. Spiro, Editor. 1988, John Wiley & Sons: New York. p. 1-58.
58. Felton, R. H. and Yu, N. T., *Resonance Raman Scattering from Metalloporphyrins and Hemoproteins*, in *The Porphyrins*, D. Dolphin, Editor. 1978, Academic Press, Inc.: New York. p. 347-393.
59. Albrecht, A. C. (1961) Theory of Raman Intensities. *J. Chem. Phys.*, **34**, 1476-1484.
60. Tang, J. and Albrecht, A. C. (1968) Studies in Raman Intensity Theory. *J. Chem. Phys.*, **49**, 1144-1154.
61. Lee, S. Y. and Heller, E. J. (1979) Time-Dependent Theory of Raman-Scattering. *J. Chem. Phys.*, **71**, 4777-4788.
62. Uchida, T. and Kitagawa, T. (2005) Mechanism for transduction of the ligand-binding signal in heme-based gas sensory proteins revealed by resonance Raman spectroscopy. *Accounts of Chemical Research*, **38**, 662-670.

63. Kitagawa, T., *The Heme Protein Structure and the Iron-Histidine Stretching Mode*, in *Biological Applications of Raman Spectroscopy: Resonance Raman Spectra of Heme and Metalloproteins*, T.G. Spiro, Editor. 1988, John Wiley & Sons: New York. p. 97-131.
64. Choi, S., Spiro, T. G., Langry, K. C., Smith, K. M., Budd, D. L., and Lamar, G. N. (1982) Structural Correlations and Vinyl Influences in Resonance Raman Spectra of Protoheme Complexes and Proteins. *J. Am. Chem. Soc.*, **104**, 4345-4351.
65. Choi, S. H. and Spiro, T. G. (1983) Out-of-Plane Deformation Modes in the Resonance Raman Spectra of Metalloporphyrins and Heme Proteins. *J. Am. Chem. Soc.*, **105**, 3683-3692.
66. Das, T. K., Couture, M., Ouellet, Y., Guertin, M., and Rousseau, D. L. (2001) Simultaneous observation of the O-O and Fe-O_2 stretching modes in oxyhemoglobins. *Proc. Natl. Acad. Sci. U.S.A.*, **98**, 479-484.
67. Deinum, G., Stone, J. R., Babcock, G. T., and Marletta, M. A. (1996) Binding of nitric oxide and carbon monoxide to soluble guanylate cyclase as observed with resonance Raman spectroscopy. *Biochemistry*, **35**, 1540-1547.
68. Denninger, J. W., Schelvis, J. P. M., Brandish, P. E., Zhao, Y., Babcock, G. T., and Marletta, M. A. (2000) Interaction of soluble guanylate cyclase with YC-1: Kinetic and resonance Raman studies. *Biochemistry*, **39**, 4191-4198.
69. Franzen, S., Boxer, S. G., Dyer, R. B., and Woodruff, W. H. (2000) Resonance Raman studies of heme axial ligation in H93G myoglobin. *J. Phys. Chem. B*, **104**, 10359-10367.
70. Huang, Q. and Schweitzer-Stenner, R. (2005) Non-planar heme deformations and excited state displacements in horseradish peroxidase detected by Raman spectroscopy at Soret excitation. *J. Raman Spectrosc.*, **36**, 363-375.
71. Irwin, M. J., Armstrong, R. S., and Wright, P. E. (1981) Resonance Raman Studies of Soybean Leghemoglobin and Myoglobin - Origin of the Differences in O_2 Dissociation Rate Constants. *FEBS Lett.*, **133**, 239-243.
72. Li, X. Y. and Spiro, T. G. (1988) Is Bound Co Linear or Bent in Heme-Proteins - Evidence from Resonance Raman and Infrared Spectroscopic Data. *J. Am. Chem. Soc.*, **110**, 6024-6033.
73. Li, Z. Q., Pal, B., Takenaka, S., Tsuyama, S., and Kitagawa, T. (2005) Resonance Raman evidence for the presence of two heme pocket conformations with varied activities in CO-bound bovine soluble guanylate cyclase and their conversion. *Biochemistry*, **44**, 939-946.
74. Mackin, H. C., Tsubaki, M., and Yu, N. T. (1983) Resonance Raman Studies of Co-O_2 and O-O Stretching Vibrations in Oxy-Cobalt Hemes. *Biophys. J.*, **41**, 349-357.
75. Ramsden, J. and Spiro, T. G. (1989) Resonance Raman Evidence That Distal Histidine Protonation Removes the Steric Hindrance to Upright Binding of Carbon-Monoxide by Myoglobin. *Biochemistry*, **28**, 3125-3128.
76. Ray, G. B., Li, X. Y., Ibers, J. A., Sessler, J. L., and Spiro, T. G. (1994) How Far Can Proteins Bend the Feco Unit - Distal Polar and Steric Effects in Heme-Proteins and Models. *J. Am. Chem. Soc.*, **116**, 162-176.

77. Schelvis, J. P. M., Zhao, Y., Marletta, M. A., and Babcock, G. T. (1998) Resonance Raman characterization of the heme domain of soluble guanylate cyclase. *Biochemistry*, **37**, 16289-16297.
78. Spiro, T. G. and Stein, P. (1977) Resonance Effects in Vibrational Scattering from Complex-Molecules. *Annual Review of Physical Chemistry*, **28**, 501-521.
79. Spiro, T. G., Stong, J. D., and Stein, P. (1979) Porphyrin Core Expansion and Doming in Heme Proteins - New Evidence from Resonance Raman Spectra of 6-Coordinate High-Spin Iron(III) Hemes. *J. Am. Chem. Soc.*, **101**, 2648-2655.
80. Spiro, T. G. and Wasbotten, I. H. (2005) CO as a vibrational probe of heme protein active sites. *J. Inorg. Biochem.*, **99**, 34-44.
81. Tomita, T., Gonzalez, G., Chang, A. L., Ikeda-Saito, M., and Gilles-Gonzalez, M. A. (2002) A comparative resonance Raman analysis of heme-binding PAS domains: heme iron coordination structures of the *Bj*FixL, *Ax*PDEA1, *Ec*Dos, and *Mt*Dos proteins. *Biochemistry*, **41**, 4819-4826.
82. Yu, N. T. and Kerr, E. A., *Vibrational Modes of Coordinated CO, CN, O_2, and NO*, in *Biological Applications of Raman Spectroscopy: Resonance Raman Spectra of Heme and Metalloproteins*, T.G. Spiro, Editor. 1988, John Wiley & Sons: New York. p. 39-95.
83. Yu, N. T., Kerr, E. A., Ward, B., and Chang, C. K. (1983) Resonance Raman Detection of Fe-Co Stretching and Fe-C-O Bending Vibrations in Sterically Hindered Carbonmonoxy Strapped Hemes - a Structural Probe of Fe-C-O Distortion. *Biochemistry*, **22**, 4534-4540.
84. Spiro, T. G., Zgierski, M. Z., and Kozlowski, P. M. (2001) Stereoelectronic factors in CO, NO and O-2 binding to heme from vibrational spectroscopy and DFT analysis. *Coordination Chemistry Reviews*, **219**, 923-936.
85. Blackwood, M. E., Rush, T. S., Medlock, A., Dailey, H. A., and Spiro, T. G. (1997) Resonance Raman spectra of ferrochelatase reveal porphyrin distortion upon metal binding. *J. Am. Chem. Soc.*, **119**, 12170-12174.
86. Jarzecki, A. A. and Spiro, T. G. (2005) Porphyrin distortion from resonance Raman intensities of out-of-plane modes: Computation and modeling of N-methylmesoporphlyrin, a ferrochelatase transition state analog. *J. Phys. Chem. A*, **109**, 421-430.
87. Sparks, L. D., Anderson, K. K., Medforth, C. J., Smith, K. M., and Shelnutt, J. A. (1994) Correlations between Raman Frequencies and Structure for Planar and Nonplanar Metalloporphyrins. *Inorg. Chem.*, **33**, 2297-2302.
88. Huang, Q., Medforth, C. J., and Schweitzer-Stenner, R. (2005) Nonplanar heme deformations and excited state displacements in nickel porphyrins detected by Raman spectroscopy at Soret excitation. *J. Phys. Chem. A*, **109**, 10493-10502.
89. Sigfridsson, E. and Ryde, U. (2003) The importance of porphyrin distortions for the ferrochelatase reaction. *J. Biol. Inorg. Chem.*, **8**, 273-282.
90. Kozlowski, P. M., Rush, T. S., Jarzecki, A. A., Zgierski, M. Z., Chase, B., Piffat, C., Ye, B. H., Li, X. Y., Pulay, P., and Spiro, T. G. (1999) DFT-SQM force field for nickel porphine: Intrinsic ruffling. *J. Phys. Chem. A*, **103**, 1357-1366.
91. Xu, C. L., Ibrahim, M., and Spiro, T. G. (2008) DFT analysis of axial and equatorial effects on Heme-CO vibrational modes: Applications to CooA and H-NOX heme sensor proteins. *Biochemistry*, **47**, 2379-2387.

92. Jentzen, W., Simpson, M. C., Hobbs, J. D., Song, X., Ema, T., Nelson, N. Y., Medforth, C. J., Smith, K. M., Veyrat, M., Mazzanti, M., Ramasseul, R., Marchon, J. C., Takeuchi, T., Goddard, W. A., and Shelnutt, J. A. (1995) Ruffling in a Series of Nickel(II) Meso-Tetrasubstituted Porphyrins as a Model for the Conserved Ruffling of the Heme of Cytochromes-c. *J. Am. Chem. Soc.*, **117**, 11085-11097.
93. Czernuszewicz, R. S., Li, X. Y., and Spiro, T. G. (1989) Nickel Octaethylporphyrin Ruffling Dynamics from Resonance Raman Spectroscopy. *J. Am. Chem. Soc.*, **111**, 7024-7031.
94. Gilles-Gonzalez, M. A. and Gonzalez, G. (2005) Heme-based sensors: defining characteristics, recent developments, and regulatory hypotheses. *J. Inorg. Biochem.*, **99**, 1-22.
95. Mathies, R. and Yu, N. T. (1978) Raman Spectroscopy with Intensified Vidicon Detectors - Study of Intact Bovine Lens Proteins. *J. Raman Spectrosc.*, **7**, 349-352.
96. Gong, W., Hao, B., and Chan, M. K. (2000) New mechanistic insights from structural studies of the oxygen-sensing domain of *Bradyrhizobium japonicum* FixL. *Biochemistry*, **39**, 3955-3962.
97. Milani, M., Pesce, A., Ouellet, Y., Ascenzi, P., Guertin, M., and Bolognesi, M. (2001) Mycobacterium tuberculosis hemoglobin N displays a protein tunnel suited for O_2 diffusion to the heme. *EMBO J.*, **20**, 3902-3909.
98. Vojtechovsky, J., Chu, K., Berendzen, J., Sweet, R. M., and Schlichting, I. (1999) Crystal structures of myoglobin-ligand complexes at near-atomic resolution. *Biophys. J.*, **77**, 2153-2174.
99. Antonini, E. and Brunori, M., *Hemoglobin and myoglobin in their reactions with ligands*. Frontiers of Biology, ed. A. Neuberger and E.L. Tatum. Vol. 21. 1971, Amsterdam: North-Holland Publishing Company. 1-37.
100. Levantino, M., Huang, Q., Cupane, A., Laberge, M., Hagarman, A., and Schweitzer-Stenner, R. (2005) The importance of vibronic perturbations in ferrocytochrome c spectra: A reevaluation of spectral properties based on low-temperature optical absorption, resonance Raman, and molecular-dynamics simulations. *J. Chem. Phys.*, **123**, 054508-1 - 054508-12.
101. Takahashi, S., Ishikawa, K., Takeuchi, N., Ikedasaito, M., Yoshida, T., and Rousseau, D. L. (1995) Oxygen-Bound Heme-Heme Oxygenase Complex - Evidence for a Highly Bent Structure of the Coordinated Oxygen. *J. Am. Chem. Soc.*, **117**, 6002-6006.
102. Tamura, K., Nakamura, H., Tanaka, Y., Oue, S., Tsukamoto, K., Nomura, M., Tsuchiya, T., Adachi, S., Takahashi, S., Iizuka, T., and Shiro, Y. (1996) Nature of endogenous ligand binding to heme iron in oxygen sensor FixL. *J. Am. Chem. Soc.*, **118**, 9434-9435.
103. Hu, S. Z., Smith, K. M., and Spiro, T. G. (1996) Assignment of protoheme Resonance Raman spectrum by heme labeling in myoglobin. *J. Am. Chem. Soc.*, **118**, 12638-12646.
104. Rush, T. S., Kozlowski, P. M., Piffat, C. A., Kumble, R., Zgierski, M. Z., and Spiro, T. G. (2000) Computational modeling of metalloporphyrin structure and

vibrational spectra: Porphyrin ruffling in NiTPP. *J. Phys. Chem. B*, **104**, 5020-5034.
105. Badger, R. M. (1935) The relation between the internuclear distances and force constants of molecules and its application to polyatomic molecules. *J. Chem. Phys.*, **3**, 710-714.
106. Green, M. T. (2006) Application of Badger's rule to heme and non-heme iron-oxygen bonds: An examination of ferryl protonation states. *J. Am. Chem. Soc.*, **128**, 1902-1906.
107. Kozlowski, P. M., Vogel, K. M., Zgierski, M. Z., and Spiro, T. G. (2001) Steric contributions to CO binding in heme proteins: a density functional analysis of FeCO vibrations and deformability. *Journal of Porphyrins and Phthalocyanines*, **5**, 312-322.
108. Decatur, S. M. and Boxer, S. G. (1995) A Test of the Role of Electrostatic Interactions in Determining the Co Stretch Frequency in Carbonmonoxymyoglobin. *Biochemical and Biophysical Research Communications*, **212**, 159-164.
109. Decatur, S. M., Belcher, K. L., Rickert, P. K., Franzen, S., and Boxer, S. G. (1999) Hydrogen bonding modulates binding of exogenous ligands in a myoglobin proximal cavity mutant. *Biochemistry*, **38**, 11086-11092.
110. Decatur, S. M., DePillis, G. D., and Boxer, S. G. (1996) Modulation of protein function by exogenous ligands in protein cavities: CO binding to a myoglobin cavity mutant containing unnatural proximal ligands. *Biochemistry*, **35**, 3925-3932.
111. Kerr, E. A., Mackin, H. C., and Yu, N. T. (1983) Resonance Raman Studies of Carbon-Monoxide Binding to Iron Picket Fence Porphyrin with Unhindered and Hindered Axial Bases - an Inverse Relationship between Binding-Affinity and the Strength of Iron Carbon Bond. *Biochemistry*, **22**, 4373-4379.
112. Kushkuley, B. and Stavrov, S. S. (1996) Theoretical study of the distal-side steric and electrostatic effects on the vibrational characteristics of the FeCO unit of the carbonylheme proteins and their models. *Biophys. J.*, **70**, 1214-1229.
113. Li, T. S., Quillin, M. L., Phillips, G. N., and Olson, J. S. (1994) Structural Determinants of the Stretching Frequency of Co Bound to Myoglobin. *Biochemistry*, **33**, 1433-1446.
114. Phillips, G. N., Teodoro, M. L., Li, T. S., Smith, B., and Olson, J. S. (1999) Bound CO is a molecular probe of electrostatic potential in the distal pocket of myoglobin. *J. Phys. Chem. B*, **103**, 8817-8829.
115. Tsubaki, M., Srivastava, R. B., and Yu, N. T. (1982) Resonance Raman Investigation of Carbon-Monoxide Bonding in (Carbon Monoxy) Hemoglobin and (Carbon Monoxy) Myoglobin - Detection of Fe-Co Stretching and Fe-C-O Bending Vibrations and Influence of the Quaternary Structure Change. *Biochemistry*, **21**, 1132-1140.
116. Vogel, K. M., Kozlowski, P. M., Zgierski, M. Z., and Spiro, T. G. (1999) Determinants of the FeXO (X = C, N, O) vibrational frequencies in heme adducts from experiment and density functional theory. *J. Am. Chem. Soc.*, **121**, 9915-9921.

117. Vogel, K. M., Kozlowski, P. M., Zgierski, M. Z., and Spiro, T. G. (2000) Role of the axial ligand in heme-CO backbonding; DFT analysis of vibrational data. *Inorganica Chimica Acta*, **297**, 11-17.
118. Zhao, Y., Schelvis, J. P. M., Babcock, G. T., and Marletta, M. A. (1998) Identification of histidine 105 in the beta 1 subunit of soluble guanylate cyclase as the heme proximal ligand. *Biochemistry*, **37**, 4502-4509.
119. Andrew, C. R., Green, E. L., Lawson, D. M., and Eady, R. R. (2001) Resonance Raman studies of cytochrome c ' support the binding of NO and CO to opposite sides of the heme: Implications for ligand discrimination in heme-based sensors. *Biochemistry*, **40**, 4115-4122.
120. Aono, S., Kato, T., Matsuki, M., Nakajima, H., Ohta, T., Uchida, T., and Kitagawa, T. (2002) Resonance Raman and ligand binding studies of the oxygen-sensing signal transducer protein HemAT from Bacillus subtilis. *J. Biol. Chem.*, **277**, 13528-13538.
121. Tani, F., Matsu-ura, M., Ariyama, K., Setoyama, T., Shimada, T., Kobayashi, S., Hayashi, T., Matsuo, T., Hisaeda, Y., and Naruta, Y. (2003) Iron twin-coronet porphyrins as models of myoglobin and hemoglobin: Amphibious electrostatic effects of overhanging hydroxyl groups for successful CO/O_2 discrimination. *Chem-Eur J*, **9**, 862-870.
122. Spiro, T. G. and Kozlowski, P. M. (1998) Discordant results on FeCO deformability in heme proteins reconciled by density functional theory. *J. Am. Chem. Soc.*, **120**, 4524-4525.
123. Spiro, T. G. and Kozlowski, P. M. (2001) Is the CO adduct of myoglobin bent, and does it matter? *Accounts of Chemical Research*, **34**, 137-144.
124. Springer, B. A., Sligar, S. G., Olson, J. S., and Phillips, G. N. (1994) Mechanisms of Ligand Recognition in Myoglobin. *Chemical Reviews*, **94**, 699-714.
125. Momenteau, M. and Reed, C. A. (1994) Synthetic Heme Dioxygen Complexes. *Chemical Reviews*, **94**, 659-698.
126. Woodward, J. J., Martin, N. I., and Marletta, M. A. (2007) An Escherichia coli expression-based method for heme substitution. *Nature Methods*, **4**, 43-45.
127. Yonetani, T., Yamamoto, H., and Woodrow, G. V. (1974) Studies on Cobalt Myoglobins and Hemoglobins .1. Preparation and Optical-Properties of Myoglobins and Hemoglobins Containing Cobalt Proto-Porphyrins, Meso-Porphyrins, and Deuteroporphyrins and Thermodynamic Characterization of Their Reversible Oxygenation. *J. Biol. Chem.*, **249**, 682-690.
128. Weinert, E. E., Tran, R., Boon, E. M., Mathies, R. A., and Marletta, M. A., *Role of Ile5 in the Conformational Flexibility of an O_2-binding H-NOX Domain*. 2010.
129. Bruha, A. and Kincaid, J. R. (1988) Resonance Raman Studies of Dioxygen Adducts of Cobalt-Substituted Heme-Proteins and Model Compounds - Vibrationally Coupled Dioxygen and the Issues of Multiple Structures and Distal Side Hydrogen-Bonding. *J. Am. Chem. Soc.*, **110**, 6006-6014.
130. Yu, C. A. and Gunsalus, I. C. (1974) Cytochrome-P-450 Cam: (III) Removal and Replacement of Ferriprotoporphyrin-IX. *J. Biol. Chem.*, **249**, 107-110.

131. Brucker, E. A., Olson, J. S., Phillips, G. N., Dou, Y., and Ikeda-Saito, M. (1996) High resolution crystal structures of the deoxy, oxy, and aquomet forms of cobalt myoglobin. *J. Biol. Chem.*, **271**, 25419-25422.
132. Hoffman, B. M. and Petering, D. H. (1970) Coboglobins - Oxygen-Carrying Cobalt-Reconstituted Hemoglobin and Myoglobin. *Proc. Natl. Acad. Sci. U.S.A.*, **67**, 637-643.
133. Tran, R., *Probing the heme structure and environment of bacterial Heme-Nitric oxide/OXygen binding domains with resonance Raman spectroscopy*. 2010, Ph.D. Dissertation in Chemistry. University of California, Berkeley. p. 1-117.
134. Herschbach, D. and Laurie, V. W. (1961) Anharmonic Potential Constants and Their Dependence Upon Bond Length. *J. Chem. Phys.*, **35**, 458-463.
135. Balakrishnan, G., Ibrahim, M., and Spiro, T. G. (2007) Time-resolved UV resonance Raman spectroscopy with sub-microsecond photolysis pulse reveals new insights in the allosteric pathway of hemoglobin. *Biophys. J.*, 381A-381A.
136. Ibrahim, M., Balakrishnan, G., Kuchinskas, M., Kerby, R. L., Youn, H., Roberts, G. P., Poulos, T. L., and Spiro, T. G. (2007) Heme displacement mechanism of CooA activation: Evidence from UV and visible resonance raman spectroscopies. *Biophys. J.*, 381A-381A.
137. Kim, J. E., Pan, D. H., and Mathies, R. A. (2003) Picosecond dynamics of G-protein coupled receptor activation in rhodopsin from time-resolved UV resonance Raman spectroscopy. *Biochemistry*, **42**, 5169-5175.
138. Kneipp, J., Balakrishnan, G., Chen, R. P., Wu, Q., Giovannelli, J. L., Tam, T. C. S., Chien, H., and Spiro, T. G. (2005) Time-resolved UV resonance Raman spectroscopy of hemoglobin sitemutants to study the role of interhelical tyrosine H-bonds. *Biophys. J.*, **88**, 392A-392A.
139. Xue, Y. F., Xu, Y., Liu, Y., Ma, Y. H., and Zhou, P. J. (2001) Thermoanaerobacter tengcongensis sp nov., a novel anaerobic, saccharolytic, thermophilic bacterium isolated from a hot spring in Tengcong, China. *Int J Syst Evol Micr*, **51**, 1335-1341.
140. Price, M. S., Chao, L. Y., and Marletta, M. A. (2007) Shewanella oneidensis MR-1 H-NOX regulation of a histidine kinase by nitric oxide. *Biochemistry*, **46**, 13677-13683.
141. Pal, B. and Kitagawa, T. (2005) Interactions of soluble guanylate cyclase with diatomics as probed by resonance Raman spectroscopy. *J. Inorg. Biochem.*, **99**, 267-279.
142. Tomita, T., Ogura, T., Tsuyama, S., Imai, Y., and Kitagawa, T. (1997) Effects of GTP on bound nitric oxide of soluble guanylate cyclase probed by resonance Raman spectroscopy. *Biochemistry*, **36**, 10155-10160.

Appendix

Table 1A Heme skeletal modes for various H-NOX domains and their mutants in the 5-coordinate, ferrous unligated form.[a]

Protein	coord.	ν_{10}	ν_2	ν_3	ν_4	ν(Fe-His)
Fe(II)-unligated						
β1 (1-194)	5, hs	1608	1568	1478	1359	208
β1 (1-385)	5, hs	1607	1563	1474	1358	206
β2 (1-217)	5, hs	1609	1567	1477	1359	207
sGC WT	5, hs	1606	1562	1471	1358	204
rat β1 (1-194) WT	5, hs	1603	1560	1470	1356	203
rat β1 (1-194) P118A	5, hs	1603	1558	1470	1356	211
rat β1 (1-194) I145Y	5, hs	1606	1563	1473	1358	211
rat β1 (1-385) WT	5, hs	1604	1561	1473	1355	206
rat β1 (1-385) I145Y	5, hs	---	---	1470	1366	209
rat sGC WT	5, hs	1606	1561	1473	1355	205
rat sGC I145Y	5, hs	1605	1560	1472	1356	208
Cc H-NOX WT	5, hs	---	1566	1472	1355	215
Dd H-NOX WT	5, hs	1602	1567	1471	1353	208
Lp H-NOX2 WT	5, hs	1600	1565	1469	1352	214
Np H-NOX WT	5, hs	1608	1566	1474	1357	209
So H-NOX WT	5, hs	1607	1567	1474	1357	213
So H-NOX P116A	5, hs	1610	1567	1474	1360	216
Tt H-NOX WT	5, hs	1599	1567	1469	1352	217
Tt H-NOX I5L	5, hs	1599	1564	1469	1352	217
Tt H-NOX P115A	5, hs	1602	1567	1469	1353	223
Tt H-NOX I5L/P115A	5, hs	1599	1564	1469	1352	220
Tt H-NOX P115A/Y140F	5, hs	1602	1567	1471	1354	220
Tt H-NOX W9F	5, hs	1600	1566	1470	1353	218
Tt H-NOX W9F/N74A	5, hs	1601	1566	1470	1353	218
Tt H-NOX Y140F	5, hs	1600	1565	1469	1353	220
Tt H-NOX Y140H	5, hs	1603	1561	1470	1353	218
Tt H-NOX Y140L	5, hs	1599	1564	1468	1351	220
Vc H-NOX WT	5, hs	1606	1561	1471	1354	224

[a] Abbreviations: *Cc*, *Caulobacter crescentus*; *Dd*, *Desulfovibrio desulfuricans*; *Lp*, *Legionella pneumophila*; *Np*, *Nostoc punctiforme*; *So*, *Shewanella oneidensis*; *Tt*, *Thermoanaerobacter tengcongensis*; *Vc*, *Vibrio cholerae*.

Table 2A Heme skeletal modes for various H-NOX domains and their mutants as the 5- or 6-coordinate, ferrous-NO complex.[a]

Protein	coord.	ν_{10}	ν_2	ν_3	ν_4	ν(Fe-NO)	ν(N-O)
β1 (1-194)	5, ls	1647	1586	1510	1376	526	1677
β1 (1-385)	5, ls	1646	1585	1509	1376	526	1676
β2 (1-217)	5, ls	1645	1585	1507	1373	528	1676
sGC	5, ls	1646	1584	1509	1375	525	1677
Cc H-NOX							
WT	5, ls	1641	1581	1508	1375	525	1689
Lp H-NOX1							
WT	5, ls	1633/1643	1584	1508	1373	525	---
Lp H-NOX2							
WT	6/5, ls	1630	1583	1497/1507	1373	551/525	1646/1677
Lp H-NOX2							
I5A	6/5, ls	1633/1641	1583	1508	1373	522	---
Lp H-NOX2							
P115A	6/5, ls	1633/1646	1584	1508	1373	522	---
Np H-NOX							
WT	6/5, ls	1633	1581	1500	1373	559/528	1655/1680
Tt H-NOX							
WT	6, ls	1625	1580	1496	1370	553	1655
Tt H-NOX							
P115A	6, ls	1636	1583	1497	1377	550	----
Vc H-NOX							
WT	5, ls	1640	1580	1504	1372	523	1674

[a] Abbreviations: *Cc*, *Caulobacter crescentus*; *Lp*, *Legionella pneumophila*; *Np*, *Nostoc punctiforme*; *Tt*, *Thermoanaerobacter tengcongensis*; *Vc*, *Vibrio cholerae.*